Formulation and rheological behavior of zinc slurries for zinc - air redox flow batteries

Diego Josué Milian Izeppi

THÈSE

Pour obtenir le grade de

DOCTEUR DE L'UNIVERSITE GRENOBLE ALPES

Spécialité : MEP : Mécanique des fluides Energétique, Procédés

Arrêté ministériel : 25 mai 2016

Présentée par

Diego Josué MILIÁN IZEPPI

Thèse dirigée par **Nadia EL KISSI, Directrice de recherche, Université Grenoble Alples**,

préparée au sein du **Laboratoire Rhéologie et Procédés**
dans **l'École Doctorale I-MEP2 – Ingénierie – Matériaux, Mécanique, Environnement, Energétique, Procédés, Production**

Formulation and rheological behaviour of anode zinc slurries for zinc – air redox flow batteries

Thèse soutenue publiquement le **22 octobre 2021**,
devant le jury composé de :

Madame, Cristina, IOJOIU
Directrice de recherche, CNRS, LEPMI, Université Grenoble Alpes, Présidente
Monsieur, Juraj, KOSEK
Professeur, University of Chemistry and Technology Prague, Rapporteur
Monsieur, Jean-Charles, MAJESTE
Professeur, Université Jean Monnet, Rapporteur
Monsieur, Philippe, MARCHAL
Ingénieur de recherche HDR, CNRS, LRGP, Université de Lorraine, Examinateur
Madame, Nadia, EL KISSI
Directrice de recherche, CNRS, LRP, Université Grenoble Alpes, Directrice de thèse

Invités

Monsieur Yahya RHARBI
Chargé de recherche HDR, CNRS, LRP, Université Grenoble Alpes
Monsieur Denis ROUX
Maître de conférences HDR, LRP, Université Grenoble Alpes

The cheapest and cleanest energy is the energy we do not use.

To our future generations

January 21, 2022

ACKNOWLEDGEMENTS

First of all, I want to thank the European Union Horizon 2020 research and innovation programme under the Marie Skłodowska-Curie Grant Agreement no. 765289. Without their support and funding, none of this would have been possible.

I would like to take this opportunity to express my gratitude to the Comité de Suivi Individuel (CSI). Since the the beginning of this PhD project these people guided and encourage me. *Cristina IOJOIU* from LEPMI, thank you for your enthusiasm and for your support whenever I needed your advice. I would like to thank warmly *Philippe MARCHAL* from LRGP, for contributing scientifically to my project and for sharing your life perspective through numerous anecdotes inside and outside a scientific background. Thank you also for having me as a guest in Nancy, I had a great time with the people I met from GEMICO and had the opportunity to learn more about suspensions from a different approach. I would also like to specially thank *Denis ROUX*, whose dynamism and advices helped me from the beginning of my project to make progress in my experiments. I enjoyed all the exchanges that we had outside LRP, whether in teaching activities, cycling in the mountains or trying to do cross country skiing.

I am also grateful to *François CATON* and *Yahya RHARBI*, your exciting ideas, contributions and your time helped me to achieve very important milestones in my research.

Many thanks to *Didier BLÉSÈS, Hélène GALLIARD, Frédéric HUGENELL, Mohamed KARROUCH, Vincent VERDOOT*. Your help on developing experimental set-ups, your advice and the time spent with me helped me to produce good quality results.

I want to thank also *François BERGEROT, Sylvie GAROFALO and Louise INFUSO*, from the first day you were always kind and helpful to whatever need I had.

I want to thank deeply *Nadia EL KISSI*, nor only for directing and supervising this work, but also for teaching me how to develop a scientific mindset and how to achieve excellence inside and outside academia. Thank you for the advices and for encourage me when I needed it. I truly appreciated working with you.

I am deeply thankful to all the people that contributed to the realisation of this project, specially the people from Laboratoire Rhéologie et Procédés (LRP) and the FlowCamp project. Throughout the length of my PhD I saw several people coming and going and be reassured that each of you left an important souvenir, piece of advice or joke to tell to future generations. I want to personally thank *Hugues le mec*, for showing me the way in the laboratory and in mountains. I never thought of me climbing outdoors and raising the thumb to reach the unreachable in our mountain expeditions. I learnt a lot from you through our conversations and activities, life is simpler when observed from above. It was a pleasure to have music around and non-stop chocolate cakes coming out from the oven, I never ate so much chocolate in my life as in this period. I want to thank *Moctar* for sharing his philosophy of life (and football) and for astonishing me with his improvisation and speaking skills, I will vote for you M Président.

Thank you *Martinien* for helping me at the very beginning of my PhD and it was interesting to see that even if we are from different continents, we have the same tropical blood and tropical food running through our veins. I thank *Ayoub*, the MacGyver of "la bureaucratie française", thank you for all your help and for having the time to stop by and have a random conversation in Italian while drinking coffee. Thank you, *Mehdi*, for being one of the MATLAB chevaliers, even if you were always turning the lab upside down, you always have the time to help us in our experiments or to share fun-facts that are still impressing us. Even if it was also for a short time that we share the lab, thank you Louis for your improvisation sketches and hopefully one day you will serve us the dreamed dinner à base des endives. I thank *Clément* and *Jenny* for their spontaneity, sincerity and for being the most welcoming hosts, you know how to take care of someone who just finished running 25 km and arrive in shorts on your balcony before the sunset. Thank you for making me discover Domène. Thank you *Héloïse* for those long discussions on how to align values and science around a cup of Yogi tea. I want to thank also the bakery of LRP, *Mathilde* for her lovely cakes and *Alice* for mastering cookies, and thanks to *Adja, Adriana, Antoine, Hanna, Ouattara, Mariem, Youness* for their support.

After some of the people that welcomed me went away to pursuit their dreams, there were other PhD students that came and marked my stay at LRP. I want to thank *Julie* for her support and for her authenticity, also for unveiling topics of discussion around which we can stay talking and talking for hours and hours, but not so late so you had the time to engage a FF XIV adventure. I want to thank *Emilie*, for her support at the end of my PhD, for sharing the love towards bread and for being available to do some coffee breaks when I needed to discuss more about bread. I want to thank the other sultan of MATLAB, *Sir Revaz*, full of ideas and good will, you will always help whoever is in need (with style). Thanks *Olivier*, the origami master, for showing me that formalities are not mandatory and sharing your love for cookies and cross-fit. I want to thank the new wave of PhD students that brought a fresh breeze of joy to the lab: *Ana, Beatrice, Clémentine, Khadija, Lydia, Mai, Maxime, Said, Sarah, Teko, Valentin* and *Xavier*. I want to thank also my three right hands that helped during my third year of PhD during their internship: *Mourad, Pauline* and *Toma* the backstreet boy.

I want to thank the people from the FlowCamp project, specially the Zinc-Air group: *Diego del Olmo, Misgina, Nak* and *Ricardo*. Thank you for all the scientific conversations that we had and the fact that we always faced the difficulties with a bit of humour. I want to thank *Gaël*, without you the Pantheon would not be the same, you are the best city guide, especially when it comes to discover a new city. *Jakub*, thanks to you I always have bubbling starter and homemade bread in my place, also for sharing your enthusiasm to fight climate change. Special thanks to *Caterina*, quack, thanks for sharing your joy and for showing me that chasing your dreams really pays off. Also, thanks for sharing adventures in places that we did not want to be *Concrete*. I want to thank also *Michael Küttinger*, for being the best host in Karlsruhe and discussing in depth all the 5-min video that we could find on arte. You are always welcome to come to Grenoble for more hiking.

I want to thank also la Bergerie, specially *Michael Schöbitz* for encouraging me to get out of bed at 6 AM to run for 1 hour continuously uphill. Thanks for sharing the love for mountains and pizza. Thanks to *Camille* and *Marie* for encouraging me at the end of my PhD.

Thank you *Adrien* for sharing many adventures in the mountains, and for the love of apèro and sapinette. Thanks to *Elena*, for our funny discussions about Italian culture (Pop X), for your amazing tiramisu and for the crazy parties. Thanks Vipin, for your friendship, for sharing the veggies and for your incredible Indian evenings at your place.

I want to thank la coloc *Toto*, thank you *Diana* and *Delphine* for sharing all your chocolate in every meal, thank you for the intensive course on French language and Grenoble lifestyle, and for sharing many adventures with me, like Family Kitchen. Thanks *Dario* for your intensive course on cheese, I loved it and for your great sense of humour.

I want to thank also my good friend from Guatemala, *José the tiger*, thank you for sharing your adventures and stories with me, and for making me feel homesick and proud of our motherland. I really enjoyed our conversations deciphering the world.

I want to thank the Saint Avre community, *La Patri, François* and *Johan and Mariana*, for your warmth welcome, for teaching me how to ski (work in progress), for all the hiking, wine tastings and for la Poire 90'. Thank you for you support and for cheering me up during the manuscript writing or when doing sports. Merci. I thank also my main sponsor, la Ferme Cartier.

I want to thank my family for their support, even from the distance. Thank you, *mamá*, for sharing your recipes and your advices, and for your unconditional love, I enjoy talking to you more often that a son is allowed to tell. Thank you, *Pamela lala Tommasa*, for sharing your good humour, for being my eyes in Guatemala and for taking care of Luca (and our mother as well). Thank you, *Alejandro* and *Sindi*, for your encouragements on my project and for always supporting me if I decide to go further. Thank you, *papá*, for your dad jokes and for always waving every bad situation with good humour. I love you all and thank you for your unconditional support, from my firsts steps to this very moment, you nourished and marked my life.

I want to dedicate this last paragraph to a person that continues to amaze me and makes me be a better version of myself. Thank you, *Candice*, for being my reason when I am lost and for showing me that the beauty of every little moment builds a great day. Because of you I certainly know that Earth is a good place, and more important, that France is the salle à manger of this good place. I am so happy that our paths crossed, 1 week in common in the lab in 2018, and I still see the same bright coming out from those eyes.

CONTENTS

LIST OF FIGURES

LIST OF TABLES

SUMMARY OF ACTIVITIES AND AUTHOR CONTRIBUTIONS

Scientific publications

Published

- *Use of Carbon Additives towards Rechargeable Zinc Slurry Air Flow Batteries.* Energies. 13 (2020) 4482. doi:10.3390/en13174482. N.H. Choi, D. del Olmo, *Diego Milián*, N. El Kissi, P. Fischer, K. Pinkwart, J. Tübke.

- *Pristine and Modified Porous Membranes for Zinc Slurry–Air Flow Battery.* Molecules. 26 (2021) 4062. doi.org/10.3390/molecules26134062. M.T. Tsehaye, G. Teklay Gebreslassie, N. Heon Choi, *Diego Milián*, V. Martin, P. Fischer, J. Tübke, N. El Kissi, M.L. Donten, F. Alloin, C. Iojoiu.

To be submitted

- *Gel polymer electrolytes rheological behaviour: yield stress and viscoelasticity. Diego Milián*, Denis C. Roux, F. Caton, N. El Kissi.

- *Polymer – Zinc interactions: rheological detection of polyacrylic acid polymer adsorption onto metallic microparticles. Diego Milián*, Y. Rharbi, N. El Kissi.

- Formulation and characterisation of zinc slurries for zinc slurry - air RFB: A rheological approach. *Diego Milián*, Nak Heon Choi, Misgina Tilahun Tsehaye, Peter Fischer, Cristina Iojoiu, Denis Roux, N. El Kissi.

Congresses proceedings

- Poster presentation at 54ème Congrès du Groupe Français de Rhéologie (GFR) Montpellier, France, 2019. *Formulation and rheological characterization of anode electrolyte slurry for zinc - air redox flow batteries. Diego Milián*, Nak Heon Choi, Diego del Olmo, Denis C. Roux, Nadia El Kissi.
- Oral presentation at ICR 2020 Rio de Janerio, Brasil. 18th International Congress on Rheology. *Zinc anode slurry formulation for zinc slurry – air redox flow battery: Polyacrylic acid stability and performance as gelling agent. Diego Milián*, Nak Heon Choi, Y. Rharbi, Denis C. Roux, Nadia El Kissi.
- Oral presentation at the 36th International Conference of the Polymer Processing Society (PPS-36) to take place September 26 - 29, 2021 in Montreal, Canada. *Formulation and electrochemical characterization of zinc slurries in zinc-air redox flow batteries. Diego Milián*, Nak Heon Choi, Diego del Olmo, Denis C. Roux and Nadia El Kissi.

Secondments

- Electrochemical characterization of zinc slurries in zinc-air redox flow battery. Fraunhofer ICT, Pfinztal, Germany.
- Rotational rheometry experiments in vibrating cell for zinc slurries. LRGP, GEMICO. UMR7274, Nancy, France.

Founding

This project has received funding from the European Union Horizon 2020 research and innovation programme under the Marie Skłodowska-Curie Grant Agreement no. 765289.

ABSTRACT

With current energy policies, aiming to drastically reduce greenhouse gases emissions, renewable sources will have a key role in supplying electricity to communities. However, in order to supply reliable, sustainable and resource-efficient electricity, stationary energy storage systems are needed to tackle the drawbacks of renewables intermittencies. Redox flow batteries (RFBs) are a promising technology because of its scalability and design flexibility. Among the different possible configurations, the focus of our study concerns a zinc slurry – air RFB. Specifically the objective is the development of an anode electrolyte slurry. The anode slurry consisted of zinc microparticles suspended in highly concentrated electrolyte (10 M KOH), conditions required to perform the redox reactions that will generate electricity.

In this study, we propose an analysis of the slurry anode electrolyte from a rheological approach, with the goal of optimising the formulation in regard of its electrochemical performance. In order to do so, the research work was divided as follows:

First, a gelled polymer electrolyte (GPE) is prepared consisting in an electrolyte, being aqueous potassium hydroxide (10 M KOH), and gelling agents. The purpose of the gelling agents is to provide a yield stress behaviour to GPE. In fact, when the battery is at rest, the material viscosity has to be high enough to maintain zinc particles suspended. Conversely, when the battery is under operation, the viscosity of the material has to decrease to ease the flow while pumping for its recirculation through the RFB cell. The challenge itself consisted in obtaining a viscoplastic behaviour in alkaline media, as the KOH electrolyte solution resulted in a pH of approximately 14. The choice of gelling agents, combining polyacrylic acid (PAA) and attapulgite clay, allowed to obtain a yield stress fluid in the alkaline medium considered. This result, established mainly by rheometry, indicates that we can consider the use of GPE like a potential network to host zinc particles, and to use the resulting suspension in the RFB.

We then approached the study of the zinc-polymer suspension. The objective was to highlight the possible interactions that can arise between zinc and polymer. We underline that such interactions can contribute to the transport of ionic species produced by electrochemical

oxidation-reduction reactions, in particular by zinc at the anode. Two approaches have been implemented to analyse these interactions.

First, an indirect approach is used based on rheometry measurements and effectively validates the hypothesis of such interactions. Then by a direct approach, based on the labelling of the polymer and its follow-up by spectroscopic means, zinc-polymer interactions were demonstrated. We emphasize here that, although indirect, rheometry remains a privileged approach due to its accessibility and its simplicity of use compared to spectroscopic approaches.

Lastly, the complete formulation of the zinc anode suspension is tested in a zinc-air RFB laboratory pilot. The objective here is to identify the key parameters of the formulation in order to optimize the electrochemical performance of the battery. Different formulations varying the polymer concentration were analysed, in agreement with the FlowCamp project partners. The main result of this chapter is the link between yield stress and electrochemical performance: below yield stress the resulting formulation is not appropriate because suspensions are subjected to sedimentation and above yield stress, the increase in viscosity affects the ionic conductivity and energy used during pumping. Moreover, here again, our study shows that the rheometry, although relatively simple, is a powerful tool, which can be used to optimize the formulation of the suspension for its use in the RFB.

In conclusion, our study made possible to propose an efficient formulation of zinc suspensions in a gelled polymer electrolyte. The stability of this suspension in an alkaline medium has been demonstrated and the role of the interactions between zinc-polymer has been identified and clarified. Each time, the rheometry has proved to be a powerful tool in highlighting and understanding the behaviours observed. It allows us to act on the formulation of the suspension and to optimize it, in connection with the electrochemical performances targeted. This is an important result for the future development of the innovative slurry-based redox flow batteries.

Current research on the subject is very active and multiple perspectives are contemplated. Concerning the immediate continuity of this work, after having identified the interactions zinc-polymer, after having characterized the rheometric behaviour of the GPE network, then the one of the suspension of zinc in the gelled polymer electrolyte, the next logical step was to determine its flow properties in the battery during pumping operations. A preliminary study of this flow behaviour is proposed. It is promising, in the sense that it makes it possible to visualize the velocity fields and to identify their characteristics. In the long term, it should make it possible to provide an experimental database with a view to testing the numerous results of numerical simulations of flows in the battery proposed in the literature, and within the FlowCamp consortium.

RÉSUMÉ

Avec les politiques et enjeux énergétiques de nos jours qui visent à réduire drastiquement les gaz à effet de serre, les énergies renouvelables ont un rôle majeur dans l'approvisionnement en électricité. Cependant, afin de fournir une électricité de façon fiable, durable et économe, des systèmes de stockage d'énergie stationnaires sont nécessaires afin d'assurer une production continue de l'énergie et prendre le relais lors des intermittences. Les batteries à flux redox (RFB) sont une technologie prometteuse en raison de leur modularité d'échelle et de leur flexibilité de conception. Parmi les différentes configurations possibles, l'objectif de notre étude concerne les batteries à flux redox à électrolyte liquide avec des particules de zinc. Plus précisément, le but est le développement et la formulation de l'électrolyte à l'anode. Nous avons choisi de mettre en œuvre des microparticules de zinc en suspension dans une solution d'hydroxyde de potassium fortement concentrée (10 M KOH). Une telle formulation, optimisée, devra permettre les réactions redox qui généreront de l'électricité.

Dans cette étude, nous proposons une analyse de l'électrolyte par une approche rhéologique, visant à en optimiser la formulation, en lien avec les performances électrochimiques. Pour cela, ce travail de recherches à été divisé comme suit :

Tout d'abord, un électrolyte polymère gélifié (GPE) est préparé à partir d'une solution d'hydroxyde de potassium (10 M KOH) et d'agents gélifiants. Le rôle des gélifiants est d'apporter au matériau un comportement de fluide à seuil. En effet, au repos la viscosité du fluide doit être suffisamment élevée pour maintenir les particules de zinc en suspension. A l'inverse, lors du fonctionnement de la batterie, la viscosité doit diminuer pour faciliter l'écoulement du fluide lors des opérations de pompage et l'alimentation de la batterie à flux redox. Le défi qui se posait était d'obtenir ce comportement viscoplastique en milieu alcalin, la solution de KOH étant caractérisée par un pH de l'ordre de 14. Le choix des gélifiants, associant acide polyacrylique (PAA) et argile (attapulgite), a permis d'obtenir un fluide à seuil dans le milieu alcalin considéré. Ce résultat, établi notamment par rhéométrie, permet donc d'envisager l'utilisation de ce GPE comme matrice potentielle pour accueillir les particules de

zinc, et utiliser la suspension obtenue à l'anode dans la RFB.

Nous avons alors abordé l'étude de cette suspension zinc-PAA. L'objectif était de mettre en évidence les interactions susceptibles de se développer entre zinc et polymère. Soulignons que de telles interactions contribueraient au transport des espèces ioniques produites par les réactions électrochimiques d'oxydoréduction, notamment par le zinc à l'anode. Deux approches ont été mises en œuvre pour analyser ces interactions.

D'abord une approche indirecte basée sur des mesures de rhéométrie et qui permet effectivement de valider l'hypothèse de telles interactions. Puis par une approche directe, basée sur le marquage du polymère et son suivi par des mesures de spectroscopie, qui démontrent ces interactions zinc-polymère. Soulignons ici que, bien qu'indirecte, la rhéométrie reste une approche privilégiée du fait de son accessibilité et de sa simplicité d'utilisation par rapport aux approches spectroscopiques.

Dans une dernière partie, la formulation complète de la suspension de zinc est testée dans un pilote de laboratoire représentatif du fonctionnement de la batterie zinc-air à anode liquide. L'objectif ici est d'identifier les paramètres clés de la formulation en vue d'optimiser les performances électrochimiques de la batterie. Différentes formulations faisant varier la concentration de polymère ont été analysées, en accord avec les partenaires européens. Le résultat principal de ce chapitre est le lien entre la contrainte seuil d'écoulement et performance électrochimique : en dessous du seuil la formulation résultante n'est pas adéquate car les suspensions sont sujets à la sédimentation et au-dessus du seuil, l'augmentation de la viscosité affecte la conductivité ionique et l'énergie utilisée lors du pompage.

Par ailleurs, là encore, notre étude montre que la rhéométrie, bien que relativement simple, est un outil performant, qui peut être utiliser pour optimiser la formulation de la suspension en vue de son utilisation dans la RFB.

En conclusion, notre étude a permis de proposer une formulation efficace de suspensions de zinc dans un électrolyte polymère gélifié. La stabilité de cette suspension en milieu alcalin a été démontrée et le rôle des interactions entre zinc/poymère a été identifié et éclairé. A chaque fois, la rhéométrie s'est révélée être un outil performant dans la mise en évidence et la compréhension des comportements observés. Elle nous permet au final d'agir sur la formulation de la suspension et de l'optimiser, en lien avec les performances électrochimiques visées. C'est un résultat important pour le développement futur de batteries redox à électrolyte liquide innovantes et performantes.

La recherche actuelle sur le sujet est très active et les perspectives multiples. Pour ce qui concerne la suite immédiate de ce travail, après avoir identifié les interactions zinc/polymère, après avoir caractérisé le comportement rhéométrique de la matrice GPE puis de la suspension

de zinc dans l'électrolyte polymère gélifié, la suite logique était d'en déterminer les propriétés d'écoulement dans la batterie lors des opérations de pompage. Une étude préliminaire de cet écoulement est proposée. Elle est prometteuse, en ce sens qu'elle permet de visualiser les champs de vitesse et d'en identifier les caractéristiques. Elle devrait permettre à terme de fournir une base de données expérimentales en vue de tester les nombreux résultats de simulations numériques des écoulements dans la batterie proposées dans la littérature, et au sein du consortium FlowCamp.

GENERAL INTRODUCTION

Climate change has become a generalized crisis, with negative environmental, social and economic impacts as more frequent disasters like droughts and floods cause the displacement of communities around the world. Because of this, stronger climate policies are being put in place with the goal of reducing carbon emissions globally. However, fossil fuels still have a big share in the electricity market, accompanied with the production of greenhouse emissions. Therefore, to booster the decarbonization of the energy sector, the integration of renewable sources is a must. Energy sources like wind and solar require stationary energy storage systems (ESS) to compensate the intermittencies associated to their power supply.

With the goal of developing efficient and large-scale ESS, the European Union founded a multinational network based in a Marie Skłodowska-Curie action named "FlowCamp", standing for Redox Flow Battery Campus (`www.flowcamp-project.eu`). The research within this network concerns the development of redox flow batteries (RFBs). The working principle of a RFB consists in a cell where electrochemical energy is converted to electricity during discharge and inversely during charge. The cell is divided in two half cells, corresponding to the anode and the cathode compartments, separated by an ion-selective membrane or separator preventing the mixing of electrolyte solutions. The electrolyte solutions are stored externally in tanks and continuously pumped in a circuit through each half cell. Electroactive species carried by the electrolyte will then react on the electrode surface for the discharge/charge of the battery. In this design, the amount of energy stored is defined by the amount of the electrolyte, whereas the power output is determined by the size of electrode. The decoupled energy storage and power output is a main advantage of this battery, allowing a flexible design towards direct energy requirements.

However, current commercial RFB solutions have different limitations like the price of the electro active species, a low power output and lifespan of the system. For instance, all-Vanadium RFB is the most mature RFB but the high cost of vanadium, dictated by mining industry, results in an expensive price for stored energy. Combined with the necessity of increase the power output with RFB, new technologies are being investigated.

To overcome the limitations of current RFB technologies, FlowCamp project work on high-performance, low-cost, next-generation RFBs. At the forefront of the research, 15 PhD students work on three types of RFBs: hydrogen-bromine, all-organic and a zinc slurry - air system, the former making the core of this research. Zinc-air has an advantageous theoretical specific energy of 1300 Wh/kg [Jörissen, 2006], which is around 5 times higher than the one of lithium-ion batteries (200-250 Wh/kg), being the benchmark ESS technology. In zinc-air RFB, metallic zinc is the anode and oxygen is the cathode. Combined with zinc availability, economic viability and safety of the system, this technology has high potential to become the next generation RFB reference. Nevertheless, several drawbacks coming from the metallic anode hinder the performance of the battery. One of the main problems is the zinc dissolution-deposition mechanism. Zinc in solution can be deposited as dendrites that can grow indefinitely until piercing the membrane of the cell, leading to premature battery failure.

Luckily, if the design of the zinc-air battery is the one of an RFB, these problems are significantly reduced as electrolyte solution is continuously renewed in the cell. In addition in 2011, a new approach was given to RFBs consisting in suspending a solid particle electrode in electrolyte media [Duduta et al., 2011]. This configuration is known as semi solid fluid cell (SSFC), in which material utilization is higher in comparison to a pure aqueous RFB, increasing its practical energy density. The SSFC is chosen for the development of a zinc slurry – air RFB in the FlowCamp project.

The zinc slurry - air group is composed of 5 PhD students focused on a specific topic matured in mutual collaboration with academic and industrial partners. The research topics consists in different battery components including an anode electrolyte slurry, an ion exchange membrane, an air bifunctional cathode, cell prototype design and testing accompanied by modelling and simulation.

The work at Laboratoire Rhéologie et Procédés (LRP) consisted in the formulation of a zinc anode slurry and designing protocols and rheometric tools to characterise slurry and its flow behaviour, according to the operational conditions in the battery, by rotational rheometry. Moreover, the formulated slurry was tested in the prototype cell, and determination of rheological key properties influencing the performance of a zinc slurry - air RFB were highlighted. The work performed in LRP will contribute to the enrich the data base that will be crucial to develop applicable models coupling slurry flow behaviour and electrochemical properties,

predicting the electrochemical performance of the battery during the discharge and charge of the zinc slurry.

In the study presented in this manuscript, attention is given to the formulation and rheological behaviour of the materials used to prepare zinc anode slurries. A specific focus is given to the trade off between network conductive properties and the viscosity of the slurry. Specifically, sufficient conductive material is needed to build a percolated network, but its viscosity needs to be appropriately low so the slurry can be pumped through the cell. The formulation is composed of a concentrated potassium hydroxide (KOH) electrolyte, gelling agents, zinc oxide (ZnO) and anode zinc micro particles. The compatibility of the components in the formulation is studied with a rheometric approach in regard of the electrochemical performance of these materials in a prototype cell. Along these lines, this manuscript is divided in the following strategy.

In the first chapter, the scientific and economic motivation is presented before discussing the advantages and disadvantages of the most relevant ESS to grid support, among them RFB.

In a second chapter, the rheology of suspensions is presented together with rheometric tools that will be useful to characterise the suspensions studied in this work. This chapter will conclude on the synergistic approach in which rheometry can be used to enhance RFBs performance. Recent studies are discussed encompassing both rheology of suspensions and RFBs.

The subsequent chapters contain the main achievements obtained during the PhD, where results are discussed highlighting the impact of the rheological approach to the RFB field.

In the third chapter, the suspending fluids used to prepare zinc slurry suspensions are presented. Gelled polymer electrolytes (GPEs) are prepared from aqueous 10 M KOH and gelling agents. The harsh alkaline environment in which pH $\gtrsim$ 14 is challenging because the choice of gelling agents chemically stable in these conditions is narrow. The study of gelling agent concentration on the rheological behaviour of GPEs is determined by using a custom-design geometry, ensuring homogeneous sample shearing during characterisation. It is highlighted in this chapter that with the formulation proposed in our study, a gel behaviour is obtained, even in such harsh alkaline environment, with the ability to suspend zinc microparticles with high potential for a RFB.

In the fourth chapter, the attention is focused to the system zinc microparticles and PAA polymer. The main objective of this study is to determine if there are interactions that can help building a percolated interconnected network between zinc and PAA polymer, enhancing the conduction of zinc ionic species. Interaction are studied by using rheometry and spectroscopy. The indirect detection of interactions is first obtained from PAA rheological behaviour after

adding zinc to PAA. Secondly, labelling of PAA allowed to detect and validate interactions by following the concentration of labelled-polymer by UV-Vis spectroscopy. Hence, rheometry is presented as an accessible and powerful tool to determine microscopic interactions from a macroscopic point of view, based on the rheological behaviour of PAA gels.

In the fifth chapter, the preparation of zinc slurries using GPEs and zinc microparticles is presented. The electrochemical performance of slurries was tested in a custom-made RFB developed by Fraunhofer ICT, within the FlowCamp network. Slurries electrochemical behaviour is studied and it was found that an optimal PAA concentration yielded a maximum performance. Rheometry measurements allowed to link a maximum performance with slurries viscoplastic flow behaviour. Our study found that rheometry can predict the optimal formulation that will yield the best performances based on flow behaviour and particle size.

Finally, the work presented in this manuscript is summarized in a final conclusion indicating the main findings, the contributions to the RFB community and the future work to be done to improve the studied technology. Furthermore, an ongoing work is introduced as a perspective in which an experimental set up is developed to study the behaviour of a zinc slurry during pumping in a RFB. The experimental device consists in a visualization cell in which a model fluid, with the characteristics of a zinc slurry, is pumped through.

CHAPTER

ONE

ENERGY STORAGE SYSTEMS

This chapter aims to make the reader aware of existing energy storage technologies boosting renewable energy sources like solar, wind and hydropower. Moreover, market analysis and the problematic limiting their application to a global scale is briefly discussed. Later on, innovation in this energy field is reviewed, including the acclaimed lithium-ion battery and different interesting alternatives, among them the redox flow battery (RFB). Special attention is given to the latter, with much focus in the promising zinc-air RFB. Several technologies are described in such way that the reader will be able to question if current storage systems deployed on field are the best solution for the ever-growing energy demand.

"This endless circulation of the electric fluid (this perpetual motion) may appear paradoxical and even inexplicable, but it is no less true and real; and you feel it, as I may say, with your hands" - Alessandro Volta [Fabbrizzi, 2019]

Contents

1.1 Introduction

Since the beginning of times, human being has been struggling with the mastering of different energy sources, from primary needs like maintaining a warm environment during cold winters, to more complicated applications like powering portable devices and feeding communities with electric energy. With increasing populations around the world and increasing economies, energy demand has been increasing proportionally to GDP globally [Liddle et al., 2020], and demand has been alleviated depending on geographical resources and available technologies to what it has become our current society.

In a world where infrastructure has been settled as the one of a carbon and fossil-fuel dependent society [Huggins, 2015], it is not a surprise finding our environment ravaged by deforestation, mining activity and oil drilling. The enormous emission of greenhouse gasses together with reduced capacity of exhausted forestlands to absorb premature released CO_2 in the atmosphere [Tilman et al., 2001], has alarmingly increased eutrophication and average seasonal temperatures all around the world. As a result, the number of communities facing critical problems related to climate change is increasing, not to mention the dramatic decrease of wildlife.

To reduce harmful effects mentioned above, multilateral cooperation to foster infrastructure decarbonization has been deployed between political, scientific and economic groups [Bazilian et al., 2020; Loftus et al., 2015]. With increasing limitations on carbon emissions, one thinks directly on renewable sources like wind and solar energy to find a viable path to decarbonize electricity [Kittner et al., 2017]. In order to increase renewable energy capacity, an important factor to optimize is electrical energy storage. Such systems should offer operational flexibility

and a fast response while tackling the problem of renewables intermittency. If society intends to shift to a sustainable energy production, one cannot ignore the role of energy storage to boost and fully integrate renewables, technologically and economically [Sisternes et al., 2016].

This chapter reviews different technologies that aim to harvest energy from different sources. Opportunities and limitations of deployed energy systems will be reviewed and compared with more recent technologies, like RFBs. A large focus will be given to zinc-air RFB, a configuration with a lot of potential due to its high energy density when compared to other existing batteries [Davari et al., 2018]. Zinc anode development is thoroughly investigated in this manuscript, more precisely we propose an innovative approach that aims to tackle the problematic around its performance.

1.2 Motivation

Recently the incorporation of renewable sources, namely solar, wind and water-based energies has increased in Europe reaching a 34 % of gross electricity consumption among the 27 European Union state members (EU - 27) [Eurostat, 2020]. However, fossil fuels still posses the biggest share in the electricity generation in the region.

Nevertheless, scientist, environmental groups and politicians are working together with the aim of reducing emissions coming from human activity. In 2019, the European Commission made a communication in which they explained the ambitious European Green Deal [European Commission, 2019]. This action aims to make Europe the first climate-neutral continent by 2050 and at the same time ensuring 3 key principles for the clean energy transition:

1. Affordable energy supply.

2. Fully integrated, interconnected and digitalized EU market.

3. Prioritize energy efficiency and developing a power sector based on **renewable sources**.

Nonetheless, incorporation of renewable sources to the electricity grid is not straightforward; solar energy depends on season irradiation and daylight, whereas wind depends on seasons. For instance, it is possible to observe how these resources change over time compared to the energy demand, as presented in figure 1.1.

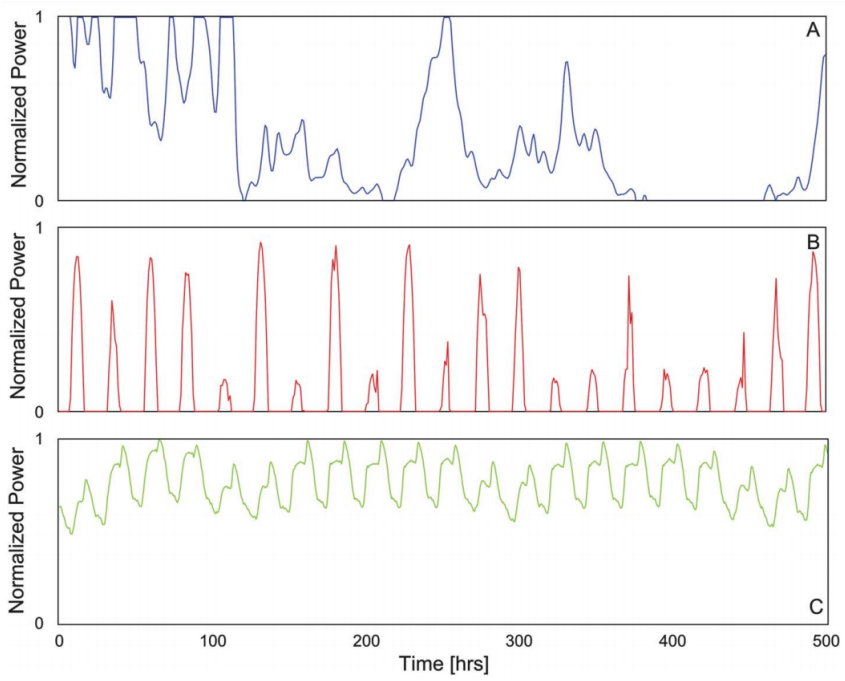

Figure 1.1: Real shape of power and demand over time. A) Normalized shape of wind power in Wilhelminadorp, Netherlands obtained for a GE 1.5 MW turbine. B) Normalized shape of solar PV power output in January in Boston. C) Normalized shape of electricity demand in the UK. [Rugolo et al., 2012].

Because daylight used to feed photovoltaic (PV) power stations varies with daytime and seasonality [Pfeifroth et al., 2018], it is normal to find fluctuations in the energy output generated by PV stations. Similar conclusion is obtained for wind patter as observed in figure 1.1, even for Netherlands, considered a windy country. More importantly, the shape of the demand C, does not correspond to the generated power produced either by wind A or solar B renewable energy sources. In other words, the installed capacity using renewables will not be always similar to the power output as these sources fluctuate over time. With the social and industrial rhythm at which energy is consumed, the energy produced just with renewable sources would not satisfy current demand. When the energy demand is not met, the most common consequence is a power crisis in which some sectors in a specific area are left without electricity, as for example the most recent case being the 2021 Texas power crisis. During the winter of 2021, Texas was hit by several winter storms and as a consequence the region fell to record low temperatures that led to the failure of power supply installations. As a result, millions of homes and business were left without power for several days.

However, renewable sources penetration into the grid can be possible if current capacity is redesigned in a more flexible way. A solution that has already been put in place in many sectors are energy storage systems (ESS), and among them we find redox flow batteries (RFBs).

Common use of ESS is displayed in figure 1.2.

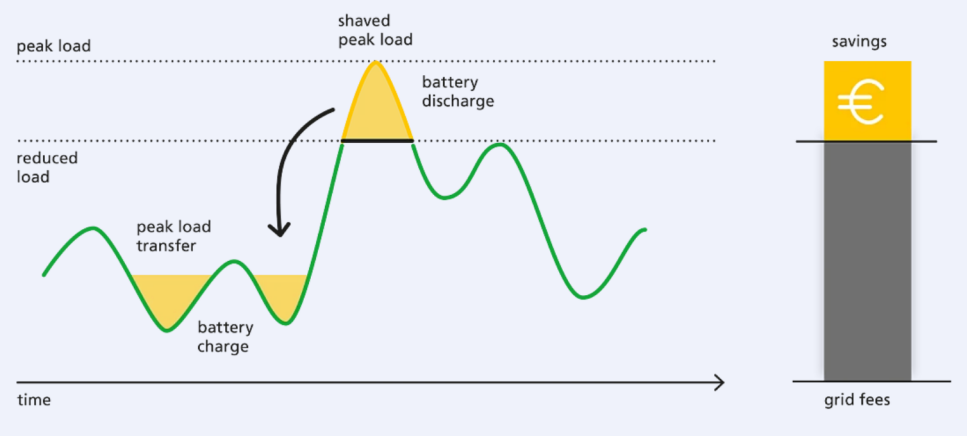

Figure 1.2: Peak shaving using a battery as ESS. Consumption peaks are reduced by using the energy stored in the battery to stabilise load [*EDF Renewables in Germany — Performances & Services* n.d.]. https://www.edf-re.de/en/battery-storage/performances-services visitied on August 4th 2021.

Energy coming form a given source i.e. solar energy, is stored in a ESS during low demand periods. as observed in the reduced load region in figure 1.2. In this period ESS can store significant significant amounts of energy in the order of magnitude of kilowatt-hour (kWh)to gigawatt-hour(GWh), depending on the energy source and ESS. This unit of energy represents the amount of power in watts that can be sustained for one hour. When power grid is under high demand, stored energy can be transferred to the grid during peak hours, reducing the total load in the whole installation. This process is known as peak shaving. In this way, power shortages, in which the electricity demand cannot be reached, due to lack of energy and poor management can be prevented. Furthermore, the price of electricity remain stable over time, making it accessible to larger communities [Kittner et al., 2017].

ESS are essential to have a better energy management and integrate renewable energy sources, accompanied with the goal to decrease the reliability on fossil fuels, which to date still make more than 40 % of the EU production of electricity [Eurostat, 2020]. In the following section, several ESS are reviewed focusing on mechanical and electrochemical ESS. The ESS that are presented are chosen because of their technology readiness level, with some of the technologies deployed worldwide, among them the core of our research which is **redox flow batteries (RFB)**.

1.3 Energy storage systems ESS

ESS are able to store energy coming from a given source, renewable and/or not renewable, by converting electrical energy to another type of potential energy, amongst them mechanical, electrochemical or thermal potential energy. When electricity power is needed, ESS are able to convert back the potential energy in electricity to be restored in the power grid, as in figure 1.2.

The main goal of ESS is to deliver uninterrupted and good quality electricity to users in different scenarios. The most common scenario is to balance the energy demand, as in peak shaving. However, there has been an increase of deployment in ESS used to build small electrical grids, denominated microgrids. In this case, the interest is to deliver electricity to remote areas that are isolated geographically from bigger grid installations [Pinnangudi et al., 2017], like those making part of national grids that are managed by the government of big companies.

In figure 1.3, ESS are classified according to their power capacity and discharge time.

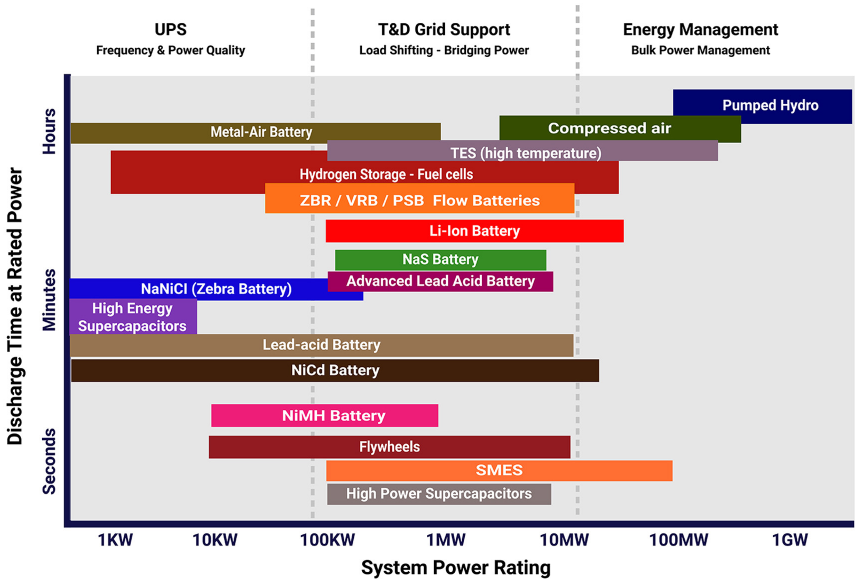

Figure 1.3: Available and developing energy storage technologies by power capacity and discharge time [Argyrou et al., 2018].

The most mature and promising ESS are classified in figure 1.3 according to their power rating, meaning the power in watts (W) that they are able to deliver in a discharge period of time. ESS can serve different purposes depending on the power that they can provide. Low power rating system, usually under 100 KW, are used for frequency and power regulation. When power demand fluctuates, ESS need to be activated (or deactivated) in order to supply an ideal voltage and frequency. A fast response is needed in this case to deliver quality power

uninterruptedly to end users. When the power that can be supplied is in the order of MW and higher, ESS are used for grid support and energy management. In this applications ESS can store the energy that it is produced in excess and that will be lost otherwise. This stored energy can be used later to equilibrate the output power according to the demand, as for example peak shaving in figure 1.2.

Interest on ESS is continuously to integrate renewable energy sources and to be able to deliver power accordingly to the demand. The trend is that more ESS are going to be deployed worldwide to manage energy more efficiently. In the next section, an overview of several ESS is provided for deployed and emerging technologies, analysing its principal advantages and challenges.

1.4 ESS technologies overview

In this section, an overview of several ESS is available to have an idea of which are the main characters of energy storage. Among the available technologies we describe technologies that are in the range of 100 kW and higher, for grid support and energy management. Moreover, the overview is focused on the ESS that can deliver power in range of minutes to hours, as this is the range of application is the area in which the technology under study, RFBs, are focused, as observed in figure 1.3

Among the technologies available, the ones having the highest market share are described, being pumped hydro, compressed air energy storage (CAES) and batteries.

1.4.1 Pumped hydro

The use of water bodies to generate energy has been known from ancient times and it has been recently designed in early 20th century to work as an energy reservoir. The working principle of pumped hydro storage is to store massive amounts of water in an upper reservoir with a significant height difference level, accumulating potential energy ($E = mgh$). When power is required, water from upper reservoir is released and forced to flow through turbines for electricity generation. Contrarily, when power is not needed, water can be pumped to the upper reservoir for future use.

When analyzing figure 1.3, it is observed that pumped hydro storage has the highest power capacity reaching the order of GW. Nowadays, there is an approximately installed capacity of 169 GW distributed globally, with the largest plant having 3 GW that can be discharged for a duration of 10 h at rated power. Other advantages are the long lifetime of installations (30-60

years), acceptable high efficiency (65-85 %) and fast response time (< 1 min) [Argyrou et al., 2018].

However, even if installed capacity has increased in Europe, USA and Japan, the cost of installation remains very high due to material, the need of large land area and extended building period [Deane et al., 2010]. Moreover, this technology remains geographically limited to water bodies and rivers [Blakers et al., 2021], that not all countries have access to. Other drawbacks are the environmental from modifying aquatic environment and social impact, as in some cases communities are displaced from building sites [Boyé et al., 2016].

1.4.2 Compressed air energy storage CAES

With this technology, electricity is used to compress air during off-peak demand. Air is compressed in natural or artificial caverns into a sealed volume at high pressures. When electricity is needed, air is expanded using heat exchangers, producing work. Finally, electricity is generated through turbines. Power capacity ranges from 10 kW to more than 100 MW [Kapila et al., 2019], penetrating different energy grid markets like grid support and bulk power. Another advantage is that power can be supplied for extended periods of time, in the range of tens of hours [Pinnangudi et al., 2017].

Nevertheless, as pumped hydro, this technology requires an specific geography that cannot be found everywhere. In the review made by Olabi et al. [Olabi et al., 2020], several authors raised fire hazard as a serious threat, as air is stored in geological caverns where the presence of hydrocarbons is unavoidable leading to an explosion risk. In addition, CAES has lower efficiency compared to pumped hydro (50-80 %) due to all energy required to pressurize and expand.

Pumped hydro and CAES are the most developed mechanical technologies that can supply energy for grid support and management. In the next section several electrochemical devices, batteries, are described.

1.4.3 Electrochemical energy storage systems

Moving to the core of the research, several batteries offer electrochemical storage based on different material chemistries and designs. The power capacity ranges from 100 W to tens of MW. In this category, an overview of different secondary batteries is presented. Secondary batteries are electrochemical systems that are rechargeable, based on reversible electrochemical reactions and material stability.

Batteries are composed of two electrodes, with different chemical potentials inherent of the material chemistry. In a given set-up, the electrode with the lowest potential is called anode, and the one with the highest potential is called cathode. Both electrodes are connected by a ion conductive material called electrolyte. When power is needed, electrons flow from the anode to cathode in an external circuit, whereas ions are transported between electrodes through the electrolyte to maintain the charge balance, converting electrochemical potential energy into electricity. In this discharge process, the anode is oxidized and the cathode is reduced. During charging, the process occurs in the opposite direction by supplying a higher voltage to the battery [Armand et al., 2008; Soloveichik, 2011].

The amount of energy that a battery can store can be maximized by [Armand et al., 2008]:

- Selecting two redox couples in which the chemical potential between the two electrodes is large
- Increasing energy density (lower mass or volume of reactants per exchanged electron)
- Reducing consumption of electrolyte in electrochemical reactions

Depending on the chemistries used as anode and cathode, different advantages and challenges are faced during operation. A redox couple is an oxidizing and reducing agent, after being reduced or oxidized, respectively. In this way, materials can be chosen according to its oxidizing/reducing strength, that will decide if the reactions will occur spontaneously or not. Different technologies are presented in this section ranging from different maturity, market penetration and some promising technologies.

1.4.3.1 Lead - acid battery

Lead (Pb) - acid battery is the most mature rechargeable battery. The first rechargeable battery was conceived in 1859 by Gaston Planté [Kurzweil, 2010]. The cell reaction is the following:

$$PbO_2 + Pb + 2H_2SO_4 \underset{\text{charge}}{\overset{\text{discharge}}{\rightleftharpoons}} 2PbSO_4 + 2H_2O \quad E^0 = 2.04\ V \tag{1.1}$$

In which lead (Pb) is the anode, PBO_2 is the cathode and the electrolyte is sulphuric acid (H_2SO_4).

Lead-acid batteries are a cost effective alternative to deliver power with high efficiency (65-80 %). Initially the battery was just suitable for power quality application and frequency

regulation (lower range of system power rating in figure 1.3), but recent advances have made possible the use for grid support with a power output of 10 MW [Argyrou et al., 2018].

Contrarily, several drawbacks limits battery ability to bigger storage markets. Battery capacity decreases with time, limited to approximately 1500 cycles (cycle is defined as the process of complete charging and discharging) [Pinnangudi et al., 2017]. Additionally, this technology is dependent to lead, which poses a safety risk because of its toxicity. However, methods to recycle lead have proven to be efficient to be re-used. Even if this technology is very mature and has been deployed globally, its primary application remains power applications, whereas grid support and energy management remains limited because of its low energy density (30-50 Wh/kg) [Beaudin et al., 2015], limiting its application to small-medium scale storage applications.

1.4.3.2 Li-ion battery

Li-ion has powered the revolution of portable electronics since it was first commercialized in 1990s by Sony. The research on the development of cathode intercalation materials in the 1980s led by John Goodenough group, who won the 2019 Noble Prize in Chemistry together with his collaborators Stanley Whittingham and Akira Yoshino [Manthiram, 2020], made possible the development of this rechargeable battery.

A scheme of a Li-ion battery is displayed in figure 1.4.

The working principle of the battery is the intercalation chemistry of Li^+ ions. As observed in figure 1.4, the negative electrode is a graphitic carbon able to hold Li^+ ions within its layers. On the other side of the battery, the cathode is a Li-intercalation compound. Both anode and cathode are able to insert and remove Li ions reversibly from their structures allowing its rechargeability [Dunn et al., 2011].

High energy density (200-250 Whkg^{-1}) and voltage (3.8 V) [Rahman et al., 2013; Soloveichik, 2011] inherent of this electrochemistry, make this battery the ideal choice for portable devices and with the growing hybrid electric vehicles.

However, concerns regarding the availability of transition metals (like cobalt, nickel and manganese), which are extracted from natural resources [Armand et al., 2008] can hinder its current production levels in the future. In addition, safety concerns regarding fire hazards due to thermal runaway leading to fires and explosions during operation [Kong et al., 2018], and lithium availability combined with challenging recyclability limits the prosperity of the technology in the long term [Vikström et al., 2013]. Nevertheless, several electrical energy storage (EES) installations had been deployed in the US, with a power rating in the order of

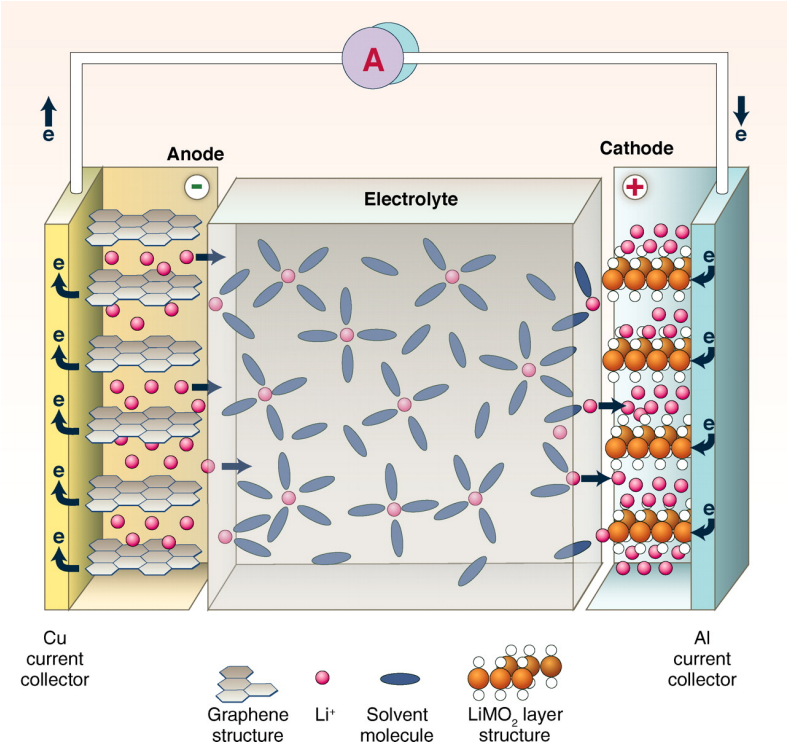

Figure 1.4: Schematic of a Li-ion battery. [Dunn et al., 2011].

MW, for applications in grid regulation and smart grids [Soloveichik, 2011].

Up to here the discussion in batteries concerned the most mature technology, being lead-acid battery, and the most commercialized one, the lithium - ion battery. However, it was seen that these batteries are not enough to satisfy the energy storage market, either because of the poor performance inherent of the battery chemistry, or because of the concerns of dealing with toxic materials. Because of this, the next type of battery is separated in a different section, as this type of battery can overcome some of the limitations presented before.

1.5 Metal - air batteries

Metal-air batteries consists mainly in a metallic anode in the form of a foil or a plate, an air cathode presented as an open cell structure that takes air from the atmosphere or from other synthetic source. Ion exchanges occurs in an electrolyte medium through an ion-exchange membrane separating the anode from the cathode.

The attractiveness of this technology lays on the high energy density inherent of metal anodes and oxygen combined to the fact that positive oxygen electrode adds no weight to the battery (before discharge). Theoretical energy density of some metal - air batteries can be a few time greater than Li-ion batteries (Figure 1.5).

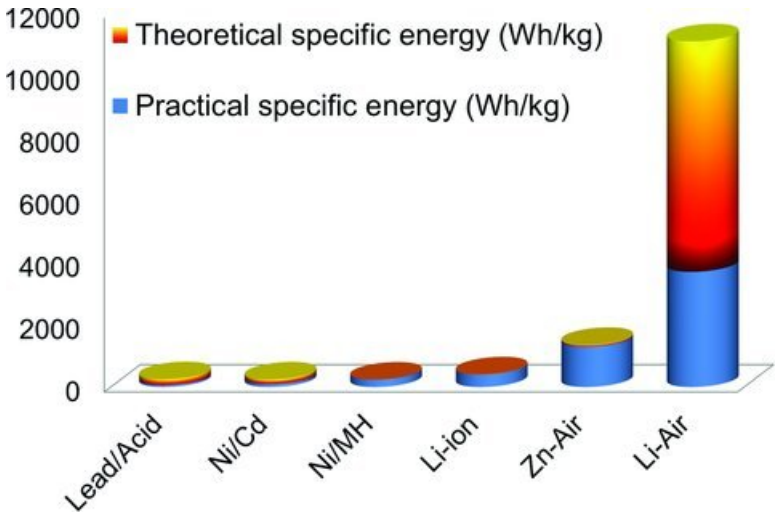

Figure 1.5: Theoretical and practical energy density for various rechargeable batteries [Lee et al., 2011b].

The real energy density of metal - air batteries is still far from its theoretical value (figure 1.5). If metal-air batteries are developed with care for commercial use, these batteries can be the next solution for ESS and electric vehicles (EVs) [Rahman et al., 2013; Sonneveld, 1991].

The electrical rechargeability of the metal-air batteries it is regarded as a big challenge. Problems involved with the anode stability during consecutive discharge/charge cycles reduce its capacity over time. Moreover, one of the milestones for metal-air batteries is the development of a bi-functional air electrode, capable of catalyse reactions involved in the charge (oxygen evolution reaction OER) and discharge (oxygen reduction reaction ORR) [Davari et al., 2018; Jörissen, 2006; Nikolova et al., 2008; Sasikala et al., 2014], and the use of non-precious metals as catalyst to reduce battery costs.

Alternatives like hydraulically [Smedley et al., 2009] and mechanically [Caramia et al., 2014; Mahlendorf et al., 2021] rechargeable batteries have been investigated , where the anode material is renovated or regenerated externally to the battery. However, research efforts focus on making metal-air batteries electrically rechargeable for an easier grid integration.

Some of the metal anodes are reviewed in table 1.1, where performance values can be observed.

Metal anode	Electrochemical equivalent of metal $[Ah/kg]$	Theoretical cell voltage with O electrode $[V]$	Theoretical specific energy of metal oxygen couple $[Wh/kg]$	Practical operating voltage metal - oxygen $[V]$
Li	3861	3.3	12741	2.4
Ca	1337	3.4	4547	2.0
Mg	2205	3.1	6837	1.4
Al	2980	2.7	8046	1.6
Zn	820	1.6	1312	1.1
Fe	960	1.3	1248	1.0
Cd	478	1.2	572	0.9

Table 1.1: Characteristic data of some metal-oxygen cells adapted from [Jörissen, 2006].

Nonetheless, the theoretical values of these metals are still far from the real performance obtained in laboratory prototypes and deployed systems. Most of the metals corrode spontaneously in aqueous electrolyte and other metals are not chemically stable in electrolyte media. As exposed by Mainar et al., more research on anode development is important to obtain a battery with a longer lifespan. Some of the main problems related to anode limitations and negative effects are pictured for the zinc metallic anode, being the focus of this study. The three main problems related to anode failure are the followings [Mainar et al., 2018a]:

Zinc anode limitation	Negative effect
Zinc passivation	1. Reduced capacity 2. Electrolyte depletion 3. Porosity reduction 4. Conductivity loss
Zinc corrosion (HER)	1. Reduction of charge retention and utilization efficiency 2. Negative effect on zinc, electrolyte and sealing structure
Zinc dissolution – shape changes and dendrite growth-	1. Reduced zinc anode stability 2. Battery failure 3. Capacity reduction

(a) Zinc anode limitations adapted from Mainar et al., 2018a.

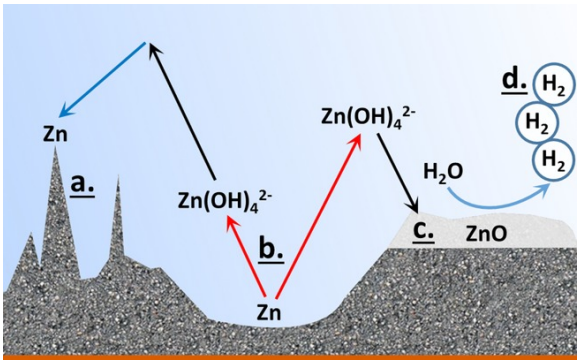

(b) Schematic representation of zinc-anode limitations. a) dendrite growth, b) shape change, c) passivation, and d) hydrogen evolution (HER) from Fu et al., 2017.

Figure 1.6: Zinc anode limitations in alkaline environment.

In the next subsections, the main problems related to metallic anode are explained. Solutions to these problems are discussed and more importantly, if challenges can be overcome to integrate this technology to current grids. As zinc metallic anode in KOH alkaline environment is the material under study in this manuscript, problems are explained specifically zinc anode.

1.5.1 Anode passivation

The deposit of a layer of inactive anode or electrolyte compounds on the surface of the anode is known as passivation. This layer reduces the activity of the anode as ions transported by the electrolyte cannot interact with the anode, and the anode cannot release its discharge products to the electrolyte, leading to anode failure.

Zinc anode capacity is known to decrease due to the formation of zinc passivation layer on the zinc surface (figure 1.6c). The origin of these passivation layers comes from a dissolution-precipitation mechanism [Cabot et al., 1993], in which zinc dissolves as zincate $Zn(OH)_4^{-2}$ but settles as a ZnO layer where OH^- concentration is locally low due to zincate saturation. Two layers of ZnO have been identified, as shown in figure 1.7:

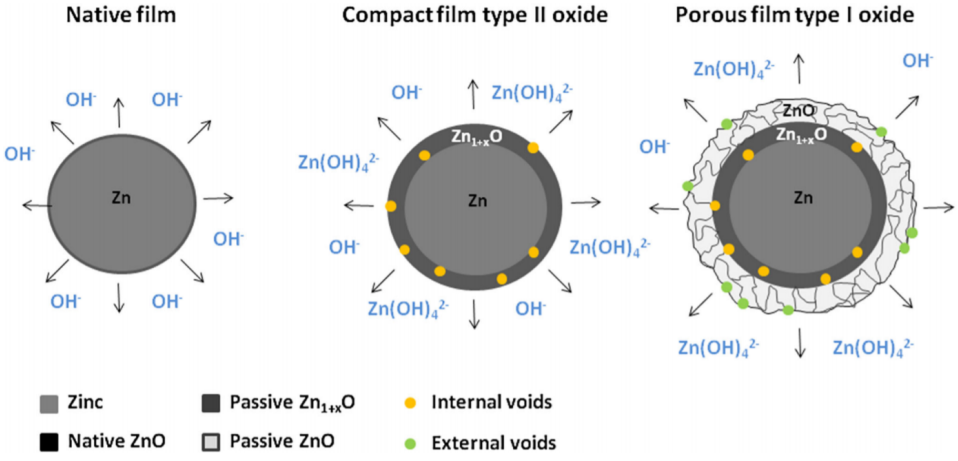

Figure 1.7: Passivation occurring in spherical zinc particles [Mele et al., 2017].

The passivation ZnO layers consist on a compact film (type II) and a porous precipitate film (type I). Furthermore, Mete et al. concluded that the main reason passivation layers formed was due to KOH electrolyte aging [Mele et al., 2017]. Finally, a failure of the zinc anode is expected with critical passivation as OH^- ions are blocked out from the anode.

The common approach to suppress passivation layers, is to use high concentrated alkaline electrolyte, increasing ZnO solubility. Other methods include the use of additives on the electrolyte, mainly surfactants [Mainar et al., 2018a]. Yang et al. [Yang et al., 2004], used

surfactant additives (sodium dodecyl benzene sulfonate SDBS) in alkaline electrolyte. This additive was reported to modify the anode surface, facilitating the diffusion of discharge product ($Zn(OH)_4^{-2}$) and reactant (OH^-).

Other methods to reduce passivation consist in anode surface protection. Mainar et al. [Mainar et al., 2018b] coated zinc pellets with Nafion®, reducing zinc dissolution rate and extending battery cycle life. On another study, Schmid and Willert-Porada coated zinc particles using different silica-based coatings that allowed a controlled zinc dissolution [Schmid et al., 2017b], reducing the formation of passivation layers.

1.5.2 Anode corrosion

Several metal anodes like Zn, Li, Al and Fe corrode in aqueous solution. In the particular case of zinc anode, hydrogen-evolution reaction (HER), also known as corrosion, is thermodynamically favoured as the Zn/ZnO stardard reduction potential at pH 14 is -1.26 V (equation **??**), is lower than that of the HER at pH 14 (equation 1.2):

$$\begin{aligned} HER : H_2O + 2e^- \Leftrightarrow 2OH^- + H_2 \\ (E^0 = -0.83\, V vs\ SHE) \end{aligned} \tag{1.2}$$

Therefore, a zinc electrode at rest will corrode and undergo self-discharge (equation 1.3).

$$Zn + 2H_2O \rightarrow ZnO + H_2 \tag{1.3}$$

The HER builds internal pressure as H_2 gas is generated and also leads to water depletion via electrolysis [Mainar et al., 2018a], generating OH^- concentration gradients.

Strategies to decrease HER concern the increase of the system overpotential to retard the reaction. Several organic compounds like surfactants are known to retard HER. In a different approach, it has been proven that presence of zincate ions reduces water activity, which at the same time reduces corrosion [Zhang, 1996]. Because of this, ZnO can be use as an additive to saturate the system on zincate ions. Additionally, when system is saturated with ZnO, the addition of inorganic salts like KF and K_2CO_3 delay HER [Mainar et al., 2018b,c; R. Mainar et al., 2016].

1.5.3 Dendrite growth

Dendrites are defined as sharp, needle-like metallic protrusions, formed during electrodeposition [Fu et al., 2017]. These form during zinc regeneration taking place when charging the battery. Several studies have observed that dendrite formation is directly related to the zinc reduction overpotential, and therefore current density and time [Fu et al., 2017; Wang et al., 2015; Zhang, 2009]. As observed in figure 1.8, different zinc deposits are found depending on the battery operation conditions (overpotential).

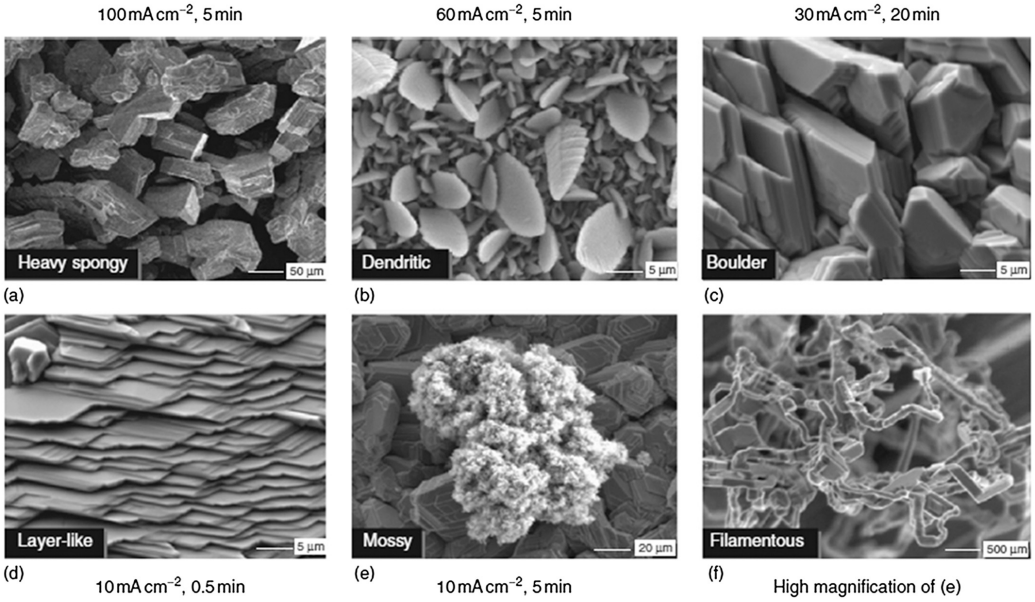

Figure 1.8: Different types of zinc deposit in alkaline conditions. a) Heavy spongy, b) Dendritic, c) Boulder, d) Layer-like, e) Mossy [Zhang, 2009].

These structures can affect negatively the battery because they can detach from the zinc anode leading to capacity losses. Moreover, if these structures have a dendritic form, they can pierce the membrane or separator and make contact with the cathode, resulting in a short circuit.

Several solutions have been explored with the outcome of improving battery cyclability. Among these, the use of a gelling agent to reduce/control dendrite growth and a continuous electrolyte flow throughout the battery have shown significant improvements in operation.

Several studies have been made with gelled polymer electrolytes (GPEs), which are a mixture of aqueous electrolyte (usually KOH for zinc-air batteries) and a gelling agent. A. Mohamad showed that using hydroponics gel not only reduced zinc shape change but also outperformed a traditional battery using alkaline aqueous electrolyte [Mohamad, 2020]. On the same approach, less needle-like structures were observed preparing a gelled KOH electrolyte using carboxymethyl cellulose [Puapattanakul et al., 2013; Yang et al., 2016], polyethylene glycol

[Banik et al., 2013; Mele et al., 2015], branched polyethylenimine [Banik et al., 2015], among others.

The second approach to reduce dendrites exposed in this work, concerns the utilization of a flowing electrolyte. This configuration is better known as **redox flow batteries** (RFBs). While using RFBs, current distribution is improved and zinc concentration gradients are reduced as alkaline KOH electrolyte is continuously flowing throughout the battery [Fu et al., 2017], avoiding zinc deposition problems, like dendrites and passivation layers. The concept of RFB is explained later (section 1.5.6) and then it is discussed how a static metal-air battery like zinc-air can become a flowing RFB system, including its advantages and challenges.

In the upcoming sections, advantages and disadvantages of two batteries are presented. The chemistries reviewed are Li-air, being the chemistry with the highest specific energy, and Zn-air, being the most developed metal-air battery and the object of study in this research.

1.5.4 Lithium - air battery

Lithium - air batteries have a great potential to store energy, its theoretical energy density is the highest among the metal-air batteries, comparable to gasoline (13000 Whkg^{-1}). Studies made on lithium - air batteries have exhibit 5-10 times greater energy density (1300 Whkg^{-1} in alkaline electrolyte), when compared to Li-ion batteries (200-250 Whkg^{-1}) [Rahman et al., 2013; Soloveichik, 2011].

Because lithium metal is very reactive in aqueous electrolyte, undergoing surface degradation and forming insoluble lithium salts, research has focused on non-aqueous electrolytes [Lee et al., 2011b; Zhang et al., 2010]. Nonetheless, as pointed out by Zhang et al., several limitations including the moisture uptake and CO_2 intake from the air hinder the performance of the battery. In addition, the poor solubility of lithium reaction products happening in non-aqueous Li-air battery are unavoidable in real conditions [Zhang et al., 2010], limiting its development.

Recently, PolyPlus Battery company developed a method in which lithium metal is protected and can be enabled in aqueous electrolyte [Visco et al., 2014]. Lithium electrode is protected by high Li^+-conductivity solid electrolyte that chemically isolate lithium metal from the external environment (figure 1.9). With this configuration, an energy density of 800 Whkg^{-1} was obtained.

As depicted in figure 1.9, metallic lithium is protected with a solid electrolyte membrane which chemically isolates the anode metal electrode from the electrolyte and positive electrode half-cell. When using this configuration the electrolyte can be either acidic or basic. This approach has also been extended to non aqueous Li-air batteries.

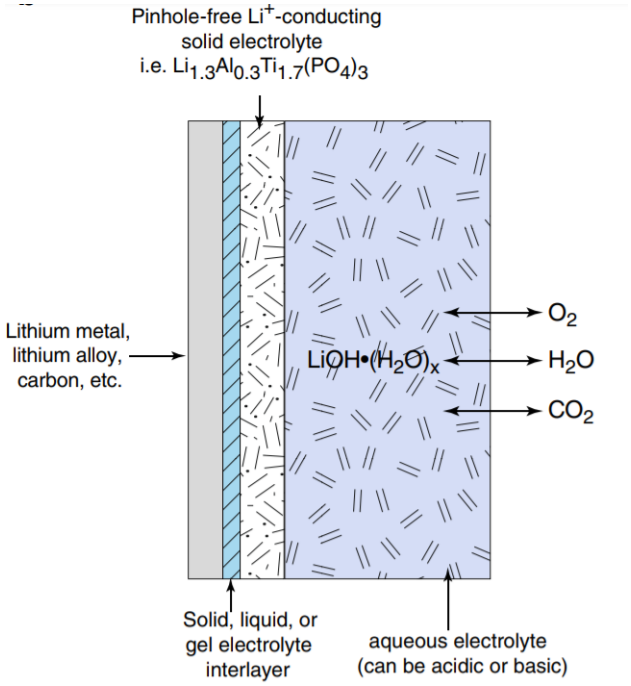

Figure 1.9: Li-air cell employing protected lithium electrode (PLE) [Visco et al., 2014].

Finally, Li-air battery shows promising results but technology is still in an initial stage, issues to be integrated in the power grid have to be still solved, as they have not shown capacity for high power density and extended cycling [Imanishi et al., 2019].

1.5.5 Zinc - air battery

Zinc - air batteries is one of the most mature technologies available. Its working principle was discovered in 1868 by Georges Leclanché , but it was until 1932 that this chemistry was first commercialized. The zinc-air battery consists in a zinc metallic anode, an oxygen cathode with a bi-functional catalyst, a membrane or separator and electrolyte (figure 1.10).

Rechargeable zinc-air batteries are a promising technology because zinc is a readily available in earth crust and because its high energy density (table 1.1), with a specific energy density of 1312 Wh/kg, at least 5 times higher than the one of a lithium-ion battery. Moreover, zinc low reactivity allows handling in oxygen and humid atmosphere [Mainar et al., 2018d].

Generally, secondary metal-air batteries with Zn, Al and Fe anodes use aqueous alkaline electrolyte to avoid corrosion and limit anode self-discharge [Mainar et al., 2018b; Visco et al., 2014]. Usually, concentrated potassium hydroxide (KOH) is used as electrolyte due to its superior ionic conductivity compared to sodium hydroxide ($NaOH$) or lithium hydroxide ($LiOH$).

Zinc-air battery is composed by an metallic zinc anode or foil, an air cathode, membrane or separator dividing the anode from the cathode compartment, and electrolyte, usually KOH ranging from 6 to 10 M KOH. In figure 1.10, the mechanisms of reaction during discharge are presented.

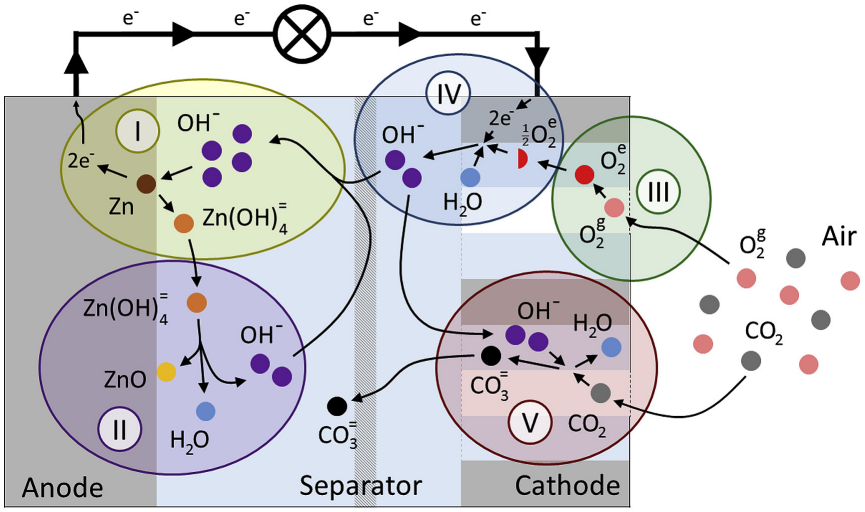

Figure 1.10: Reactions during discharge in a primary zinc-air cell [Stamm et al., 2017].

The discharge of the battery happens as follows. In a first stage (I), zinc dissolves into aqueous electrolyte producing zincate ionic species ($Zn(OH)_4^{-2}$) and generating electrons that will travel to the anode. Next, ZnO precipitates as production of the discharge (II). On the cathode side, oxygen enters through gas diffusion layer (III) and its reduced in the cathode (IV). In parallel, carbonate can form from the intake of atmospheric CO_2 [Stamm et al., 2017]. During charging, the reactions occur in the opposite direction, in which anode is reduced and cathode oxidized. The reactions happening in alkaline environment are available in chapter six.

Zinc-air is an established technology, with high power density that can be used for large scale energy storage for long durations. Environmental impact is low as zinc can be easily recycled. However as mentioned in section 1.5, several problems limit rechargeability, reducing cycling efficiency to values of around 50 %. Even with this limitations, several companies have deployed rechargeable zinc - air batteries, like Zinc8 (www.zinc8energy.com), with competitive storage costs for long duration application in the order of 45 $/KWh for a modular design in which zinc is regenerated externally to the power stack. Similarly, NantEnergy (www.nantenergy.com) offers solutions for remote off-grid areas. Modular zinc-air batteries are also combined with Li-ion batteries for a more flexible design.

As discussed in section 1.5, several of the problems related to zinc anode limitations and rechargeability can be diminished significantly by changing the design of a traditional zinc - air battery towards a flowable design, being RFBs.

This technology was developed in late 20th century and since then, several research groups and companies have shown interest in developing this technology for stationary energy storage. The working principle of RFB is explained in the following section.

1.5.6 Redox flow batteries RFBs

RFBs have been gaining attention in recent years because of its design flexibility and scalability [Wei et al., 2017]. As in standard batteries, there is the choice among different redox couples that can be used to perform the redox reaction and the transfer of electrons. The working principle and the design of a RFB is displayed in figure 1.11:

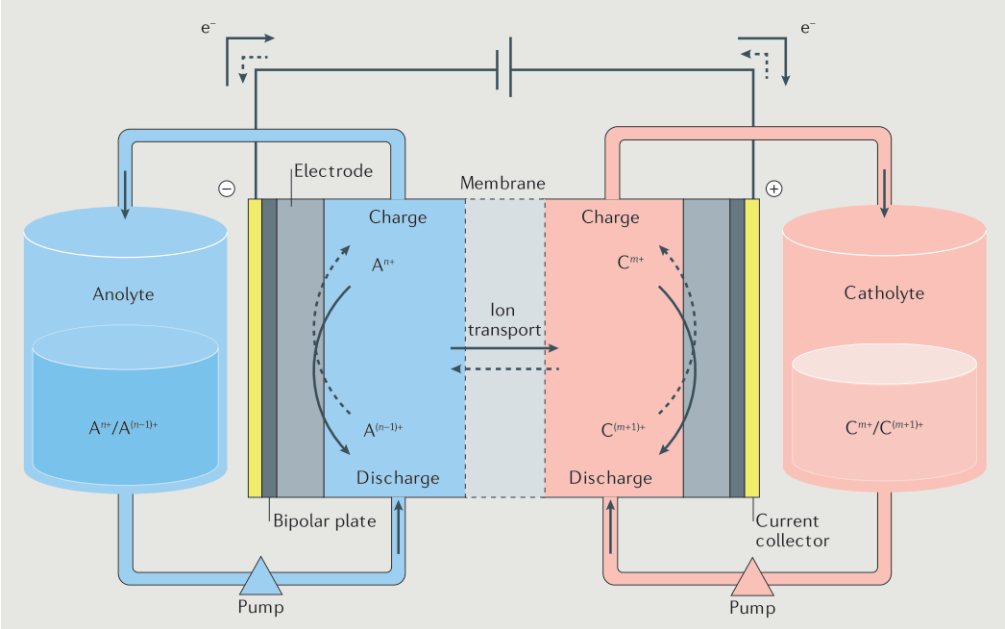

Figure 1.11: RFB configuration from [Park et al., 2016].

Energy is stored in two redox couples dissolved in electrolyte, being the anolyte and catholyte, in the anode and the cathode compartment, respectively. These electro-active solutions are continuously pumped throughout the stack, where redox reactions occur on the active electrode surface [Park et al., 2016], producing electricity. Electrolyte compartments are separated by an ion conductive membrane or microporous separator, where ionic products from the redox reactions are conducted through [Gubler, 2019]. In figure 1.11, the pathway during the discharge and charge are represented by solid and dashed lines, respectively. As in regular batteries, during the discharge the the oxidation takes place at the anode and the reduction on the cathode, producing a flow of electrons from the anode to the cathode. During charging, the process occurs in the opposite sense.

The main characteristic of RFB is that electrolyte is separated from electrode, and stored in external tanks, as observed in figure 1.11. Consequently, the energy capacity depends on the volume of electrolyte stored externally, and the power output depends on the active area in the stacks. In this way, energy is decoupled from power, allowing design flexibility to meet specific demands. Moreover, as tanks are accessible, electrolyte replacement or resizing is possible.

RFBs have been a subject of study since late 20th century. First RFBs were studied in pure aqueous media. In 1970s, NASA developed an iron-chromium flow battery, but low reversibility of chromium redox couple and low specific energy (15 Wh kg^{-1}) hindered its progress [Huang et al., 2015; Weber et al., 2011].

With the current technology, RFBs are considered as long-term energy storage devices for large-scale applications, with output power ranging from 10 kW - 10 MW [Argyrou et al., 2018]. Nowadays, the most mature technology is the all-vanadium RFB. This technology was developed in the 1980s by Skyllas-Kazacos et al. [Skyllas-Kazacos et al., 1987, 1986]. This technology is explained shortly in the next section.

1.5.6.1 All-Vanadium RFB

One of the great advantages of the all-Vanadium RFB is that the battery uses the same element in both compartments, avoiding the problem of cross-contamination. Cross-contamination is the process in which redox-active species in the electrolyte travel from one electrode compartment to the other, inducing capacity losses [Lourenssen et al., 2019]. This issue has been addressed by producing more efficient ion-selective membranes [Gubler, 2019]. However, as all-Vanadium RFB uses the same material in different oxidation states in both compartments, crossover issues are significantly reduced. The redox couples are $V^{2+/3+}$ and $V^{4+/5+}$ (otherwise VO^{2+}/VO_2^+), which are dissolved in sulphuric acid (H_2SO_4) electrolyte. The reactions taking place in the battery are the following:

$$Cathode: \ VO_2^+ + 2H^+ + e^- \underset{\text{charge}}{\overset{\text{discharge}}{\rightleftharpoons}} VO^{2+} + H_2O \qquad (E^0 = 1.0 \, Vvs \, SHE) \tag{1.4}$$

$$Anode: \ V^{2+} \underset{\text{charge}}{\overset{\text{discharge}}{\rightleftharpoons}} V^{3+} + e^- \qquad (E^0 = -0.26 \, Vvs \, SHE) \tag{1.5}$$

$$Cell\ reaction: VO_2^+ + V^{2+} + 2H^+ \underset{\text{charge}}{\overset{\text{discharge}}{\rightleftharpoons}} VO^{2+} + V^{3+} + H_2O \quad (E^0 = 1.26\ Vvs\ SHE) \tag{1.6}$$

Nowadays, there are several prototypes and facilities worldwide using all-vanadium RFB as ESS with a power rating in the range of MW [Shigematsu, 2019]. Some examples of commercialized vanadium RFBs are Invinity Energy systems (www.invinity.com), offering configurations with a power output of 78 kw - 10 MW that can be used for grid support; VoltStorage (www.voltstorage.com) offering the same technology for private households with thanks of 220 liters delivering a power of 1.5 kW.

However, vanadium has some drawbacks that limits its application and concerns its development in the future. These are mainly the vanadium solubility and its market-dependent price.

Vanadium solubility is directly related to system energy density. V^{5+} shows a limited solubility at different temperatures. At less than 10 $°C$, V^{2+} V^{3+} and V^{4+} at a 2M concentration precipitate in a 5 M sulfuric acid [Choi et al., 2017]. However, at 40 $°C$, a 2.0 M solution of V^{5+} shows accelerated rate of thermal precipitation [Huang et al., 2015]. These limits the operation of all-Vanadium RFB to temperatures between 10-40 $°C$ and to lower vanadium concentrations to avoid precipitations of any kind [Lourenssen et al., 2019].

With the current policies and the high price of stored energy ($\approx USD$ 0.10 $kW^{-1}h^{-1}$) [Kear et al., 2012], reduction in costs are mandatory to compete with other ESS, even if several indicators confirm that an energy transition will happen, where ESS will be enabled as main characters to boost renewables [Gielen et al., 2019]. However, fluctuations in vanadium price, dictated by the demand of other industries (i.e. steel manufacturing) [Brushett et al., 2020], make availability and cost/revenue predictions more difficult.

Many chemistries and redox pairs have been investigated since the development of the all-Vanadium RFB [Park et al., 2016]. One of the most interesting technologies is the hybrid zinc-air RFB, maintining the advantages of a RFB combined with the readily available, high energy density zinc anode material.

1.5.6.2 Zinc - air RFB

As discussed in section 1.5.5, zinc-air rechargeable batteries are interesting for energy storage because of the high theoretical energy density inherent from metallic Zn/O_2 redox couples.

When adopting a RFB configuration, some of the drawbacks limiting the zinc anode like passivation, dendrites and corrosion, can be significantly reduced, as pointed out by Fu et al. and Han et al. [Fu et al., 2017; Han et al., 2018].

For metal-air RFBs, there are two possible configurations, as observed in figure 1.12.

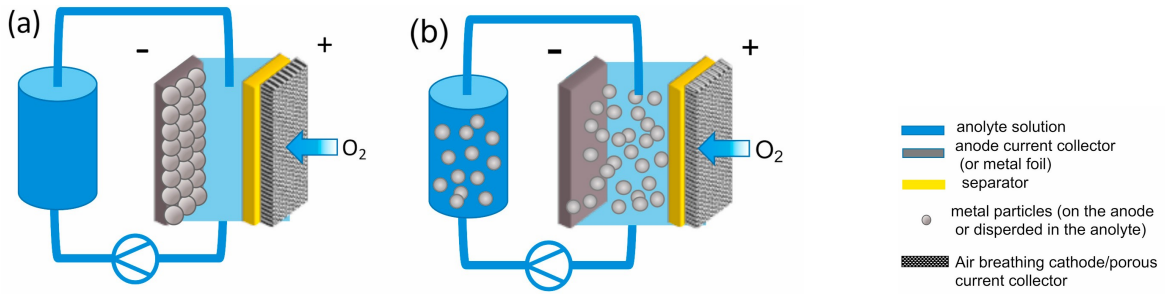

Figure 1.12: RFB structure diagrams with anode circulating. a) Air breathing metal-air flow battery with metal anode and anolyte solution flow, b) Air breathing metal-air flow battery with metal slurry anolyte, with metal anode and oxygen cathode. Adapted from [Sánchez-Díez et al., 2021].

The main difference with a regular RFB, is that just one half-cell (in the case of zinc-air the anode) will adapt a redox flowing couple whereas the positive electrode is replaced by oxygen/air. By replacing the positive tank by an oxygen gas diffusion electrode, the weight and the volume of the battery are reduced, contributing to a higher energy density when compared to other RFB systems [Han et al., 2018].

There are mainly two designs for zinc-air RFBs. The first one is the one having fixed zinc metal anode located in the cell and a flowing anolyte carrying active redox species (figure 1.12a). Zinc discharge products are recirculated avoiding zinc anode limitations (figure 1.6), increasing battery discharge capacity and cycle life. This configuration so far has been the more studied and developed [Bockelmann et al., 2016; Fu et al., 2017; Han et al., 2018; Puapattanakul et al., 2013; Wang et al., 2015 and citations therein].

The second design consists in the use of a metal slurry (figure 1.12b) in which metal dissolution and precipitation occurs in the flowing anolyte, reducing localized passivation and dendrite formation [Fu et al., 2017; Sánchez-Díez et al., 2021]. Moreover, the utilization of zinc particles allows higher discharge rates as passivation is reduced [Zhang, 1996].

In some cases, aged anode electrolyte slurry can be recharged mechanically replacing it with fresh slurry [Lao-atiman et al., 2019; Mele et al., 2017; Pei et al., 2014]. In this way, slurry can be regenerated externally [Zhang, 2009], without affecting battery performance.

The electrode slurry anolyte concept was developed in 2011 and it is also known as semi-solid flow cell (SSFC) [Duduta et al., 2011]. Main advantages are an increase of energy density and electro-active material utilization. Moreover, there is not a solubility limit like in all-Vanadium RFBs [Choi et al., 2017], so the energy density can be theoretical increased by suspending higher particle concentrations. Nonetheless, slurry viscosity is a main concern regarding battery efficiency [Barton et al., 2018] and clogging of the flow cell.

Flowing metal-air batteries are still under development, specially charging of the battery where zinc electrodeposition can clog the battery in flow frames [Choi et al., 2020b], aside from membrane/separator development and the challenging bifunctional air electrode [Guo et al., 2019], allowing electrical rechargeability.

The development of metal-air RFB is still in its early stage, but nevertheless, this configuration possess several advantages that can earn to this technology a bigger market share in the ESS market. Some of the features are summarized here:

- Reduction of electrolyte concentration gradients
- During charging, more compact deposition of zinc, suppression of dendrite growth
- When compared to static systems, energy is decoupled from power, allowing a flexible design
- Application in large-scale energy storage, stationary plants and electrical vehicles
- Technology in early stage

For the large-scale energy storage, it is then clear that a RFB approach is more adequate than the static system. The electrolyte and anode qualities mentioned are vital to store energy and to provide a long battery life cycle.

1.6 Conclusions

Several ESS have been discussed in these chapter, exposing its advantages and limitations to be integrated in current grids. The driving force of ESS is the integration of intermittent renewable sources to the electrical grid, and the response measured in discharge time and capacity allows a general assessment of the available ESS (figure 1.3).

Special attention is given to metal-air batteries, where synergistic approach of abundant high energy density materials are combined with RFB design.

A summary of some of the technologies reviewed in this chapter is found in table 1.2, exposing each system characteristics and technology readiness level.

Technology option	Maturity	Capacity (MWh)	Power (MW)	Duration (hours)	% Efficiency (total cycles)	Power cost ($/kW)	Energy cost ($/kWh)
CAES (aboveground)	Demo	250	50	5	(>10 000)	$1950 - 2150$	$390 - 430$
Advanced Pb-acid	Demo	$3.2 - 48$	$1 - 12$	$3.2 - 4$	$75 - 90$ (4500)	$2000 - 4600$	$625 - 1150$
Na/S	Commercial	7.2	1	7.2	75 (4500)	$3200 - 4000$	$445 - 555$
Zn/Br flow	Demo	$5 - 50$	1-10	5	$60 - 65$ (>10 000)	$1670 - 2015$	$340 - 1350$
V redox flow	Demo	$4 - 40$	1-10	4	$65 - 70$ (>10 000)	$3000 - 3310$	$750 - 830$
Fe/Cr flow	RD	4	1	4	75 (>10 000)	$1200 - 1600$	$300 - 400$
Zn-air	RD	5.4	1	5.4	75 (4500)	$1750 - 1900$	$325 - 350$
Li-ion	Demo	$4 - 24$	$1 - 10$	$2 - 4$	$90 - 94$ (4500)	$1800 - 4100$	$900 - 1700$

Table 1.2: Available energy storage options for utility transmission and distribution grid support [Dunn et al., 2011].

Among the different ESS, it is observed that zinc - air battery is one of the technologies offering economically accessible energy storage in the order of 325-350 $\$/kWh$, at least 3 times lower when compared to Li-ion [Dunn et al., 2011]. The price of energy storage with RFB is likely to decrease as integration of intermittent renewable sources to the electrical grid is likely to increase with current energy policies [Sisternes et al., 2016]. However, the problems related to anode stability and cyclability have to be improved with the purpose of becoming the next benchmark in electrical storage systems. Because of these reasons, more research is needed to foster this technology to a higher technology readiness level.

The work that will be presented in this thesis concerns the development of a zinc - air RFB. Furthermore, in order to reduce significantly the formation of passivation layers and dendrite formation, the formulation of a zinc anode suspension is investigated to be used in a RFB.

The semi-solid anode suspension consists in metallic zinc particles suspended in alkaline electrolyte. This material is expected to display a complex flow behaviour during the recirculation of the suspension through the battery. To understand how the sample will behave under flow, rheology is used to formulate and characterize the proposed suspension.

In the next chapter, the focus is given to the rheology of suspensions, specifically in the regime in which zinc slurry suspension are found. Moreover, rheometric tools that can be used to improve the formulation and development of zinc slurries for RFB are discussed.

CHAPTER

TWO

RHEOMETRY OF SUSPENSIONS

As discussed in the previous chapter, materials for batteries have to be chosen according to its chemical potential, redox pairs reversibility, chemical stability, among other electrochemical properties. In addition, when considering redox flow batteries (RFBs), another variable is introduced to the problem, being the viscous behaviour of the electro active material. Aqueous batteries may have a simple flow behaviour (i.e. Newtonian fluid), but systems become more complex when dealing with semi-solid electrodes (slurries). In the latter, particles are suspended in electrolyte medium, showing a complex flow behaviour (non-Newtonian fluids). This is the object of study in the zinc slurry - air RFB.
In this chapter, the rheometric tools that are used to analyse fluids viscous behaviour are introduced. Then the rheology of suspensions is introduced highlighting the elements that will be important for our slurry samples.

"...for the Greek philosopher Heraklitus was literally correct when he said that "everything flows". It is therefore necessary to limit our discussion by excluding the flow of those things which we are accustomed to refer to as fluids, the pure liquids and gases. But the circle of our lives is not concerned principally with the fluids, even air and water, but with plastic materials." - Eugene C. Bingham.

Contents

2.1 Introduction

In order to formulate a suspension to be used in a zinc slurry - air RFB, there is a trade off to take into account, being the conductive network properties and its viscous behaviour. Specifically, sufficient active material needs to be used to build a conductive percolated network, but the viscosity of this network has to remain sufficiently low so the slurry can be pumped throughout the battery. In the zinc - air battery, the problem is even more complicated because the operating conditions occur in highly alkaline medium (pH $\approx$ 14). To assess the viscous behaviour of the electro active materials used in a zinc slurry -air RFB, a rheological approach is used. An introduction to the rheology of suspensions and its scope are discussed in this chapter.

The term rheology was coined in 1929 by Eugene C. Bingham and the field of study is the deformation of materials under a given stress [Wilson, 2018]. The necessity of this physics branch appeared from the need to characterise materials in a category between Hookean elastic solids and ideal Newtonian viscous fluids, as it is the case for slurry suspensions used in RFBs. As Bingham noticed back in early 20th century, most of the materials surrounding us belong to this category. In addition, flow behaviour of these materials will not only depend of its intrinsic properties, but also of external conditions like temperature, pressure, pH and others.

As a result different material responses can be obtained from exerting a given force on them, usually evaluated as a stress τ.

Recalling the basics of rheology, let us consider a simple shear flow of a homogeneous continuous material between two infinite plates separated by a distance h, in which the upper plate moves and the lower plate remains static, as in figure 2.1:

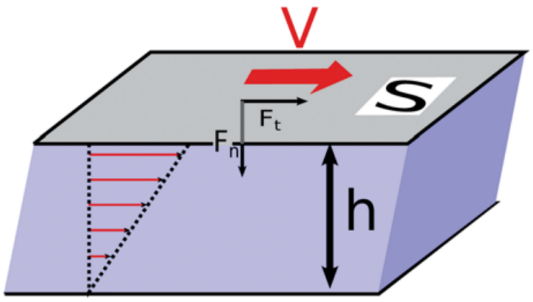

Figure 2.1: Ideal shear flow between two plates with surface S, separated a distance h. The upper plate moves at a velocity V, parallel to imposed force F_t. Fluid is confined by a force F_t. Adapted from [Mansard et al., 2012].

In this configuration, the material is sheared when a force $\vec{F}$ acts on the upper plate, moving at a velocity V. The material starts to deform into a laminar flow in which the fluid moves in a layered configuration as observed in figure 2.1. The force $\vec{F}$ has two components, one tangential F_t and one normal F_n, as represented in figure 2.1. In this ideal geometry, the shear stress is obtained by $\tau = F_t/S$ and the velocity of deformation, denominated shear rate is given by the expression $\dot{\gamma} = V/h$. Finally, the shear viscosity, indicating the resistance of the fluid to undergo deformation follows Newton law:

$$\tau = \eta \cdot \dot{\gamma} \tag{2.1}$$

Where η is the viscosity in Pa s.

The viscosity of some materials is constant independently of the shear rate at which they are studied. These are defined as Newtonian fluids and some examples include water, mineral oil, ethanol, glycerol, acetone, among others. Nevertheless, it exists a vast category of fluids in which the shear stress and shear rate in the material have a non-linear relation. In other words, viscosity is variable and will depend on the shear rate applied to it. These materials are defined as non-Newtonian and the most common flow behaviours are shown in figure 2.2.

It is then observed that contrary to Newtonian fluids, where shear stress is directly proportional to shear rate (constant slope of curve A in figure 2.2), the viscosity of non-Newtonian

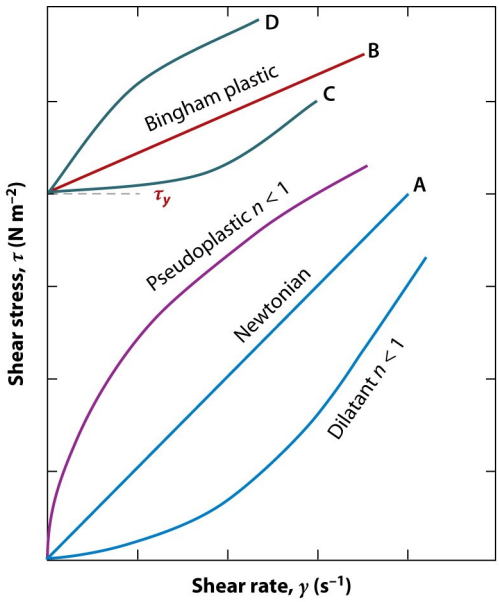

Figure 2.2: Different shear stress vs shear rate flow behaviours [Boger, 2013].

fluids will depend on the shear rate applied.

Non-Newtonian fluids can be modelled as power-law fluids at a non-zero shear rate using the following relation:

$$\tau = K \cdot \dot{\gamma}^n \tag{2.2}$$

This power-law is otherwise known as the Ostwald-de Waele relationship, in which K is the consistency index (in $Pa \cdot s^n$) and n is the flow index.

The most common non-Newtonian behaviours are briefly explained in the following sections. In particular a detailed description of yield stress fluids is provided, a behaviour that is often found in suspensions, like the zinc anode slurry.

2.2 Rheological flow behaviours

2.2.1 Shear thinning behaviour $n < 1$

Shear thinning fluids, also known as pseudoplastic, are described by a flow index $n < 1$ (figure 2.2). The viscosity of these fluids will decrease with increasing shear stress. The origin of this phenomena is a result of microscopic structure rearrangements obtained at a given stress or shear rate.

For instance, shear thinning behaviour can be observed in polymeric solutions. The breakdown of the polymer chain entanglements occurs when shear rate is increased, leading to a chain alignment in the direction of the deformation [Liu, 1989; Milner, 1996; Xia et al., 1991]. The chain rearrangement is in a better disposition to flow and thus, as shear rate is increased, viscosity decreases.

This behaviour is also observed in self-assembling hydrogels. The network found in this hydrogels is an effect of competing attractive and repulsive forces. When an external force as shearing is applied to these gels, network breaks leading to a viscosity decrease [Guvendiren et al., 2012; Lang et al., 2019]. When shear force is removed, hydrogels are able to self-assemble again, building a high viscosity network. Some examples are protein-based hydrogels, colloidal systems and block copolymers among others.

The similar mechanism can be found in suspensions. The shear thinning is caused by the formation of ordered domains in which the suspension is able to flow more easily [Foss et al., 2000; Mongruel et al., 1999; Poslinski et al., 1988]. Such is the example of carbon black suspensions, in which increasing shearing results in the break up of agglomerates from micro structures to more elementary structures of smaller size.

2.2.2 Shear thickening behaviour $n > 1$

Shear thickening fluids, also known as dilatant, are described by a flow index $n > 1$ (figure 2.2). In this type of fluids the viscosity increases when the shear force applied increases. This behaviour is less frequently observed but is common of colloidal suspensions like cornstarch-water system [Dail et al., 1990; Madraki et al., 2017], latex suspensions [Rodriguez et al., 1992; Wagner et al., 2009], and in the high deformation regime of non-Brownian particles [Cwalina et al., 2016; Dratler et al., 1997; Gopalakrishnan et al., 2004; Hermes et al., 2016].

It was observed that in colloidal systems, there is a critical shear rate in which particles adopt a jammed configuration, where they interact through physical contact and clustering. The increase of friction forces will ultimately lead to an increase in viscosity [Hoffman, 1998]. In addition, the critical shear rate at which viscosity starts to increase is lowered when large non-Brownian particles are added to the system [Madraki et al., 2017].

2.2.3 Yield stress fluid

Yield stress fluids are non-Newtonian fluids with a dual behaviour. The yield stress τ_y is defined as the stress that need to be overcome for flow to take place. Yield stress is a macroscopic property resulting from structural microscopic interactions forming a network that will break

once the yield stress is overcome. In these lines, if a fluid is subjected to a stress τ that is lower compared to its characteristic yield stress τ_y, the sample will not flow and will behave as an elastic solid. However, if the stress τ applied is higher than its yield stress $\tau > \tau_y$, the sample will deform and be subjected to flow [Coussot et al., 1996; Magnin et al., 1987]. This type of fluids are illustrated in previous figure 2.2, in which the yield stress τ_y is indicated as a non-zero stress at the zero shear rate. Curve B is the simplest fluid representation of this type of material known as a Bingham fluid. Curves D and C follow other type of behaviour that can be represented with non-linear models.

Different models have been proposed to analyse these types of fluids, amongst them the most used are the Herschel-Bulkley, the Casson and the Bingham model [Macosko, 1994]. Nonetheless, the Herschel-Bulkley model has been the most used in the rheological community in the last two decades [Frigaard, 2019], accounted for describing flow behaviour by considering 3-parameters that are related to fluid properties, being the following:

$$\begin{aligned} \dot{\gamma} &= 0 \;\; if \;\; \tau < \tau_y \\ \tau &= \tau_y + K\dot{\gamma}^n \; if \;\; \tau > \tau_y \end{aligned} \tag{2.3}$$

Where τ_y is the yield stress, K is the consistency index and n is the flow index. When applying a stress τ below the τ_y, material will not flow exhibiting a solid elastic behaviour. Contrarily, if the stress τ is higher than the τ_y, the material will flow following power-law behaviour, i.e. shear thinning if $n < 1$. These parameters have to be determined experimentally and are specific of a given material.

These types of fluids are of great interest for several industries, like food [Deshpande et al., 2010; Missaire et al., 1990; Yoo et al., 1995], well drilling [Briscoe et al., 1994; Clark, 1995; Hermoso et al., 2012], construction materials [Coussot et al., 1996; De Larrard et al., 1998; Hu et al., 1996], paints [Balmforth et al., 2014; Cohu et al., 1995; Hester et al., 1997], energy storage [Bossis et al., 1997; Pieczyska et al., 2005; Smith et al., 2014], and others.

The existence of a yield stress has been a debate for rheologists, as some authors state that all materials can flow if the experimental time is long enough [Barnes, 1999]. From an experimental point of view, the determination of yield stress is not always straightforward [Dinkgreve et al., 2016; Møller et al., 2006], and the problem comes from the experimental artefacts and the time scale at which the steady state is obtained [Cheng, 1986; Coussot, 2018]. Nevertheless, a yield stress inherent of the sample in question can still be obtained under well-defined experimental conditions [Caton et al., 2008; Dinkgreve et al., 2016; Ovarlez et al., 2013].

Yield stress is a macroscopic property and its origin lays in the material structure. Over time, two large categories encompassing yield stress fluids have been proposed, being colloidal glasses [Coussot et al., 2002; Piau, 2007; Sollich et al., 1997], which are systems dominated by repulsive interactions, and colloidal gels [Piau et al., 1999; Pignon et al., 1997], systems dominated by attractive interactions. A rough categorization of these materials is presented in figure 2.3.

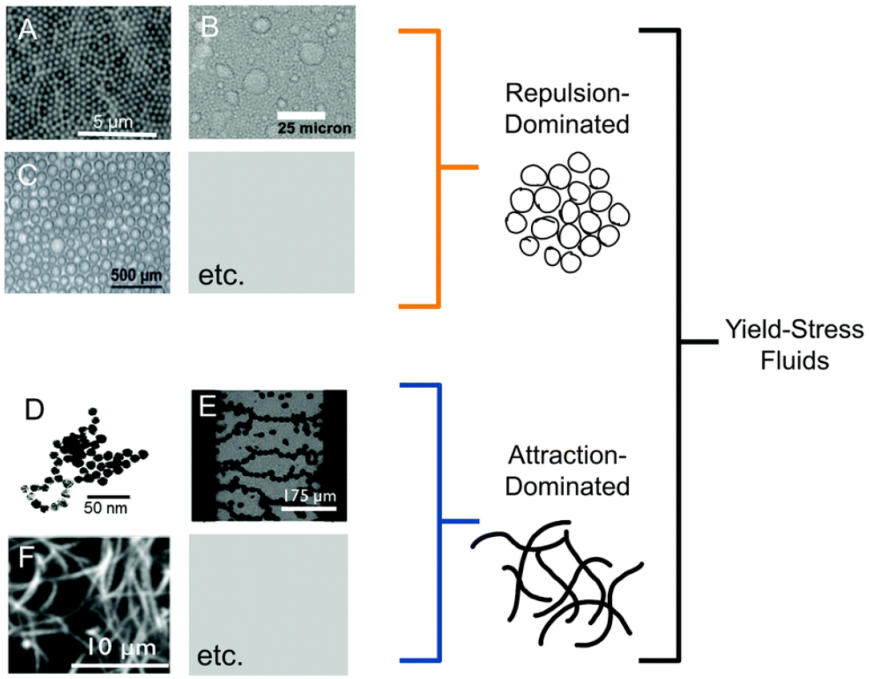

Figure 2.3: Classification of yield stress fluids. Examples shown are (A) particulate suspensions, (B) emulsions, (C) foams, (D) particulate gels, (E) electro/magneto-rheological fluids, and (F) fibre gels extracted from the paper of [Nelson et al., 2017].

For the first category, repulsion forces are the result of a jammed configuration, as observed in the graphic representation for the repulsion-dominated systems. In this systems, the elementary structures are densely packed resulting in a jammed system as observed in the insets A, B and C in figure 2.3. A system is said to be jammed when a volume concentration of elementary structures ϕ is attained in which colloidal or non-colloidal structures squeeze each other (repulsion). The resulting network will only flow if the stress applied to it is greater that the network yield stress. In this category, some examples of yield stress fluids are colloidal glasses [Petekidis et al., 2004], granular suspensions like slurries and glass beads [Stickel et al., 2005], microgels in water like Carbopol® [Piau, 2007], among others.

For the second category, attractive microstructures build a network by resisting to be pulled apart from their neighbours, as observed in the insets D, E and F of figure 2.3. When the shear stress is stronger than the attractions, the network will eventually be deformed and flow will be established. Some examples are colloidal gels like bentonite and Laponite® [Moller et al., 2009], magneto- and electro-rheological fluids, like titanium dioxide in silicone oil [Liu et al., 2010], and associating fibrils, like xanthan gum in water [Rochefort et al., 1987]. More examples can be found in the papers literature cited here [Moller et al., 2009; Nelson et al., 2017].

Thence, the structures arrangements presented above, based on repulsion-dominated and attraction-dominated networks, give the origin to a yield stress behaviour. In some cases, this behaviour is sought for an specific application, but in other cases the yield stress is just a result of a formulation used for a given application.

In the thesis work, the use of yield stress materials is considered for two main reasons. The first being to avoid the sedimentation of zinc particles: network yield stress has to be higher than the stress exerted by the dense zinc particles, avoiding sedimentation. The second reason is to build a percolated network with the zinc particles to enhance conductivity, following a repulsion-dominated structure (particulate suspensions in figure 2.3). It is highlighted again that the trade off between conductivity and viscosity is critical, as a concentrated zinc slurry may be extremely difficult to flow through a RFB cell.

In order to characterise the rheological behaviour of a material, different rheometrical techniques are available. Some examples are rotational rheometry, capillary viscometers, microfluidics, microrheology, and others. The flow occurring in specific geometries has been well defined allowing to characterise viscous behaviour by using rotational rheometry. This approach is discussed in the next section.

2.3 Rotational rheometry

In the previous section, the ideal scenario of a sample being sheared between two infinite parallels plates in the absence of gravity was presented (figure 2.1). In practice, there are available geometrical configurations used to evaluate the flow behaviour of a given fluid in rotational rheometers. The most common geometries are (i) parallel plates, (ii) cone and plate and (iii) concentric cylinders. Furthermore, the expressions to obtain shear stress τ and shear rate $\dot{\gamma}$ are dependent of the geometry, so individual solutions are proposed for each viscometric flow.

In a general way, rheometers use the information of the shearing geometry to calculate shear stress and shear rate. The viscosity of a given fluid is thus calculated as follows:

$$\eta(\dot{\gamma}) = \frac{\tau(\dot{\gamma})}{\dot{\gamma}} = \frac{\Gamma \cdot K_\tau}{\Omega \cdot K_{\dot{\gamma}}} \tag{2.4}$$

Where rheological properties τ and $\dot{\gamma}$ are determined from the torque Γ and rotational speed Ω obtained from the rheometer. The geometrical shape stress and strain constants K_τ and $K_{\dot{\gamma}}$, respectively, correspond to the shearing geometry characteristics.

In each of the geometries, a simple flow is considered by making following ideal assumptions: (i) the fluid sheared is homogeneous, (ii) there are no edge/interfacial effects, (iii) inertia effects are negligible, (iv) the flow is laminar, isothermal and in steady state, (v) the rotational velocity Ω is constant, (vi) conservation of mass and momentum is applied (Navier-Stokes equation) [Macosko, 1994]. By reuniting these hypothesis, the flow within a specific geometry can be defined in terms of shear rate and shear stress.

The advantages and limitations of the main rotational geometries are presented in the next section. To ease the explanation, it is considered that geometries are studied in a stress-controlled rheometer, meaning that the torque/shear stress is applied and the rotational speed/shear rate is measured.

2.3.1 Classic rotational geometries

2.3.1.1 Flow between a cone and a plate

The cone and plan geometry consists in a cone of radius R, with a small angle (usually $\theta_0 < 6°$), as displayed in figure 2.4. The free surface is spheric and the flow can be then described in spheric coordinates (r, θ, φ).

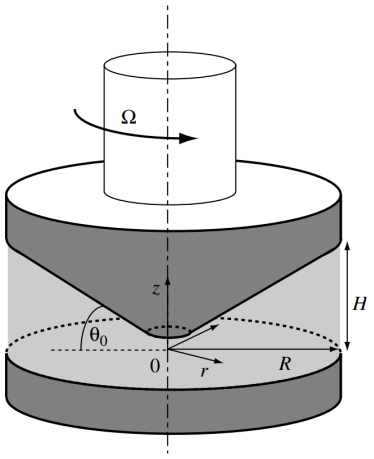

Figure 2.4: Cone and plate viscometric flow geometry. Scheme taken from [Coussot, 2005].

It is highlighted that the cone is truncated to avoid contact with lower plate leading to additional friction, and therefore it defines the gap of the geometry. The flow in the truncated zone is neglected, and its effect is reduced as the truncation diameter decreases [Coussot, 2005].

The shear rate within this geometry is calculated with the following expression:

$$\dot{\gamma} = \frac{\Omega}{\theta_0} \tag{2.5}$$

And the shear stress is calculated as follows:

$$\tau = \frac{3\Gamma}{2\pi R^3} \tag{2.6}$$

The advantage of this geometry is that the shear rate is uniform and constant within the geometry gap, as observed in equation 2.5. Therefore real viscosities are obtained with this geometry. The angle θ_0 is fixed so the ratio of the fluid thickness and R is $\ll 1$, avoiding localised shearing across the gap. Moreover, when using a cone with a lower angle θ, higher shear rates are attainable.

Some of the limitations of this geometry are the folloiwng. The sample in the geometry can be subjected to solvent evaporation as the free surface area is in contact with the atmosphere. When solvent is evaporated during rheometric tests, the results are not representative of the initial sample properties. This phenomena can be controlled by using solvent traps [Magnin et al., 1990]. Moreover generation of secondary flows at high shear rates, in particular when having large angles θ_0, appear at high shear rates, possibly leading to sample ejection from the geometry [Sdougos et al., 1984]. Finally, the truncated gap is dependent of the angle θ_0, limiting the size of particles in suspensions to be analysed.

2.3.1.2 Flow between parallel plates

It is assumed that the flow happening between two circular parallel plates of radius R separated by a gap H, form a constant straight cylinder, as depicted in figure 2.5. The flow is then analysed in cylindrical coordinates (O, r, θ, z).

In this configuration, the flow profile is represented by fluid layers parallel to the rotating plate and rotating around its axis.

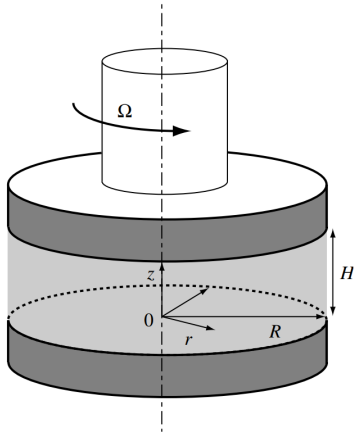

Figure 2.5: Parallel plates viscometric flow geometry. Scheme taken from [Coussot, 2005].

The shear rate within this geometry is calculated with the following expression:

$$\dot{\gamma}(r) = \Omega \cdot \frac{r}{H} \tag{2.7}$$

And the shear stress at distance R is given by the following expression:

$$\tau = \frac{\Gamma}{2\pi R^3}\left[3 + \frac{d\ ln\ \Gamma}{d\ ln\ \dot{\gamma}_R}\right] \tag{2.8}$$

Some of the features of this geometry is that the gap H separating both plates can be modified accordingly to sample properties. For instance, when studying suspensions, the gap between plates should be at least 50 times the size of the larger particles, to maintain the condition of continuous medium [Macosko, 1994] and avoiding frictional effects on viscosity measurements.

Equivalently, by modifying the gap, the shear rate range can be adjusted, as observed in equation 2.7. Therefore, lower shear rates are obtained by increasing the gap and contrarily, high shear rates are obtained by decreasing the gap. In addition, a small volume of sample is required to perform the experiment, typically under 2 ml.

However, parallel plates do not generate an uniform shear rate as the shear rate is maximum at the edge R but is minimum close to the origin $r = 0$, as observed in equation 2.7. The shear rate at calculated at the radius R is thus $\dot{\gamma}_R = \Omega \cdot \frac{R}{H}$. This can be corrected with a derivative by relating shear stress to total torque Γ with the expression given in equation 2.8. If the tested fluid is Newtonian, the expression is simplified to $\tau = \frac{2\Gamma}{\pi R^3}$. In addition, parallel plates can be subjected to evaporation and ejection, as discussed for cone and plate geometry.

2.3.1.3 Flow between concentric cylinders

In this geometry, the flow generated by the rotation of the inner cylinder can be represented by relative motion of concentric cylindrical layer of material rotating around the central axis. The flow is confined in the gap between the outer cylinder with a radius r_2 and the inner cylinder with a radius r_1 and a height h. Hence, the flow can be analysed in cylindrical coordinates (O, r, θ, z). This type of flow is also known as Couette flow and the geometry can be observed in figure 2.6.

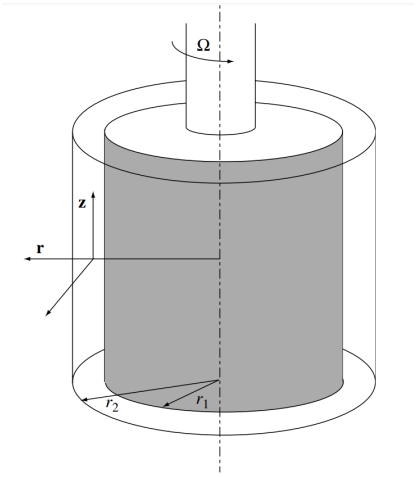

Figure 2.6: Concentric cylinders viscometric flow geometry. Scheme taken from [Coussot, 2005].

With this geometry the shear rate is dependent of the annular gap $\kappa = r_1/r_2$. The following expressions can be written for this geometry:

$$\dot{\gamma}_{r_2} \approx \dot{\gamma}_{r_1} = \frac{2\Omega}{1-\kappa^2} \quad for \;\; \kappa > 0.99 \tag{2.9}$$

$$\begin{aligned} \dot{\gamma}_{r_1} &= \frac{2\Omega}{n(1-\kappa^{2/n})} \quad for \;\; 0.5 < \kappa < 0.99 \\ and \;\; \dot{\gamma}_{r_2} &= \frac{-2\Omega}{n(1-\kappa^{-2/n})} \quad where \;\; n = \frac{dln\Gamma}{dln\Omega} \end{aligned} \tag{2.10}$$

and the shear stress is determined at the inner cylinder:

$$\tau = \frac{\Gamma}{2\pi h r_1^2} \tag{2.11}$$

This geometry is well adapted for samples having a low viscosity. As the sample is confined

in a cylinder container, the risk of sample ejection is very low even at high shear rates and boundary effects are reduced. Furthermore, evaporation is reduced as free surface area is reduced.

However, the shear rate is not homogeneous when having a large annular gap. In addition, it is possible to have end bottom effects described by the shearing of the lower part of the inner cylinder with the bottom of the outer cylinder. To reduce end effects, the bottom of the cylinder can adopt a different geometry with the goal of reduce secondary flows [Macosko, 1994].

2.3.2 Flow instabilities in rotational geometries

During experiments, some artefacts or instabilities can arise producing measurements not representative of a steady flow. This implies that the ideal assumptions mentioned in section 2.3 are no longer applicable and measurements obtained are not exploitable. Some of the instabilities occurring in these geometries are wall slip, fracture, shear banding, among others, and representative of the phenomena observed in suspensions [Bertola et al., 2003; Divoux et al., 2016].

2.3.2.1 Wall slip and fracture

The lack of samples adherence to smooth geometries is often a problem during shearing experiments. This phenomena is known as wall slip and it occurs when a thin lubricating "slipping layer" appears between the shearing walls and the sheared material [Yoshimura et al., 1988]. For instance, when imposing a given shear stress τ, if the sample slips the rheometer measures an apparent shear rate $\dot{\gamma}_{app}$ that is abnormally higher to the real effective shear rate $\dot{\gamma}_{eff}$. As a result, significant lower shear stresses are obtained for a given deformation. Nevertheless, several methods exist to correct experimental data obtained with slip, among the most important the method proposed by Mooney [Mooney, 1931] an the one of Yoshimura and Prud'homme for yield stress fluids [Yoshimura et al., 1988].

Wall slip can be suppressed by using geometries with textured surfaces [Magnin et al., 1990]. The roughness of the geometry should be adequate to provide grip and to avoid secondary flows [Magnin et al., 1987]. Moreover, Aral and Kalyion [Aral et al., 1994] studied the wall slip as function of roughness and it was found that the slip decreased as the roughness of the surface increased.

However, when suppressing wall slip in concentrated suspensions other phenomena can rise, as fracture [Aral et al., 1994]. This phenomenon can be observed in yield stress materials like

slurry and pasty materials. The fracture can be observed in the core of the sheared sample by following the distortion of a vertical line [Magnin et al., 1987], as displayed in figure 2.7.

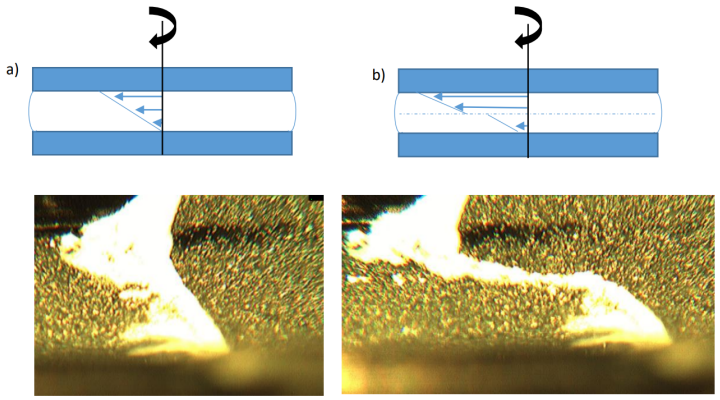

Figure 2.7: Fracture occurring in the free surface of a zinc slurry in a parallel plates geometry with roughened surfaces. Sample is sheared at $\dot{\gamma} = 0.01\ s^{-1}$. a) $t = 120\ s$, b) $t = 260\ s$. Gap H between plates is 1 mm.

When fracture happens it is observed that the velocity gradient is not constant, as observed in the inset b) in figure 2.7, obtaining just a local apparent shear rate $\dot{\gamma}_{app}$. This effect becomes worse with shearing time and limits the deformation of the sample in question.

2.3.2.2 Shear banding

Contrary to the hypothetical homogeneous shear rate in a geometry (section 2.3), shear bands can be defined as the progressive evolution of the shear rate towards two different values in two adjoining regions of the sheared fluid. The cause of this phenomena depends on the sample intrinsic properties but generally originates from the competition of different physical phenomena [Ovarlez et al., 2009].

For instance, the origin of shear bands in yield stress fluids consists in the coexistence of a sheared region (liquid-like) and unsheared region (solid-like) [Pignon et al., 1996]. When the fluid subjected to a shear rate $\dot{\gamma}$ lower than a critical shear rate $\dot{\gamma}_c$, the sample can split into a flowing region under a deformation higher than $\dot{\gamma}_c$ and another static region [Coussot et al., 2002]. Another example are suspensions, in which shear bands can originate from the competing sedimentation of particles in competition with a shear induced resuspension in a Couette device [Acrivos et al., 1993]. Conversely, if there is no sign of sedimentation [Ovarlez et al., 2006], the shear banding can arise from the competition between hydrodynamic forces (liquid regime) and contact frictional forces (jammed-solid regime), as observed in non-Brownian suspensions.

To overcome shear banding, it is usual to erase the mechanical history of the sample with a large deformation and then to characterise sample properties in a time lower than a character-

istic time to develop a competing behaviour to shearing [Auffret et al., 2009a,b; Ovarlez et al., 2013].

When none of these geometries is convenient to the sample to be analysed, there is still another option to be considered, in which non-conventional geometries with different shapes are suitable for the such samples.

2.3.3 Non-conventional geometries

Non conventional shearing geometries can have different designs and some examples are vanes [Baravian et al., 2002], helical impellers [Brito-De La Fuente et al., 1997], fractal geometries [Owens et al., 2020], multi-blade mobile [Puig et al., 2016], among others.

Among the non-conventional geometries, the most widely used is the vane tool. Vane geometry has been used to study the yielding of fluids and steady state flow behaviour of structured (but nor only) non-Newtonian fluids [Barnes et al., 2001]. A scheme of the vane geometry is shown in figure 2.8.

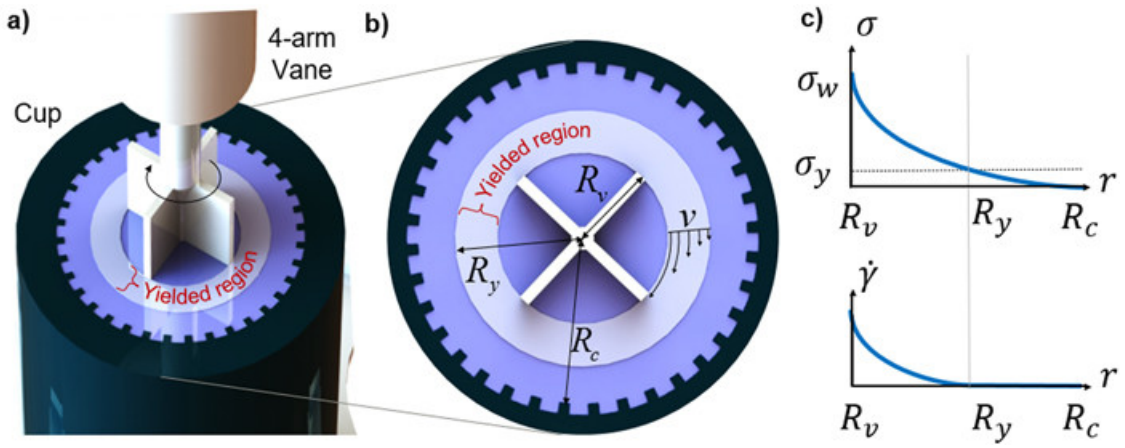

Figure 2.8: Vane-in-cup geometry with roughed surface [Owens et al., 2020].

The vane depicted in figure 2.8, consists in a 4 blade geometry. The vane usually have from 2 to 8 blades depending on the design. The yield stress can be determined from the maximum torque exerted on a given sample using a vane [Keentok, 1982]. In order to quantify the yield stress, it is assumed that the shear is homogeneously distributed at the end of the blades, forming a yielded cylinder region [Dzuy et al., 1985; Dzuy et al., 1983a] as observed in figure 2.8 a),b). Supposing that the vane blade has a heigh h and a width d, and it is submerged in a cup of diameter D, the yield stress can be calculated as follows:

$$\tau_y = \frac{\Gamma}{2\pi d^3}\left(\frac{h}{d}+\frac{2}{3}\right)^{-1} \tag{2.12}$$

Thus, yield stress can be calculated from vane dimensions (d and h) and maximum measured torque Γ. The maximum torque has to be obtained by imposing small rotational speeds so any viscous flow can be neglected. Moreover, the conditions the conditions h/d < 3.5; D/d>2 have to be respected. However, several authors confirmed that the sheared cylindrical region is actually larger than first thought and corrections need to be applied to have a real estimation of yield stress [Keentok, 1982].

Furthermore, it is possible to obtain flow curves using the vane tool. Several methods exist to convert raw rheometer data from the rheometer to shear stress and shear rate. For instance, associating the power consumption of a geometry to the rheological parameters of a well-known fluid [Brito-De La Fuente et al., 1997; Carreau et al., 1993]. The Couette analogy [Aït-kadi et al., 2002], has been widely used to translate raw data acquired with a non-conventional geometry and to convert it to rheological parameters, equivalently to equation 2.4. The procedure to calculate the geometrical constants K_τ and $K_{\dot{\gamma}}$ in order to obtain shear stress vs shear rate curves will be explained in Chapter 3, as indeed a vane geometry is used in our work. The procedure consists in associate the geometrical properties to the rheological behaviour of a well known fluid as it was a Couette geometry.

The main advantage of a vane geometry is that when introduced gently into the cup, the sample structure is almost undisturbed, ideal for sensible or structured samples and to prevent wall slip [Dzuy et al., 1983b]. In the scope of our study, non-conventional geometries are used to handle fluids with large heterogeneities and phase separation while providing continous mixing [Aït-kadi et al., 2002]. Moreover, with more access to 3-D printing nowadays, vanes are easy and cheap to fabricate, and even more, chemical stability can be ensured with proper material selection [Barnes et al., 2001; Owens et al., 2020].

Particle suspensions and slurries, are often heterogeneous and samples are not suitable to be analysed in conventional geometries[Hermoso et al., 2012; Hreiz et al., 2017; Lebranchu et al., 2017; Nzihou et al., 2004; Puig et al., 2016, among others]. In order to have a better insight on suspensions rheology, the evolution of the theory behind suspension is briefly reviewed in the following section. This include the first observations made by Einstein in the very early 20th century [Einstein, 1906], to studies unifying suspension rheology one century later [Boyer et al., 2011].

2.4 Rheology of suspensions

The field of suspensions is a vast domain with applications in numerous fields. Numerous examples can be given corresponding to different domains, like red blood cells suspended in plasma, colloidal starch suspensions in food systems, paintings, cement slurries, metallic suspensions for energy use, etc. Because the nature of the particles and the suspending fluids is vast, it has been difficult to find a common law unifying the suspension rheology. Some of the most ground breaking studies are presented from the dilute regime in which hydrodynamic forces are predominant, to the concentrated regime, in which frictional forces become predominant.

2.4.1 Dilute regime

First studies were carried by A. Einstein, considered a non-Brownian system, consisting in dilute non-interacting particles suspended in a Newtonian fluid [Einstein, 1911, 1906]. A non-Brownian system is a suspension in which there are no Brownian or colloidal motion/forces that can have important effects in small particles (particle size $< 1\ \mu m$)[Denn et al., 2014]. The following theoretical expression was obtained by Einstein:

$$\eta_s = 1 + 2.5\phi \tag{2.13}$$

Where η_s stand for relative suspension viscosity, being the ratio between the suspension and suspending fluid viscosity, and ϕ represents the particle volume fraction. The η_s is the viscosity ratio between the suspension and the suspending fluid viscosity.

However, the equation 2.13 given by Einstein is only valid in the very dilute regime in which $\phi \to 0$. The necessity of understanding more concentrated systems that were more in line with the processes observed in industry, raised the interest in further developing the suspension theory. However, main breakouts would be obtained several years after Einstein publications.

2.4.2 Semi-dilute to concentrated regime

An extended version of the equation 2.13 by Einstein was proposed by Batchelor and Green in 1972 [Batchelor et al., 1972a,b]. Their studies consisted in spherical non-Brownian particles suspended in a Newtonian fluid under a steady state velocity gradient. The particles under study are only subjected to hydrodynamic stresses in semi-dilute regime. Their breakthrough consisted in determining an hydrodynamic particle interaction of order ϕ^2, as represented in the following equation in shear flow:

$$\eta_s = 1 + 2.5\phi + 5.2\phi^2 \tag{2.14}$$

Another important model developed in the middle of 20th century is the Krieger-Dougherty model [Krieger et al., 1959]. In this model, the viscosity increase is a consequence of adding particles to a suspension already containing particles. A concentration ϕ_c is considered in this model, being the maximum packing fraction possible for a given packing arrangement and suspension composition. When $\phi \to \phi_c$, the viscosity approaches the infinity. The ϕ_c is empirically determined and can range from $0.5 < \phi_c < 0.74$ [Torquato et al., 2000].

$$\eta_s = \left(1 - \frac{\phi}{\phi_c}\right)^{-[\eta]\phi_c} \tag{2.15}$$

In equation 2.15, $[\eta]$ is the intrinsic viscosity, representative of the solute contribution to the suspension viscosity.

At the beginning of 21st century, studies on denser suspensions were done by different authors in the field of non-Brownian systems. Some of the studies considering Newtonian fluids as suspending fluids are the work of Zarraga et al. [Zarraga et al., 2000], in the dense regime ranging from $0.30 < \phi < 0.55$ and the work of Ovarlez et al. [Ovarlez et al., 2006], using magnetic resonance imaging to study monodisperse particles in the range of concentrations of $0.55 < \phi < 0.60$. A different approach with an inclined plane rheometry was presented by Bonnoit et al. [Bonnoit et al., 2010] in concentrations ranging $0.35 < \phi < 0.61$.

It is worth to highlight other works on concentrated suspensions by using a non-Newtonian suspending fluids. The work of Mahaut et al. [Mahaut et al., 2008] considered three yield stress fluids as suspending fluids. These were a water-in-oil emulsion, a Carbopol® and a bentonite suspension. The concentration of these suspension ranged from $0 < \phi < 0.50$. These results were modelled by Chateau et al. [Chateau et al., 2008], by proposing an estimation homogenization model in which at a macroscale the suspension behaves as a Herschel–Bulkley fluid with the same exponent as that of the suspending fluid. This isotropic approach was extended by Ovarlez et al. [Ovarlez et al., 2015], considering anisotropic spatial distribution of particles under shearing (shear-induced migration). Nonetheless, it is also important to highlight the work of Dagois-Bohy et al [Dagois-Bohy et al., 2015], in this study it was demonstrated that the dynamics of particles close to jamming are not dependent of the nature of the suspending fluid, but by particle geometrical constrains.

A common framework for suspensions was found by Boyer et al. [Boyer et al., 2011]. Suspensions can be described by a general law, considering hydrodynamical and frictional

effects as follows:

$$\eta_s(\phi) = 1 + \frac{5}{2}\phi\left(1 - \frac{\phi}{\phi_c}\right)^{-1} + \mu^c(\phi)\left(\frac{\phi}{\phi_c - \phi}\right)^2 \tag{2.16}$$

In the proposed model, the first two terms are accountable for the hydrodynamic contribution, tending to Einstein viscosity in very dilute suspensions. The third term is accountable for solid contacts and provides the viscosity divergence with the term $(\phi_c - \phi)^{-2}$, where viscosity diverges asymptotically to the maximum volume fraction observed at $\phi_c = 0.585$ [Boyer et al., 2011]. The frictional term $\mu^c(\phi)$ is a function of ϕ and frictional factors characteristic of the suspension components.

The evolution of the study of suspensions went from very dilute systems in early 1900s to dense suspensions as granular systems studied one century later. The review paper by E. Guazzelli and O. Pouliquen [Guazzelli et al., 2018] gathered several experimental data sets and models. These are available in figure 2.9.

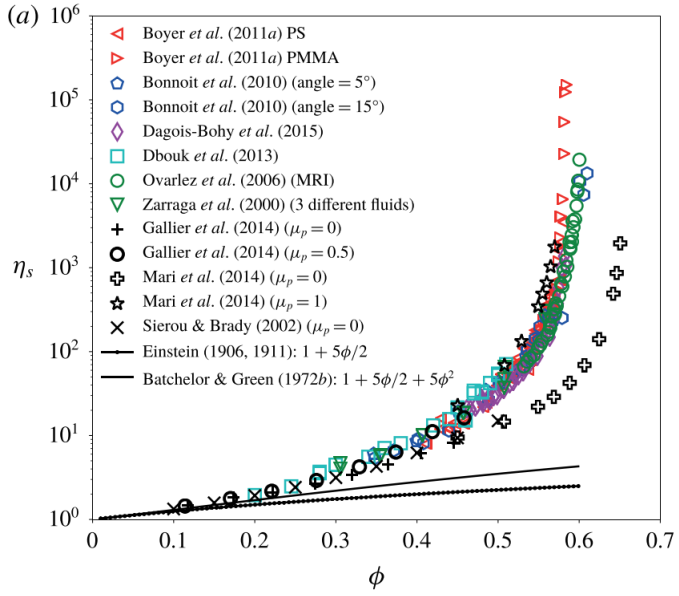

Figure 2.9: Relative suspension viscosity η_s as function of volume fraction ϕ. Several models and data sets are compared [see citations in Guazzelli et al., 2018].

It is interesting to see that most of the values for relative suspension viscosity diverges at the same maximum volume fraction $\phi_m \approx 0.585$, as predicted by Boyer [Boyer et al., 2011] in which $\eta \to \infty$. However, some deviations are observed from this common behaviour. As discussed at the beginning of this section, Einstein (equation 2.13) and Batchelor (equation 2.14) model predictions work only in very dilute and semi-dilute concentrations at concentration ϕ below 0.05 and 0.15, respectively. Another deviation is obtained from the study of Mari et al. [Mari et al., 2014]. A model was proposed taking into account frictional contact forces together with

viscous lubrication in a dense regime ($\phi > 0.45$). Very different results were obtained when considering frictionless particles ($\mu_p = 0$), as observed in figure 2.9. This latter highlights the importance of frictional contributions in suspension rheology.

The theory of the development of suspensions indicates that the viscosity of a suspension is highly dependent of the volume fraction ϕ, specifically in the concentrated regime at which viscosity increases towards infinity as $\phi \rightarrow 0.585$. This knowledge is highly important for suspension and slurry-based RFBs because there is a trade off between network conductivity and suspension viscosity. Moreover, when dealing with such dense particles like zinc ($\rho = 7.11\ g/cm^3$), viscosity of suspending fluid is likely to be increased to avoid the sedimentation of the particles. These design parameters will be assessed in the core chapters presenting the research work on the zinc slurry for RFB.

2.5 Rheometry approach to RFB

As explained in chapter one, RFBs use a pump to recirculate electrolyte solution from storage tank to the electrochemical reaction located in the cell, where the redox reactions will take place. Pure aqueous RFB use Newtonian fluids as electroactive materials and the viscosity is usually maintained as low as possible to reduce energy requirements during pumping.

Nevertheless, novel semi-solid flow cells were introduced in RFBs as a higher energy density alternative for stationary storage systems. When using energy-dense active materials suspended in an electrolyte, energy density increases proportional to their concentration [Duduta et al., 2011]. The semi-solid material consists in a slurry that can exhibit a complex flow behaviour when recirculated in the battery.

What if RFBs are analysed from a rheometrical point of view?

Rheometry can be used like a tool to maximize the performance of a RFB. In fact studies have shown that rheological behaviour, which is dependent of concentration ϕ of elementary electro-active components, has an impact on battery performance. With the tools presented in chapter two, it is possible to have an insight on the viscous behaviour of electro-active fluids.

For instance, studies have shown that the rheological percolation occurs close to the electronic percolation [Parant et al., 2017], evidenced by a sharp increase in viscosity and conductivity, respectively. This phenomenon is then controlled by particle concentration ϕ [Lohaus et al., 2019], which is directly related to suspension viscosity.

With increasing ϕ, structured fluids can be formed showing a yield stress behaviour. This

behaviour is beneficial for RFBs as a percolated network exhibit higher conductivities [Fan et al., 2014; Wei et al., 2015], beneficial to the performance of RFBs. Nevertheless, an optimal yield stress exists, as the energetic cost of pumping such suspensions can increase drastically with increasing viscosity [Iyer et al., 2017; Smith et al., 2014]. To reduce mechanical energy dissipation, the promotion of wall-slip by surface modification can ease the pumping of such materials, leading to significant power savings while maintaining a good electrochemical performance [Solomon et al., 2018]. With this knowledge, efforts can be made in order to maximize the energetic efficiency by aiming specific rheological behaviour, as shown in the work of Smith et al. with yield stress fluids [Smith et al., 2014].

So can rheometry be used to optimize RFB performance?

The answer to this question lays in the upcoming chapters containing the core of the research. In this work, rheometry is extensively used to formulate and characterise suspending fluids and slurries to be used in a RFB. It is highlighted that harsh alkaline environment inherent of the zinc-air chemistry is a challenge to formulate stable zinc suspension. In like manner, interactions happening between components in microscale are studied from the macroscopic rheological behaviour of our samples.

Throughout these chapters, samples will be characterised by rheometry and their impact on the zinc slurry - air RFB is extensively discussed.

2.6 Conclusion

The main concepts to analyse and understand the rheology of suspension were introduced in this chapter. It was discussed that structured fluids show non-Newtonian behaviour due to microscopical arrangements that can be modified with shearing. Suspensions, slurries, pastes, granular materials form part of this fluids displaying a yield stress behaviour. Moreover, as discussed in section 2.4.2 the interactions of the microstructures increase when concentration ϕ increases, as viscosity frictional contributions exceeds the hydrodynamic contributions.

For our study, dense zinc particles ($\rho = 7.11\ g/cm^3$) have to be suspended in electrolyte media for application in a zinc slurry - air RFB. The electrolyte used is a highly concentrated KOH solution with a pH $\gtrsim 14$. In order to formulate a stable suspension, meaning that particles will not settle over time, a special type of suspending fluid is needed to counterbalance the net gravity force and harsh alkaline environment. It is then indisputable that a rheological approach is needed to be able to characterise suspending fluid flow behaviour for formulation and complete slurry sample for the performance in a RFB.

CHAPTER

THREE

GEL POLYMER ELECTROLYTES RHEOLOGICAL BEHAVIOUR: YIELD STRESS AND VISCOELASTICITY

In redox flow batteries (RFBs), semi solid flow cells incorporate solid particles in the same medium than the electrolyte in the form of slurry to increase energy efficiency. However, rheological properties of the fluid hosting the solid particles need to favour the particle stability and the pumping process within the RFB. In this study, the the materials used to formulate a gelled polymer electrolyte (GPE) that will be used as suspending fluid in a zinc slurry - air RFB are studied. It was found that when using polyacrylic acid and attapulgite gelling agents together, a yield stress behaviour is found. This satisfactory result was obtained even in harsh alkaline conditions (pH > 14), representative of the battery operation conditions in which the chemical stability of gelling agents is threatened. Yield stress values were obtained by fitting experimental data to the Herschel-Bulkley model and results were compared to creeps. Results indicate that the GPEs presented in this study are good candidates to host zinc particles for a zinc slurry - air RFB.

Contents

3.1 Introduction

Since late 20th century, Li-ion batteries have dominated the energy storage market [Li et al., 2018], but market-dependent cost [Ciez et al., 2016], limited geological availability [Gruber et al., 2011; Vikström et al., 2013], fire-related hazards [Kong et al., 2018] and recyclability [Garole et al., 2020] have taken academia and industry to search for more sustainable solutions for the future. Recently, redox flow batteries (RFBs) have gained attention because of its flexible design, outstanding from others electrochemical energy storage systems.

Redox flow batteries (RFBs) are energy storage systems that aim to shorten the gap between intermittent renewable energy sources like wind and solar, and the energy grid [Rugolo et al., 2012]. RFBs differ from regular batteries because electrolytes are stored externally in reservoirs and pumped throughout the reactor, where power generation occurs. RFB storage capacity will depend on the size of the electrolyte tanks, whereas power output will depend on the number of cells in the battery stack. In the electrolyte tanks, energy is stored in electro-active materials dissolved or dispersed in aqueous electrolytes. The ability of redox-active materials to be oxidized and reduced indefinitely gives the battery the capability of being rechargeable. This flexible design allows independent storage/power optimization and easy scalability for specific applications.

Recently, metal-air batteries have been designed as RFBs. Advantageous high energy density, inherent of metals [Han et al., 2018; Kim et al., 2013], combined with the flexible design of RFBs, able to decouple energy and power, have been investigated under this synergistic approach. Amongst them, zinc – air RFB have gained special attention due to zinc availability on earth and its high specific energy density (1350 Wh/kg [Bockelmann et al., 2016]).

Nonetheless, metallic zinc anode suffers from different stability problems during charging such as localized dendrite formation [Banik et al., 2015; Liu et al., 2016; Yang et al., 2016], electrode shape change [Mainar et al., 2018b] and formation of passivation layers [Han et al., 2018; Yang et al., 2004]. Consequently, new approaches are being evaluated to enhance battery lifespan, among them, the development of a semi-solid zinc anode consisting in zinc particles dispersed in alkaline electrolyte forming a slurry.

While using a slurry approach, zinc works as a flowable anode (semi-solid electrode) which is stored in a tank externally to the reactor. Thus, zinc slurry serves the double purpose of electrode and electrolyte, reaching higher energy densities due to utilisation of active material in comparison with its equivalent pure aqueous electrolyte configuration [Duduta et al., 2011]. When battery is under operation, slurry is pumped to the reactor where charge/discharge reactions take place.

Zinc slurry flow behaviour is of great importance to the whole system, not only when the battery is operating but also at rest. In particular, a sufficient high viscosity is needed to maintain zinc particles in suspension when the battery is at rest. However, slurry viscosity needs to be sufficiently low to be able to be pumped throughout the battery without affecting the energetic efficiency of the RFB [Barton et al., 2018; Iyer et al., 2017]. Hence, an optimal formulation has to be found, where viscosity will be high enough to maintain particles in suspension, but low enough to ease pumping.

However, zinc slurry formulation and characterisation are not trivial tasks. Zinc – air batteries work under harsh alkaline conditions. Usually potassium hydroxide (KOH) in concentrations ranging from 6 – 10 M are used as aqueous electrolyte to have high ionic conductivity favouring the transport of specific zinc ionic species [Mainar et al., 2018c,d]. Under these conditions pH increases significantly (pH $>$ 14), and gelling agents able to suspend dense zinc particles (density = 7.11 g/cm^3), are scarce. Given these conditions, new formulations for gelling agents with the role of suspending zinc particles are needed for RFB application.

In this study, the rheology of the suspending fluids for anode zinc slurries is thoroughly analysed. Gelled polymer electrolytes (GPEs) are proposed as suspending fluids for zinc particles to be used in a zinc slurry - air RFB.

GPEs considered inhere consist in a gelled KOH electrolyte. KOH has been used previously

in zinc slurry - air application [Choi et al., 2020a,b], because of its superior conductivity to other alkaline electrolytes. In order to form a gelled electrolyte two different gelling agents are used: polyacrylic acid (PAA) and attapulgite.

PAA forms a physical gel with enhanced viscosity at neutral pH [Piau, 2007]. Although previous studies have shown that viscosity of PAA decreases significantly at pH higher than 10 [Charman et al., 1991; Gutowski et al., 2012; Lochhead et al., 1989], it has been shown that PAA is able to remain chemically stable under highly alkaline KOH concentrations [Tran et al., 2019].

To strengthen network gel properties, attapulgite clay is used in the formulation. Attapulgite is a type of magnesium aluminium silicate clay with chemical formula $3MgO - 1.5Al_2O_3 - 8SiO_2 - 9H_2O$. This clay forms a gel when dispersed at high shear rates. Attapulgite has been previously used to formulate zinc anode slurries. In addition it was found that when used as additive together with zinc oxide (ZnO) in the formulation, battery life is improved as less corrosion rates are reported [Sonneveld, 1991].

Furthermore, a yield stress fluid behaviour is sought with the formulation presented in this work. Yield stress fluids are materials that displays a dual flow behaviour: at stresses below yield stress (τ_y), materials will show solid-elastic behaviour and at stresses above yield stress, material will start to flow and behave as a viscous liquid following a shear-thinning behaviour. Different models have been proposed to analyse yield stress fluids. The Herschel-Bulkley model has been proved to describe properly the rheology of suspensions using 3 parameters [Frigaard, 2019; Ovarlez et al., 2015]. This model is expressed in equation 3.1:

$$\tau = \tau_y + K\dot{\gamma}^n \tag{3.1}$$

Where τ is the shear stress, $\dot{\gamma}$ is the shear rate and the 3 parameters correspond to: τ_y yield stress, K consistency index, and n flow index.

Furthermore, the definition of a unique yield stress value has been a topic of discussion [Barnes, 1999], and the root of this problem may come from a steady-state definition or experimental issues (i.e. slippage, ejection, fracture, etc.)[Balmforth et al., 2014], shear banding [Rouyer et al., 2005] and time dependent behaviours (i.e. thixotropy, structuration) [Caton et al., 2008; Dinkgreve et al., 2016; Møller et al., 2006]. To tackle the problems mentioned above, a tailored protocol is put in place to determine yield stress and GPE flow behaviour.

This study aims to characterise elasto-visco-plastic behaviour of GPEs containing high concentration of electrolytes designed for energy storage. Yield stress flow behaviour is sought for RFB application at pH $>$ 14, conditions in which gelling agents as PAA behave poorly as

suspending fluids. Notably, the effect of PAA concentration in GPEs is studied to evaluate gelled network properties as candidates to be used in a RFB. Samples are studied using small and large deformation rheological tests. Oscillatory rheology is used to study viscoelastic sample properties in the linear regime representative of the material at rest. Steady state flow curves are obtained for each of the samples analysed using large deformation techniques from which yield stresses were determined using Herschel-Bulkley model (equation 3.1). Moreover, GPEs yielding was studied performing creep tests, allowing to study and compare liquid-solid transition. With the objective to determine if sample exhibited time-dependent properties, GPEs viscoelastic properties were linked and analyzed using rheometer rotor inertia [Auffret et al., 2009a; Baravian et al., 1998; Benmouffok-Benbelkacem et al., 2010] during creeps. This set of tests provided detailed rheological properties of solid and liquid regimes of GPEs.

3.2 Material and methods

3.2.1 Sample preparation

GPEs are prepared as follows. Aqueous electrolyte solution is prepared by dissolving potassium hydroxide (KOH) flakes (Reagent grade, 90%, Sigma-Aldrich) in deionized water. The resulting pH of this solution was found to be 14.7 obtained with a pH meter (Orion Star A215, Thermo Fisher Scientific), using a pH/ATC rechargeable electrode (Orion™ ROSS Ultra™ Triode™). Next PAA gelling agent (Carbopol® 940, Acros Organics) is dissolved in aqueous electrolyte solution with the aid of a magnetic stirrer for 24 h to ensure full polymer dissolution. Then, attapulgite gelling agent (Attagel® 50, BASF), is added to the mixture together with zinc oxide (99.9 % metal basis, -200 mesh powder, Alfa Aesar), under continuous stirring for 5 minutes. Finally, mixture is homogenized for 1 minute using a high shear homogenizer (Ultra-Turrax, T25 model, IKA) to obtain the GPE. Samples are mixed at the lowest speed (11 000 rpm for 1 minute) to avoid mechanical degradation on PAA chains and to disperse and build attapulgite gel.

Concentrations of each component are available in table 3.1. It is remarked that this study focuses on the effect of PAA gelling agent on GPEs rheological behaviour. These concentrations were carefully chosen and tested in the set-up presented in one of our studies on a zinc slurry-air RFB [Choi et al., 2020a and upcoming Milian et al. 2021]. Alkaline environment for the operation of the battery together with ionic conductivity is obtained with KOH electrolyte at a concentration of 92 % wt. PAA and attapulgite concentrations were chosen to prepare gel-like materials. Finally, ZnO was added to prevent zinc self-discharge. Satisfactory discharge results were obtained by N. Choi et al. [Choi et al., 2020a], using a similar formulation with same

electrolyte KOH concentration.

Sample	KOH 10 M wt. %	PAA wt. %	Attapulgite wt. %	ZnO wt. %
GPE1	92.00	0.30	1.40	6.00
GPE2		0.45		
GPE3		0.60		
GPE4		0.75		
GPE5		0.90		

Table 3.1: Gel polymer electrolytes composition.

3.2.2 Rheometry

GPEs rheological behaviour was investigated using a stress-controlled rheometer AR-G2 (TA instruments, United States) equipped with a specially designed 4-blade vane-in-cup geometry (h = 45.5 mm, d = 30 mm), as depicted in figure 3.1. Vane-in-cup tool is used to avoid slippage [Barnes et al., 2001], and ensure sample homogeneity [Aït-kadi et al., 2002]. A transparent cup (D = 48 mm) is used to observe the appearance of sheared sample with the aid of microscope usb camera (A1 2MP 500 X, Andonstar, China). The wall of the cup is equipped with a squared grid ($L_{square} = 5.5mm,\ thickness = 2mm$) to suppress slippage between the sample and cup wall [Owens et al., 2020].

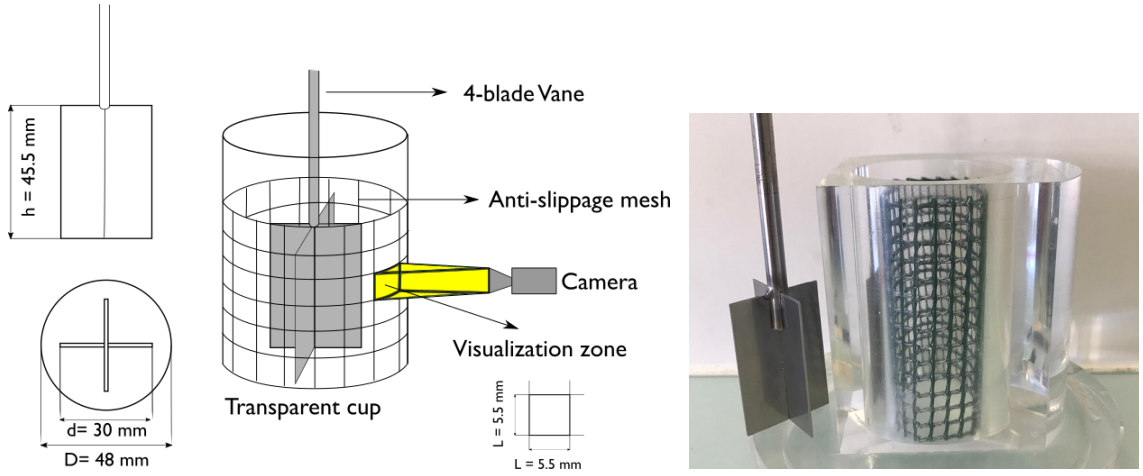

(a) (b)

Figure 3.1: Vane-in-cup shearing geometry. Transparent cup allows to observe sample appearance trough the spaces of the squared grid ($L_{square} = 5.5mm$ and thickness 2 mm). a) Scheme of Vane-in-cup and set up used for GPEs rheometrical characterisation. b) Picture of actual set-up.

The vane generates a flow profile in a Couette that is similar to the one occurring in concentric cylinders geometry [Baravian et al., 2002]. Furthermore, it is possible to convert rotational speed and torque obtained with the vane-in-cup, into shear rate and shear stress, respectively,

using a Couette analogy approach [Aït-kadi et al., 2002]. Figure 3.2 is a representation of the Couette analogy applied for the vane-in-cup used in this study.

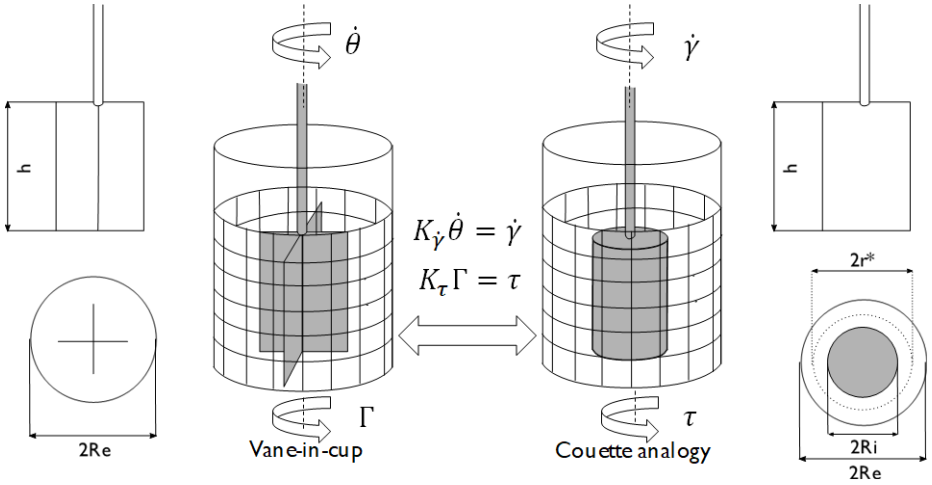

Figure 3.2: Vane geometry and its virtual analogous cylinder.

In the scheme in figure 3.2, $K_{\dot{\gamma}}$ and K_{τ} are geometrical factors that need to be experimentally determined. Once factors are obtained, they can be applied as if the geometry used is an analogous inner cylinder and so shear rate and shear stress can be calculated as follows [Aït-kadi et al., 2002; Hermoso et al., 2012; Puig et al., 2016]:

$$\begin{aligned} \dot{\gamma} &= K_{\dot{\gamma}}\dot{\theta} \\ \tau &= K_{\tau}\Gamma \end{aligned} \tag{3.2}$$

Where $\dot{\theta}$ is the rotational velocity, Γ is the measured torque and $K_{\dot{\gamma}}$ and K_{τ} are the geometrical correction factors.

Geometrical factors were determined using the Couette analogy introduced by Aït-Kadi et al. [Aït-kadi et al., 2002]. This protocol determines analogous inner cylinder dimensions, represented in figure 3.2, corresponding to the flow profile generated by the Vane. $K_{\dot{\gamma}}$ and K_{τ} were determined as follows:

$$K_{\dot{\gamma}} = \frac{2}{n} \frac{\left(\frac{R_e}{r^*}\right)^{\frac{2}{n}}}{\left(\frac{R_e}{R_i}\right)^{\frac{2}{n}} - 1} \tag{3.3}$$

$$K_{\tau} = \frac{1}{2\pi r^{*2} h}$$

Where R_e and R_i are the cup and the analogous inner cylinder radius, respectively, h is the height of the vane, corresponding to the height of the analogous inner cylinder; n is the flow index of the fluid used for the calibration and r^* is an optimal radial position calculated from cup and vane dimensions. At this position r^*, any sample can be characterised independently of its flow index n.

A shearing experiment with a standard Newtonian fluid (ISO 17025, 6166 mPa s, 20 $°C$, Paragon Scientific Ltd), is done to perform the calibration. This fluid was selected to perform the calibration as its viscosity is in the same order of magnitude that the samples analysed in this study in its fluidized state (above yield stress).

Complete calculation of analogous inner cylinder radius R_i and optimal radial position r^* can be found in supporting information 1. With these conditions, $K_{\dot{\gamma}} = 2.30\ rad^{-1}$ and $K_{\tau} = 13450.7\ Pa\,N^{-1}\,m^{-1}$ were obtained. Calibration was successfully validated by measuring viscosity of a non-Newtonian fluid (Carboxymethyl cellulose 3 wt. %). Results obtained with a vane tool were compared to the ones obtained with a cone (1 deg, r = 30 mm) and plate geometry (supporting information figure 3.13).

3.2.2.1 GPEs Oscillatory rheology

GPEs viscoelastic properties at small deformations are studied by oscillatory rheometry by applying sinusoidal deformations. Linear domain is obtained by performing a strain amplitude sweep tests, from 0.1 to 1000 % at 1 Hz.

After determining linear domain, samples viscoelastic behaviour close to rest was studied. This was done by performing a frequency sweep from 0.01 to 4 Hz at a constant deformation $\gamma = 0.1$ %, located in sample linear domain.

3.2.2.2 GPEs flow curves

GPEs flow curves were obtained by large deformation tests. For such complex materials a specific protocol had to be implemented in order to obtain results representative of the material and independent of sample previous handling or shear history before its characterisation. To do so, the protocol was first tested and optimised with GPE5 sample. GPE5 was then subjected to successive shear rate steps. Shear rates are applied from 0.001 to 100 s^{-1} and down to 0.001 s^{-1}, each step with a duration of 120 s (5 measured points per decade). This shear rate increase and decrease was repeated twice, as represented in figure 3.3(a). This was done in order to understand if the solid-liquid transition is comparable to the liquid-solid transition, and the reproducibility of the measurement when comparing the ramps.

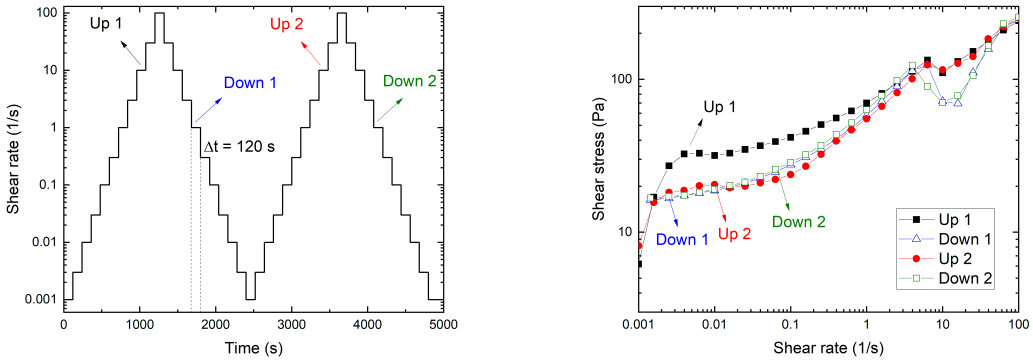

(a) (b)

Figure 3.3: a) Flow sweep protocol. Sample undergoes consecutively increasing and decreasing shear rate steps from 0.001 to 100 s^{-1} and down to 0.001 s^{-1}. Each step had a duration of 120 s, 5 points per decade were obtained with a total of 25 steps. b) GPE5 shear stress as function of shear rate. Numbers correspond to the order in which flow sweeps were performed.

Shear stress response to applied shear rate is represented in figure 3.3(b). During the first increasing steps (curve Up 1), it is observed that shear stress increases continuously in a shear-thinning behaviour.

As the first decreasing steps starts (Down 1), shear stress recorded is lower than the value obtained for the first increasing ramp. As shear rate decreases to the lowest values, a clear shear stress plateau is observed, indicating yield stress behaviour. The subsequent Up 2 and Down 2 ramp are superimposed on the first Down 1, showing excellent reproducibility once the material mechanical history has been erased by the first increasing ramp.

However, at shear rates higher than 3 s^{-1}, stress suddenly undershoots independently of the ramp. This sudden decrease in shear stress is a consequence of the Weissenberg effect [Eitelberg, 1984; Weissenberg, 1947] and more information can be found in supporting information 2,

together with a video [https://rb.gy/pypcww].

At shear rates lower than 3 s^{-1}, Weissenberg effect is not observed and results are reproducible in this region. The flow behaviour is the one of a yield stress fluid followed by shear thinning behaviour.

Furthermore, pictures of the sample in the transparent cup were taken during shearing through the spaces of the grid (figure 3.1(a)), and they can be observed in the insets of supporting information, figure 3.15. It is observed that when shear rate is up-ramped for the first time (Up 1), sample appearance changes from a plain surface aspect (at $\dot{\gamma} = 0.01\ s^{-1}$) to small aggregates across all the sample at $\dot{\gamma} \gtrsim 0.01\ s^{-1}$. Contrarily, when shear rate is down-ramped (Down 1), changes in sample appearance are not observed. In fact, when aggregates are seen across all the sample, the appearance of the sample will not further change. To summarize information above, when sample undergo the first solid-liquid transition (Up 1), the appearance of the sample changes and adopt a new flow behaviour, with a lower yield stress. Once the sample adopt the new appearance, flow behaviour remains the same (curves Down 1 and Down 2), as sample aspect does not further evolve. A small deviation is observed for Up 2, indicating that indeed decreasing ramps must be used for this sample to obtain reproducible results at shear rates $\leq 3\ s^{-1}$ (supporting information figure 3.16).

Thus steady state flow curves for all samples GPE1 - GPE5 were obtained only by down-ramping shear rate steps, unless stated for a specific result. Each decreasing step had a duration of $\Delta t = 1000$ s, sufficient to attain steady state as shown in figure 3.17, unless otherwise indicated.

To quantify rheological parameters of GPEs, shear stress as function of shear rate experimental data is fitted to a Herschel-Bulkley model (equation 3.1), from which yield stress τ_y, consistency index K and flow index n are obtained describing sample flow behaviour.

3.2.2.3 Creeps

Samples elasto-visco-plastic behaviour was studied using creep tests. Focus was placed on solid-liquid and liquid-solid transition to determine sample yield stress. Morevoer, this yielding study allowed comparison to yield stress obtained from fitting experimental flow curves data to Herschel-Bulkley model (equation 3.1).

Several studies [Cheng, 1986; N'gouamba et al., 2020; Ovarlez et al., 2013], have found two type of yield stresses being the **static** yield stress and the **dynamic** yield stress. Tests to determine yield stress assess whether the sample in evaluation has developed a steady state flow (**static** yield stress) or has ceased flowing (**dynamic** yield stress). Experimental efforts

have shown that static yield stress is higher than dynamic yield stress, for the same material analysed [Cheng, 1986]. Therefore, the protocol presented in this section will allows us to determine how different is the yield stress depending on the direction in which the solid-liquid transition is studied.

To set up the creep protocol, preliminary τ_y values were used as reference for each GPE in the following way. Shear stresses were increased from $\tau_{initial}$ (below yield stress) to τ_{final} (above yield stress), and then decreasing back to $\tau_{initial}$, as shown in figure 3.4(a). Equivalently, values of $\tau_{initial}$ and τ_{final} were carefully selected from flow curves for each GPE, so the solid-liquid transition could be observed. Finally, to ensure steady state each creep step had a duration of $\Delta t = 1000$ s. Figure 3.4(b) shows the expected strain response as function of time of the viscoelastic material when a stress is applied to it.

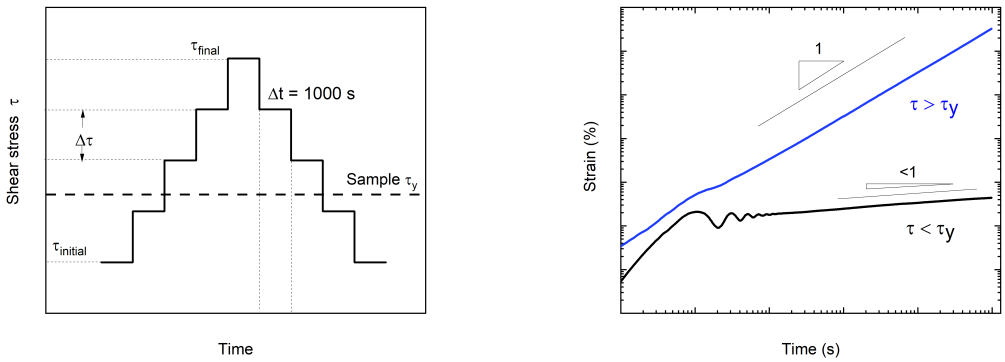

(a) (b)

Figure 3.4: Creep protocol for GPEs. a) Successive creeps procedure to determine yielding. Each creep step had a duration of 1000 s. b) Example of expected response to creep procedure.

It is observed in figure 3.4(b) that two behaviours can be expected depending if the stress τ is smaller or larger than sample τ_y. When $\tau < \tau_y$, strain evolves as a weak power law over time, characteristic of solid-like state. Contrarily, when $\tau > \tau_y$ strain increases rapidly as function of time with a slope of 1, indicating that the sample is flowing.

Furthermore, figure 3.4(b) also shows strain oscillations during creep experiments. These oscillations have an elastic origin and are helpful to study the influence of time and shear history on viscoelastic properties of GPEs. This is explained in detail in next section.

3.2.2.4 Inertio-elastic oscillations

In this section, a method is presented in which sample viscoelastic properties are obtained from creep oscillations. As observed in figure 3.5, when performing creep experiments, defor-

mation oscillates at the beginning of each creep step. This response is known as inertio-elastic oscillations [Baravian et al., 1998; Yao et al., 2008].

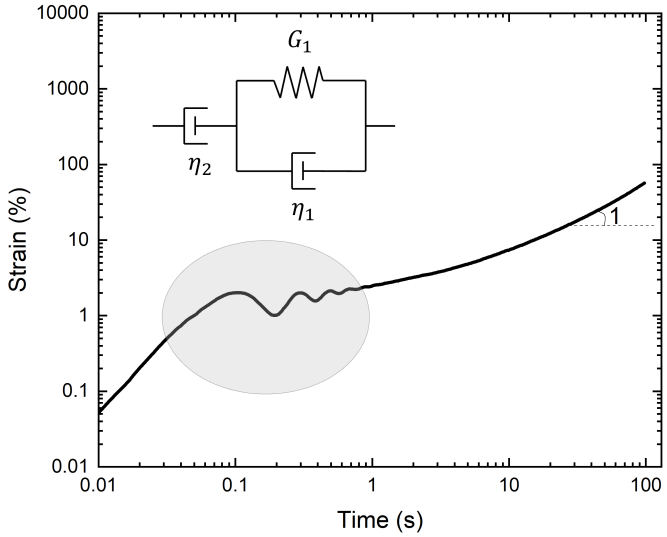

Figure 3.5: Creep test highlighting inertio-elastic oscillations. Inset is a representation of the Jeffrey model representing sample viscoelastic properties.

In figure 3.5, oscillations are seen as a result of the inertial response of the moving part of the rheometer and the viscoelastic sample. A Jeffrey model (inset figure 3.5) is proposed to analyse these oscillations and link them to sample viscoelasticity. The model consists in a dash-pot element in series with another element composed by a dash-pot connected in parallel to a spring. The dash-pot represents the steady state viscous liquid behaviour of the sample η_2, whereas the elements in parallel represents the elasticity G and elastic dissipation η_1.

The constitutive equation of Jeffrey model is [Baravian et al., 1998]:

$$(\eta_1 + \eta_2)\dot{\tau} + G\tau = \eta_2 G\dot{\gamma} + \eta_1\eta_2\ddot{\gamma} \tag{3.4}$$

The analytical solution of this equation if found in the paper of Benmouffok-Benbelkacem et al. [Benmouffok-Benbelkacem et al., 2010], in which strain γ is described by a function involving the inertia of the rotating geometry and the viscoelastic sample information that will be obtained by the model being η_1, η_2, and G.

3.3 Results

3.3.1 Oscillatory rheology

Viscoelastic GPEs properties were studied by means of oscillatory rheometry and results are depicted in figure 3.6.

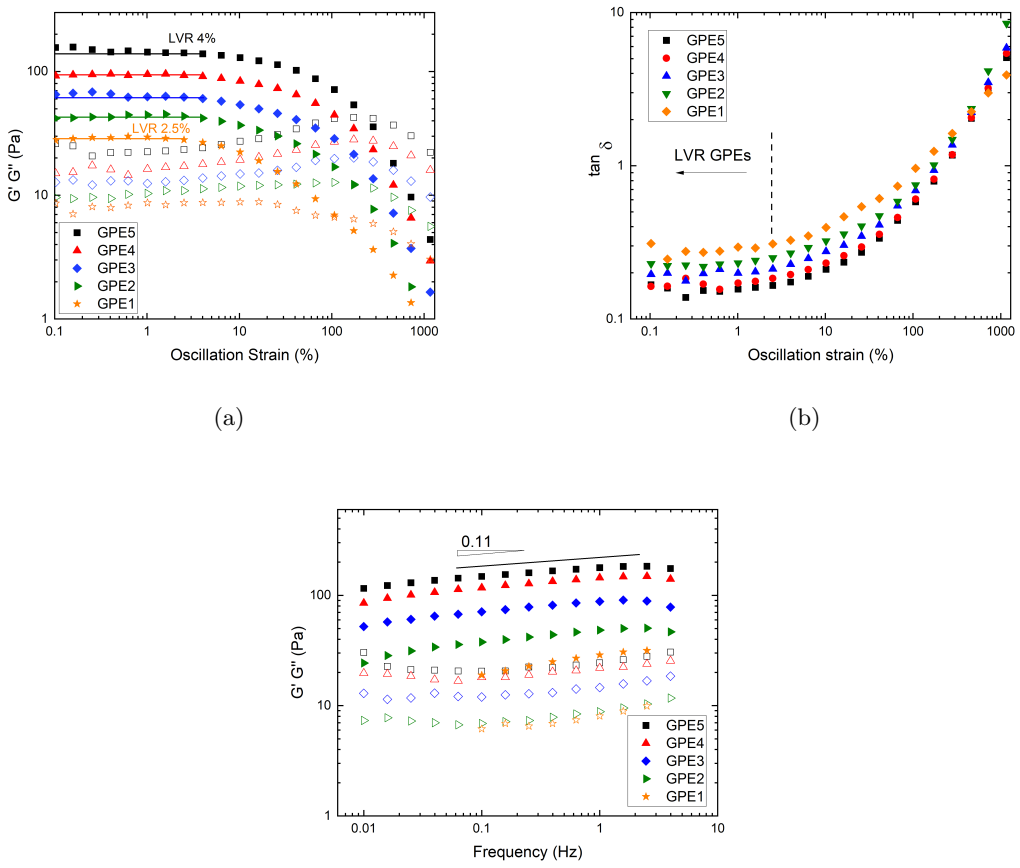

Figure 3.6: Oscillatory rheometry: Strain and frequency sweeps for GPEs. a) Log-log plot of G' (solid symbols), and G'' (open symbols), as function of strain amplitude at 1 Hz. b) tan δ as function of strain amplitude at 1 Hz. c) Log-log plot of G' (solid symbols), and G'' (open symbols), as function of frequency at 0.1 % strain, located in LVR.

Determination of linear domain is observed in figure 3.6(a). Storage G' and loss G'' moduli are represented as function of oscillation strain amplitude, for all GPEs. At low strains, both moduli are independent of strain up to 4 % (except for GPE1, up to 2.5 %), indicating the linear viscoelastic region (LVR). In this region, G' is greater than G'' for all the samples analysed, demonstrating that the elastic portion of the material dominates in the linear regime. When a critical deformation is reached, moduli start to drop before reaching the crossover point.

Beyond this critical strain deformation, the viscous modulus G'' is greater than the elastic modulus G' as the sample is in its fluidized state.

Finally, As PAA concentration increases in GPEs, magnitude of storage and loss moduli increases. This result was expected as the addition of more gelling agent in the formulation results in a material with higher elasticity.

An equivalent representation of linear domain is observed in figure 3.6(b), where $\tan\delta$ (G''/G') is represented as function of oscillation strain. As strain increases, it is seen that ratio between both moduli is constant up to a strain of 2.5 % for GPE1 and 4 % for the rest of GPEs. This result indicates the LVR as previously detected from G', G'' as function of strain (figure 3.6(a)).

GPEs linear viscoelastic behaviour is observed in figure 3.6(c), where G' and G'' are represented as function of frequency. Experiment was performed at a deformation of 0.1%, located in LVR. From this test it is seen that in the range of frequency analyzed, G' is always greater than G'', revealing desired gel-like behaviour. Therefore, this result shows that even at highly alkaline environment in which pH $>$ 14, it is possible to prepare gelled networks using PAA as gelling agent. In fact, there is no moduli crossover happening in the range of frequencies analyzed. This is also reflected in the slight dependence of GPEs to frequency. Elastic modulus behaves following weak power law with an average slope of 0.11, as observed in figure 3.6(c), indicating slight dependence to frequency.

As PAA gel concentration decreases, both moduli value decreases, but gel-like behaviour is still observed for all GPE samples at the lowest frequency tested. Furthermore, oscillations frequencies lower than 0.01 Hz become very irregular for GPE1 because of the low oscillatory torque, so results for this sample range between 0.1 and 4 Hz.

Gel behaviour is interesting because incorporates mechanical resistance from the elastic solid behaviour, being a good candidate to host zinc particles. In order to determine flow behaviour, high deformation measurements were performed and they are depicted in the following section.

3.3.2 GPEs flow behaviour

3.3.2.1 Steady state

Large deformation tests were performed not only to investigate flow behaviour in the non-linear regime but also to evaluate the liquid-solid transition.

Shear stress as function of shear rate for the different GPEs is shown in figure 3.7. These results were obtained using decreasing shear steps as mention in section 3.2.2.2.

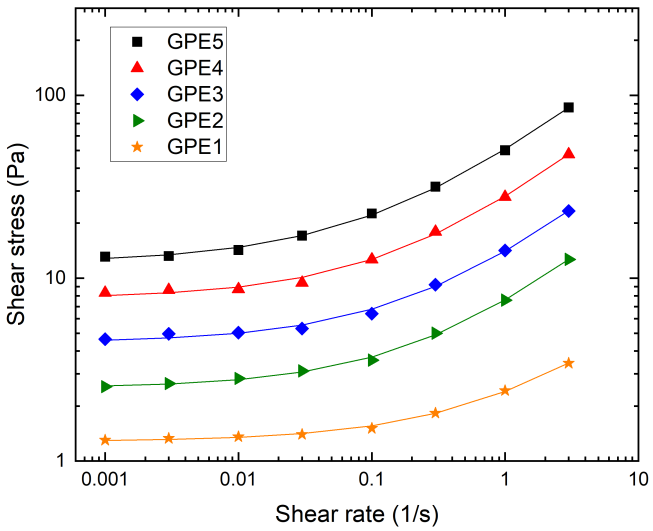

Figure 3.7: GPEs shear stress as function of shear rate. Solid line represents data fitted to Herschel-Bulkley model (Equation 3.1). Closed symbols represent steady state measurement.

It is seen that GPEs behaviour can be that of a yield stress fluid. In fact, at low shear rates there is a tendency to reach a shear stress plateau indicating sample dynamic yield stress. Then, as shear rate increases, shear stress increases following a shear-thinning behaviour. Shear stresses obtained at shear rates $\dot{\gamma} > 3s^{-1}$ were not taken into account because no steady state was found due to the presence of an elastic instability in the vane-in-cup (supporting information figure 3.16(b)). As expected, when PAA concentration increases (from GPE1 to GPE5), shear stress values increase, meaning that there is viscosity increase together with PAA concentration.

For each GPE considered in this study, experimental data was well fitted by a Herschel-Bulkley model (equation 3.1). Fitting can be observed in figure 3.7, represented by solid lines for each GPE. Herschel-Bulkley fitting parameters are summarized in table 3.2.

Sample	**PAA** [**wt. %**]	τ_y [**Pa**]	K [**Pa** s^n]	**n** [**-**]	R^2
GPE1	0.30	1.28	1.12	0.60	
GPE2	0.45	2.51	5.09	0.63	
GPE3	0.60	4.44	9.62	0.62	0.99
GPE4	0.75	7.75	20.27	0.61	
GPE5	0.90	12.15	38.58	0.59	

Table 3.2: GPEs yield stress extracted from Herschel-Bulkley fitting (equation 3.1).

It is observed from table 3.2 that yield stress τ_y increases with increasing PAA concentration, without significant changes in n flow indexes at different PAA concentrations, showing an identical shear-thinning behaviour ($n < 1$). Finally, consistency index K increases as PAA concentration increases.

To study the solid-liquid transition, creep experiments were exploited and analysed to compare yield stress and viscosity behaviour from flow curves.

3.3.3 Creeps

3.3.3.1 GPEs yielding

To determine sample static and dynamic yield stress, creep experiments are performed. Consecutive creeps (following protocol in figure 3.4(a)), for GPE5 can be seen in figure 3.8. This sample is chosen as an example and as the same general behaviour was found for the other GPEs.

Figure 3.8(a) shows the evolution of strain as function of time for increasing applied stresses, studying GPE5 solid-liquid transition. Note that the value of strain is set to zero at the start of each creep step in order to preserve accuracy and avoid rounding errors which become dominant for total strains larger than 10. Only few creep steps considered important are included to ease the reading of the figure. From lower to higher stresses, it is observed at first that strain oscillations appear at $t < 1$ s and they are superposed one to the other. At $t > 1$ s strain increases as a weak power law of time, typical of solids in their creep regime. However, as shear stress is further increased to $\tau = 20$ Pa a different behaviour is observed in which strain at $t > 1$ s increases significantly. Finally, when applying stresses equal and higher than 24 Pa, oscillations disappear and strain increases rapidly with a power law of 1, indicating that the sample is flowing. The transition between these two behaviours is observed and **static** yield

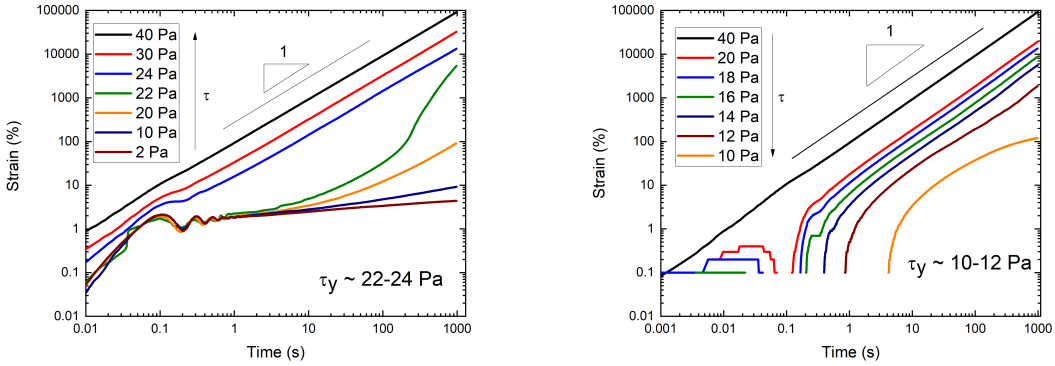

(a) (b)

Figure 3.8: a) Succesive creeps for GPE5. a) Increasing τ steps. b) Decreasing τ steps. $\Delta\tau = 2\ Pa$, $\Delta t = 1000\ s$.

stress of a value approximatively 22 - 24 Pa is observed considering this protocol and time-scale.

Figure 3.8(b) shows creep steps obtained by decreasing stresses. It is observed that oscillations with negative values cannot be represented in the log-log representation. Moreover, the oscillations are present up to times $t < 10\ s$, in comparison with the increasing steps, in which oscillations were observed at times $t > 1\ s$ (figure 3.8(a). From all the curves displayed in figure 3.8(b), only creeps with τ equal to 12 and 10 do not follow a power law of 1. Hence, the value of approximate 10 - 12 denotes the **dynamic** yield stress.

It is important to highlight that when decreasing shear stresses, sample comes from a high deformation regime to a low deformation regime, in which the liquid-solid transition is analysed. Flow is observed down to a stress of 12 Pa (highlighted by the slope with a value of 1), 50 % less of the value recorded from increasing shear stress steps. This value of 12 denotes the **dynamic** yield stress.

From creep tests shown in figure 3.8, it is possible to observe inertio-elastic oscillations at t < 1 s. The analysis done with these oscillations in next section allows us to observe if sample viscoelastic properties change during a succession of decreasing creep steps.

3.3.3.2 Inertio-elastic oscillations

Inertio-elastic oscillations obtained from decreasing creeps steps are fitted to Jeffrey model (equation 3.4). A fitting for GPE5 is seen in figure 3.9. As a result, strain oscillations for this sample are well defined and can be analysed with the model presented.

Figure 3.9 shows that Jeffrey model is able to fit data very well above and close to yield

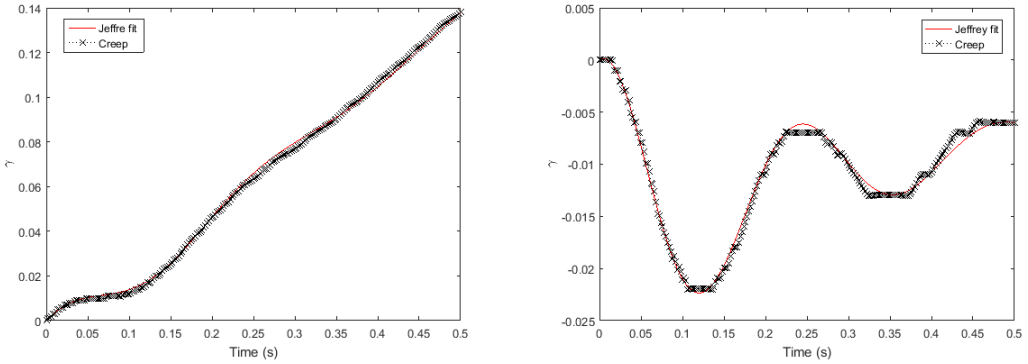

(a) (b)

Figure 3.9: Fitting of strain as function of time for GPE5 obtained by decreasing shear stress steps. Fitting curve corresponds to the red solid line. a) Oscillations during GPE5 creep 24 Pa. $\tau > \tau_y$. b) Oscillations during GPE5 creep 12 Pa. $\tau \approx \tau_y$.

stress. Figure 3.9(a) shows the fitting for a creep performed at 24 Pa. Strain oscillates around a linear increase, showing that flow is developed indicating a viscoelastic fluid. This response was expected because 24 Pa is above GPE5 dynamic yield stress, as seen in figure 3.12. Correspondingly, figure 3.9(b) shows the fitting for a creep performed at 12 Pa, very close to GPE5 yield stress. At this stress, it is possible to observe the elastic response in form of oscillations, belonging to the solid-elastic properties of GPE5.

From Jeffrey fitting (equation 3.4), elasticity G, elastic dissipation η_1, viscosity η_2 and viscosity at the end of each step η are represented for GPE5. Results are shown in figure 3.10.

In figure 3.10(a), elasticity G is analysed. G remains constant at $\tau < \tau_y$ (yield stress from Herschel-Bulkley fitting is highlighted in gray). At $\tau > \tau_y$, G remains stable up to a stress value of 24 Pa. At stresses $24 < \tau \leq 40$, G values are slightly lower compared to the value obtained below yield stress.

Elastic dissipation η_1 is observed in figure 3.10(b). At $\tau < \tau_y$ elastic dissipation η_1 is constant and shows higher values compared to the behaviour at $\tau > \tau_y$, where η_1 decreases progressively as stress increases, down to 38 % of the value obtained below yield stress.

Finally, in figure 3.10(c) it is possible to observe the behaviour of viscosity η_2 and η as function of shear stress. In here, η_2 calculated from Jeffrey model (equation 3.4) at the beginning of each creep step (t < 1 s) is compared with the viscosity η obtained at the end of each creep step. This comparison allows to determine if material presents any thixotropy or viscoelasticity on a time scale larger than the creep steps $\Delta t = 1000$ s (see [Benmouffok-Benbelkacem et al., 2010]). From this result, it is possible to observe that both viscosities converge at stresses $\tau > \tau_y$ when downramping shear stress steps. This results means that in the sample fluidized-state, no time-

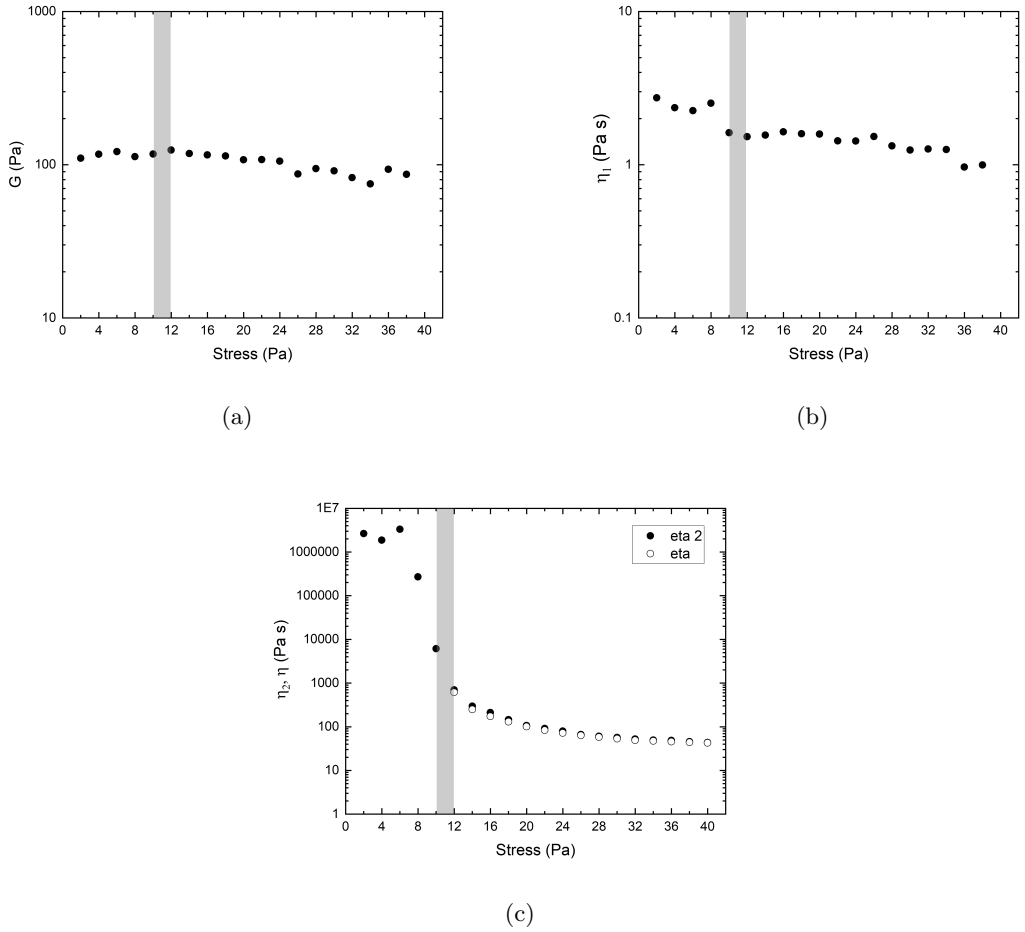

Figure 3.10: Fitting parameters for GPE5 obtained from decreasing successive creeps with a step duration of 1000 s. τ_y obtained from Herschel-Bulkley fitting is highlighted in gray. a) Elasticity G as function of shear stress. b) η_1 as function of shear stress. c) η (open symbols) and η_2 (solid symbols) as function of shear stress.

dependent behaviour is observed, like in neutral Carbopol® gels [Benmouffok-Benbelkacem et al., 2010]. Contrarily, when $\tau < \tau_y$, viscosity η_2 forms a plateau, whereas η, given by the rheometer, is not representative of the sample as GPE is not flowing (strain tends to decrease indefinitely at these stresses), and therefore no viscosity can be associated to it.

3.4 Discussion

GPEs rheological characterisation at small and large deformations are important as gels are prepared to host dense zinc particles in a RFB. Indeed, gels have to ensure a stable network in which sedimentation is reduced when material is at rest, but accompanied by shear-thinning behaviour while pumping during battery operation. In regard of the battery environment, gelling ability of polymers to be used as suspending fluids is very poor at pH > 14. Notably, previous studies have shown that viscosity of PAA, which is the polymer under study for this formulation, decreases significantly at pH higher than 10 [Charman et al., 1991; Gutowski et al., 2012; Lee et al., 2011a; Lochhead et al., 1989]. Therefore, it is important to ensure yield stress properties for GPEs at pH ≈ 14 for zinc slurry - air RFBs with the formulation proposed in this study.

Small deformation tests allowed characterisation representative of sample at rest, important for RFB application when the battery is not in operation (zero flow through the reactor). Frequency sweeps performed at a deformation located in the linear regime (0.1 %), demonstrated that all GPEs behave as a gel material: G' is greater than G'' at all frequencies and there is not moduli crossover (figure 3.6), as the dependece of the moduli towards the frequency is small.

Correspondingly, amplitude strain sweep (figure 3.6(a)) revealed a linear domain (LVR) in which storage modulus is greater than loss modulus, and once a critical deformation is overcome, the sample begins to flow. This behaviour corresponds to the one sought for the operation of the RFB, being a network with a yield stress followed by a shear thinning behaviour. Therefore, to study GPEs flow behaviour in detail, large deformation experiments were performed.

Out of the linear domain, large deformation tests were challenging as GPEs showed a hysteresis loop in which the stress response depended on material initialization/shear history, as observed in figure 3.3. Because of this, a protocol was determined so the rheological characterisation could be accurate and reproducible. When down-ramping either shear rate or shear stress, characterisation is obtained from a known state after initializing the sample. From this starting point, following steps corresponded to sample rheological behaviour and are not influenced by previous shear history. To evidence this point, viscosity from creeps and flow curves for GPE5 are compared and can be observed in figure 3.11.

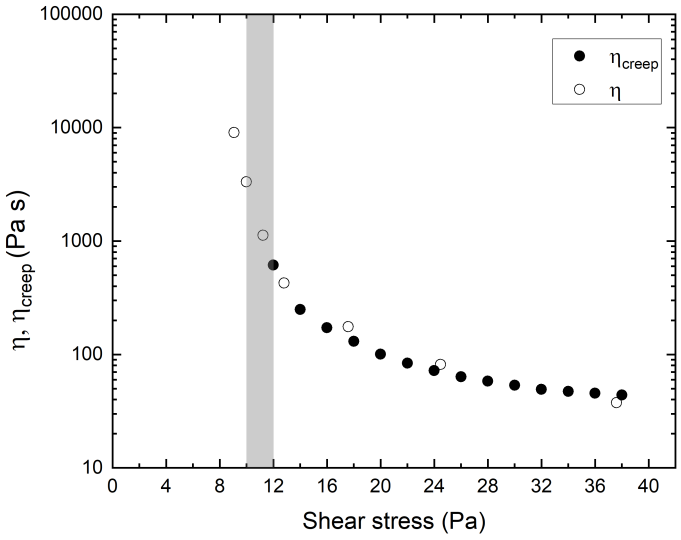

Figure 3.11: Viscosity η and viscosity at the end of creep step η as function of shear stress for GPE5.

Viscosity as a function of shear stress can be seen in figure 3.11 for GPE5. It is seen that the same result is obtained by creeps (η_{creep}) or by applying a constant shear rate (η) as experimental points superpose one to each other. More importantly, a yield stress behaviour is observed. Concretely, viscosity tends to increase indefinitely when approaching to GPE5 yield stress (10-12 Pa). In this range of shear stress observed, we find an agreement between two methods to characterise GPEs rheological behaviour, corresponding to an elasto-visco-plastic material.

Furthermore, this approach is used in all GPE samples to confirm a yield stress behaviour. It is found that when applying decreasing steps, dynamic yield stress values obtained by creeps correspond to the ones determined with Herschel-Bulkley fitting (table 3.2). Yield stress values obtained with these two methods can be seen in figure 3.12.

In figure 3.12(a), viscosity as function of shear stress is plotted for each GPE. Moreover, τ_y obtained from Herschel-Bulkley is represented as a vertical bar for each GPE. It can be seen that viscosity decreases significantly when stresses are higher than the τ_y represented with bars. Moreover, there is a good agreement in characterising the liquid-solid transition with both methods. Shear thinning behaviour is observed as shear stress values increases. Finally, as PAA concentration increases, viscosity is found to be higher, as expected.

Correspondingly, figure 3.12(b) shows that as PAA concentration increases, yield stress values gradually increases. It is seen that there is an agreement between both methods in calculating yield stress values, following a power law as follows:

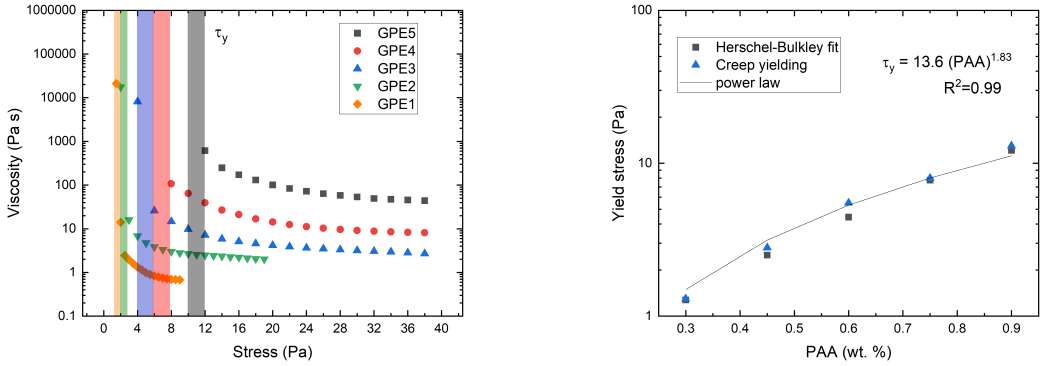

(a) (b)

Figure 3.12: Yield stress behaviour for GPEs obtained from flow curves and creeps. a) Viscosity as function of shear stress. Values of τ_y from Herschel-Bulkley fitting are represented with bars for each GPE. b) Yield stress τ_y as function of PAA concentration obtained by strain controlled and stress controlled experiments.

$$\tau_y = 13.6 \cdot (PAA)^{1.83} \tag{3.5}$$

Where PAA is the polymer concentration in wt. %.

These result suggest that regardless of the method used to determine GPEs yield stress, fluid behaviour will be the same if sample is characterised by imposing decreasing shearing steps, as stated by Ovarlez et al [Ovarlez et al., 2013] and N'gouamba et al. [N'gouamba et al., 2020]. More precisely, Ovarlez et al. found that when increasing shear rates, unsheared regions corresponding to material solid behaviour are present across the sample. These heterogeneous stress fields can appear, as destructuration and restructuration physical phenomenon are in competition when sample undergoes a transition from a solid to fluid-like behaviour.

To verify that GPEs do not show time-dependent properties and validate yield stress behaviour, an experiment was performed on GPE5 as follows. Viscoelastic behaviour was studied during creep experiments by using the inertio-elastic oscillations approach and a Jeffrey model. As observed in figure 3.10(c), η_2 obtained at the beginning of the step ($t < 1\ s$), and η_{creep}, obtained at the end of the step ($t = 1000\ s$) are identical when stress applied is $\tau > \tau_y$. Therefore, no reorganizations or time-dependent properties (in a period of t = 1000 s) were observed for GPE5.

In addition to successfully have found a yield stress behaviour for GPEs, viscosity behaviour in the fluidized state is also critical. Viscosity decrease is very important for energy storage with RFB, as lower viscosities will require less energy for pumping [Iyer et al., 2017]. Moreover, lower

viscosities reduce ohmic and mass-transfer resistances, leading to more efficient and feasible processes [Barton et al., 2018]. As observed in figure 3.12(a), viscosity as function of shear stress is represented together with τ_y. It is observed that at values higher than yield stress, viscosity rapidly decreases and shear-thinning behaviour is clearly seen.

Results obtained in this study by using direct rheometrical methods helped us to characterise GPEs. We found through oscillatory and large deformation rheometry that GPEs can perform good as suspending fluids for a zinc slurry - air RFB. Sought rheological properties were obtained, being gel-like properties at rest and shear-thinning behaviour during pumping.

3.5 Conclusions and Perspectives

PAA gels normally perform great as yield stress fluids, but information at highly alkaline conditions were missing so far. This study is a rheological approach on the study of PAA-based gels at alkaline conditions. With the formulation presented in here, the following outcomes were obtained:

- With the formulation presented in here, using PAA together with attapulgite as gelling agents, it was possible to prepare gels possessing a yield stress and shear-thinning behaviour in highly alkaline conditions (10 M KOH).
- Elasto-visco-plastic properties were found for all GPEs through small and large deformation rheological tests using a Couette analogy approach and a tailored characterisation protocol.
- PAA effect could be quantified by measuring yield stress trough Herschel-Bulkley fitting and creep yielding tests. Moreover we found that τ_y follows a power law as function of PAA concentration (equation 3.5).
- Inertio-elastic oscillations at the start of creep tests were analyzed using a Jeffrey model. Results obtained allowed to confirm that no time-dependent behaviour or re-structuration were observed during rheological characterisation.

This study broadens the knowledge on gels with high concentrations of electrolytes for redox flow battery applications, where viscosity [Barton et al., 2018; Iyer et al., 2017] and yield stress values [Smith et al., 2014; Wei et al., 2015] are key parameters in the overall performance. Furthermore, rheometric characterisation validate GPEs presented in here as good candidates to formulate zinc slurries for RFB in harsh alkaline conditions. Yield stress followed by shear-thinning behaviour was found for all GPEs, indicating that zinc particles can be suspended in

a percolated network and at the same time, network can flow with a decreasing viscosity easing sample recirculation in a zinc slurry - air RFB.

Research efforts were focused in the region where material flows following a yield stress fluid behaviour. In order to determine viscous behaviour at high shear rates, specially at shear rates $> 3\ s^{-1}$ (figure 3.14), a different approach has to be put in place in order to study the effect of elasticity on flow instabilities. Furthermore, the role of attapulgite in the formation of the network needs to be studied to understand the role of this gelling agent in the microsctructure of GPEs and the displayed macroscopic behaviour. This study brings attention to the possibility of preparing GPEs in harsh alkaline environment for RFB application.

3.6 Supporting information

3.6.1 Virtual Couette analogy

3.6.1.1 Analogous cylinder radius and optimal radial position

To determine the analogous radius of the inner cylinder R_i, an experiment in which torque as function of rotational velocity is determined using a fluid of known consistency and flow index (Newtonian fluid ISO 17025, 6166 mPa s, 20 $°C$, Paragon Scientific Ltd). Then, R_i is determined as follows:

$$R_i = \frac{R_e}{\left[1 + \frac{2\dot{\theta}}{n} * \left(\frac{2\pi K h R_e^2}{\Gamma}\right)^{\frac{1}{n}}\right]^{\frac{n}{2}}} \tag{3.6}$$

Finally, by substituting torque Γ and rotational velocity $\dot{\theta}$ obtained by shearing a fluid with well-known rheological properties (n , K), using the vane-in-cup geometry (vane height h and cup radius R_e), an internal radius $R_i = 13\ mm$ for an analogous cylinder is obtained.

It has been found that geometrical factor $K_{\dot{\gamma}}$ is dependent of sample flow index n, a priori unknown. Nevertheless it has been proved that there is a radial position r^* in which $K_{\dot{\gamma}}$ is independent of n [Aït-kadi et al., 2002; Puig et al., 2016]. This optimal radial position is calculated as follows:

$$r^* = \left[\frac{n'}{n} * \frac{\left(\frac{R_e}{R_i}\right)^{\frac{2}{n'}} - 1}{\left(\frac{R_e}{R_i}\right)^{\frac{2}{n}} - 1} * R_e^{\left(\frac{2}{n} - \frac{2}{n'}\right)} \right]^{\frac{1}{\left(\frac{2}{n} - \frac{2}{n'}\right)}} \tag{3.7}$$

Where n and n' are the extreme flow indexes representing the range of shear thinning fluids to be studied. To do the calibration, values of $n = 1$ and $n' = 0.2$ were chosen and a value of $r^* = 15\ mm$ was obtained. In this position r^*, $K_{\dot{\gamma}}$ and K_τ are calculated so both geometrical factors are independent of sample flow index, in the range selected, using equation 5.4.

Geometrical factors calculated with the above information are $K_{\dot{\gamma}} = 2.30\ rad^{-1}$ and $K_\tau = 13450.73\ Pa\ N^{-1}\ m^{-1}$. These factors were validated by comparing shear stress as function of shear rate obtained with two different geometries for a solution of carboxymethylcellulose at 3 wt. %.

In figure 3.13, it is possible to observe raw data Γ vs $\dot{\theta}$, and translated flow curves τ vs $\dot{\gamma}$. It is observed that raw data is shifted by geometrical factors $K_{\dot{\gamma}}$ and K_τ. Once these factors are determined and applied, a good agreement is found between the tested geometries to analyse carboxymethyl cellulose 3 wt. % flow behaviour. It is observed that this fluid shows a shear-thinning behaviour. Finally, it is found that geometrical factors calculated inhere represent accurately the behaviour of non-Newtonian fluids.

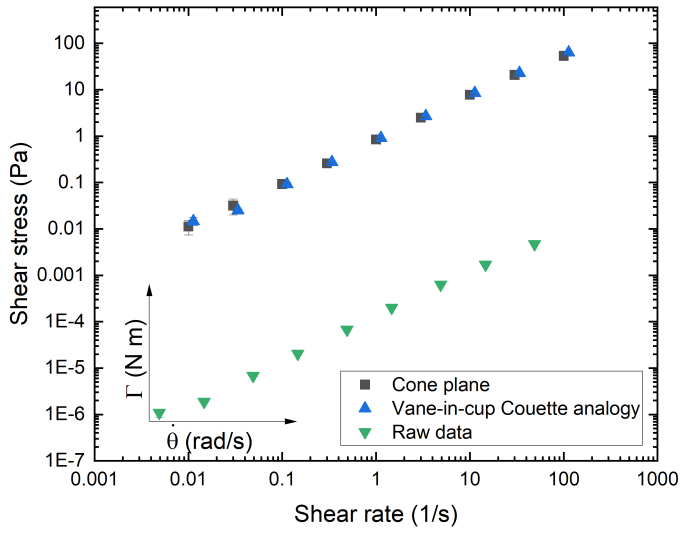

Figure 3.13: Shear stress as function of shear rate for carboxymethylcellulose 3 wt. % using a vane-in-cup calibrated with Cup Analogy approach [Aït-kadi et al., 2002], and a cone and plane geometry. Raw data is obtained with vane-in-cup geometry and points correspond to the axes of rotational velocity as function of torque.

3.6.2 Elastic instability

Values represented in figure 3.14 at shear rates $> 3\ s^{-1}$ are the shear stress values obtained at the end of each step, representing an apparent shear stress. This zone is highlighted in red in figure 3.14, where insets represent the appearance of the free surface area when shearing in a stable zone (white background) or unstable zone (red background). Measurements obtained within unstable zone belong to a transient state where no constitutive equation supports this phenomena [Coussot, 2005].

3.6.2.1 Sample appearance under shearing

Figure 3.15 shows stress response when shear rate is consecutively increased from 0.001 to 100 s^{-1} and then decreased to 0.001 s^{-1} ($\Delta t = 120\ s$). Insets are pictures of sample appearance taken through the transparent cup. When performing the increasing shear rate steps, it is observed that sample appearance at 0.01 s^{-1} is plain and continuous, just like after GPE preparation. When shear rate increases to 1 s^{-1}, small defects start to be seen randomly. Finally, at shear rates $> 3\ s^{-1}$, aggregates can be seen across the whole sample. Once small aggregates form, sample do not go back to its initial smooth appearance. After performing decreasing shear rate steps, sample appearance remain like the one obtained at 100 s^{-1}.

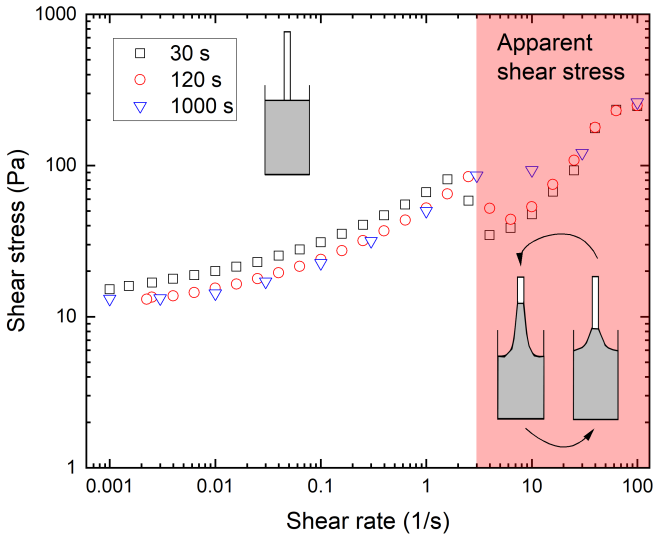

Figure 3.14: Shear stress as function of shear rate for GPE5 obtained by downramping shear rate at different acquisition times: 30, 120 and 1000 s per point. Inset figure indicate sample free surface area while being sheared.

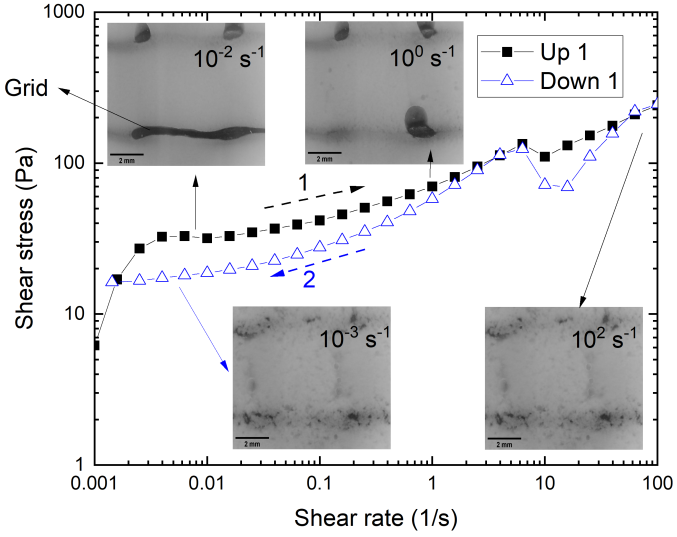

Figure 3.15: GPE5 appearance at different shear rates. Pictures were obtained through the transparent cup.

3.6.3 Determination of shearing time / transient GPEs behaviour

To determine the minimum shearing time to obtain steady state measurements, steps of variable durations were performed while decreasing shear rate. Shear durations of Δt = 30, 120 and 1000 s were investigated.

In order to determine step duration necessary to obtain steady state, the shear stress signal at different shear rates were recorded following the protocol in figure 3.16(a). Shear stress response is obtained and shown in figure 3.16(b) for GPE5.

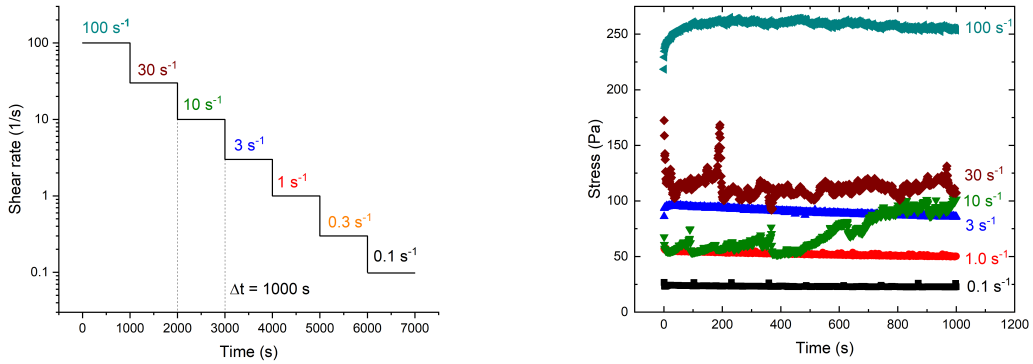

(a) Steady state determination protocol. Sample undergoes consecutively decreasing shear rate steps from 100 to 0.001 s^{-1}. Each step had a duration of 1000 s.

(b) Shear stress signal at different shear rates for GPE5. Shear rates are applied consecutively, down-ramping from 100 to 0.1 s^{-1}.

Figure 3.16: Protocol to determine GPEs steady state.

Shear stress signal as function of time for different shear rates is observed in figure 3.16(b). Initially at 100 s^{-1} shear stress signal is somewhat stable, but small stress fluctuations are perceived. When decreasing shear rate to 30 and 10 s^{-1}, shear stress signal starts to fluctuate significantly, and steady state behaviour is not found. Shear rates higher than 3 s^{-1} produce a phenomenon in which shear stress undershoots as the volume of sheared sample is continuously changing: material tries to climb the shearing geometry, similarly to rod climbing [Weissenberg, 1947]. This can be observed in the video attached in supporting information [`https://rb.gy/pypcww`]. As the sheared volume changes, rheometer struggles to keep up with the imposed shear rate. At shear rate values of 3 s^{-1} and lower, shear stress signal remains stable over time denoting steady state. Because of this, the range of shear rates explored in this study corresponds to $\leq$ 3 s^{-1}, where no perturbations are observed and steady state is reached for all samples.

In order to determine the minimum shearing time to attain steady state, shear stress as function of shear rate for different acquisition times is shown in figure 3.17.

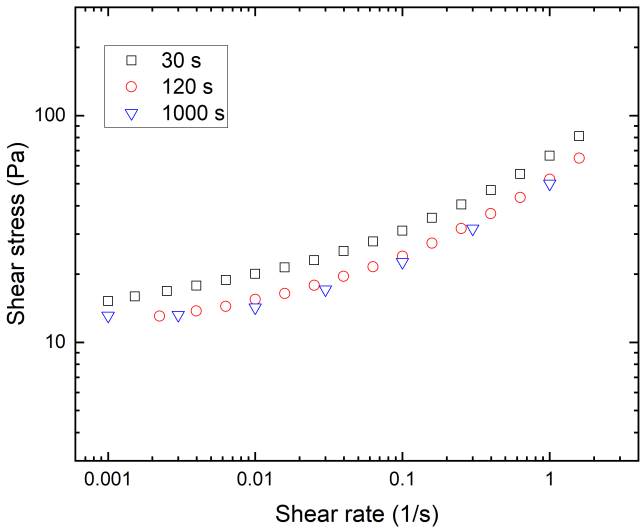

Figure 3.17: Shear stress as function of shear rate for GPE5 obtained by downramping shear rate at different acquisition times: 30, 120 and 1000 s per point. Inset figure indicate sample free surface area while being sheared.

It is observed that for the same material, shearing time has a slight effect on the shear stress response, as seen in figure 3.17. Shear stress as function of shear rate obtained at 30 s per step (□) shows higher shear stress values in comparison to the values obtained by shearing 120 s per step (◯). This means that by shearing just 30 s per point, steady state is not obtained as stress would have continued to decrease over time. On the other hand, it is seen that 120 s is almost enough to reach steady state, when it is compared to 1000 s per step (▽).

To compile the information above, steady state flow curves are obtained by down-ramping shear rate steps. Each step has a duration of t = 1000 s (unless otherwise indicated), to ensure that steady state is attained. Moreover, shear stress values obtained in the range of shear rate $10 \leq \dot{\gamma} \leq 100\ s^{-1}$ are not taken into account, as steady state is not obtained at these shear rates (figure 3.16(b)).

CHAPTER

FOUR

POLYMER – ZINC INTERACTIONS: RHEOLOGICAL DETECTION OF POLYACRYLIC ACID POLYMER ADSORPTION ONTO METALLIC MICROPARTICLES

In this chapter, it is assessed if polyacrylic acid (PAA) is an adequate gelling agent to be used to suspend zinc particles for redox flow battery (RFB) application. In order to do so, potential interaction happening between zinc and PAA are studied, demonstrating that these materials are able to bound and form an interconnected network. This is done by a rheological approach, in which microscopic interactions are studied from a macroscopic point of view. By validating our hypothesis by spectroscopy, rheometry is presented as an accessible and powerful tool to determine interactions when compared to other less accessible direct methods.

Contents

4.1 Introduction

With current energy policies, aiming to drastically reduce greenhouse gases emissions [European Commission, 2019], renewable sources will have a key role in deliver electricity to large communities. However, in order supply reliable, sustainable and resource-efficient electricity, stationary energy storage systems are needed to tackle the drawbacks of renewables intermittencies.

Among several promising solutions, redox flow batteries (RFBs) have gained especial attention due to their design flexibility, cost, safety and ability to decouple power from energy, the latter conferring the ability to tailor its design to meet precise markets. Recently, a different design was proposed to undertake the problem of low solubility compounds affecting battery energy density [Choi et al., 2017]. This design consists in a semi-solid flow cell, in which the electro active materials are suspended in electrolyte media producing a slurry with higher energy density than its aqueous analogue [Duduta et al., 2011]. This approach has been applied to several metal-air batteries, chiefly high energy density zinc-air batteries, reducing anode limitations, like zinc passivation, corrosion and dendrite formation [Fu et al., 2017; Han et al., 2018].

Zinc slurry – air RFB consists mainly in a slurry electrolyte anode, a membrane and an air cathode with a bi functional air catalyst to perform both discharge and charge reactions [Choi et al., 2020a]. However, there is not much information on the development of zinc electrolyte slurries to fulfil this purpose. The anode slurry formulation is not trivial as dense zinc particles ($\rho = 7.13\ g/cm^3$) need to be suspended in electrolyte medium, when in fact they are prone to sedimentation. Furthermore, zinc-air batteries usually operate in concentrated alkaline KOH

electrolyte, in order to prevent corrosion [Visco et al., 2014] and because of its high conductivity [Mainar et al., 2018d]. Nonetheless, in alkaline environment it is difficult to find a gelling agent able to suspend homogeneously zinc particles in concentrated alkaline environment [Nelson et al., 2017].

Despite this, studies have found that polyacrylic acid (PAA) is chemically and electrochemically stable in highly alkaline environment [Tran et al., 2020]. PAA is a carbomer, mostly known by its commercial name Carbopol®. Its chemical structure is shown in figure 4.1. PAA is widely used as a model fluid because of its ideal yield stress behaviour [Curran et al., 2002]. A yield stress fluid will only flow if the stress applied to it is greater than its yield stress. Its behaviour is well-fitted by the 3 parameter Herschel-Bulkley fluid model:

$$\begin{aligned} \dot{\gamma} &= 0 \quad \text{if } \tau < \tau_y \\ \tau &= \tau_y + K\dot{\gamma}^n \quad \text{if } \tau > \tau_y \end{aligned} \tag{4.1}$$

Where τ is the shear stress, $\dot{\gamma}$ is the shear rate and the fitting parameters are τ_y yield stress, K consistency index, and n flow index.

PAA gels are spongy microgels that are defined as colloidal glasses [Emady et al., 2013], in which the yield stress is a macroscopic property of the jammed repulsive interactions in its microstructure [Piau, 2007]. PAA gels have a rheological behaviour highly dependent on pH. When PAA powder is dissolved in water, resulting solution has an acidic pH lower than 4 [Curran et al., 2002]. At this pH polymer chains have a relaxed configuration [Lochhead et al., 1989], as observed in figure 4.1. However, as gel pH is modified by adding a base i.e. NaOH, that will be dissociated in Na^+ and OH^- ions, pH increase to values equal and higher to its pKa (pKa Carbopol = 6.0 ± 0.5 [Lee et al., 2011a]). As it is schematically represented in figure 4.1, in this environment, carboxyl groups in the polymer chain get ionized, meaning that they adopt an anionic form ($-COO^-$) generating repulsion forces that increase internal osmotic pressure [Lochhead et al., 1989]. Consequently, PAA microgels swell towards an expanded configuration (figure 4.1), reaching up to 1000 times its original volume [Lee et al., 2011a]. As a result, PAA microgels compress each other in a jammed arrangement, exhibiting a yield stress behaviour [Oppong et al., 2011].

However, when adding more NaOH, pH is further increased to values higher than 7, and a different configuration of polymer chains is expected. In fact, internal osmotic pressure is reduced as excess counterions Na^+ in solution increase [Lochhead et al., 1989], softening the microgels and reducing elastic macroscopic properties, essentially yield stress.

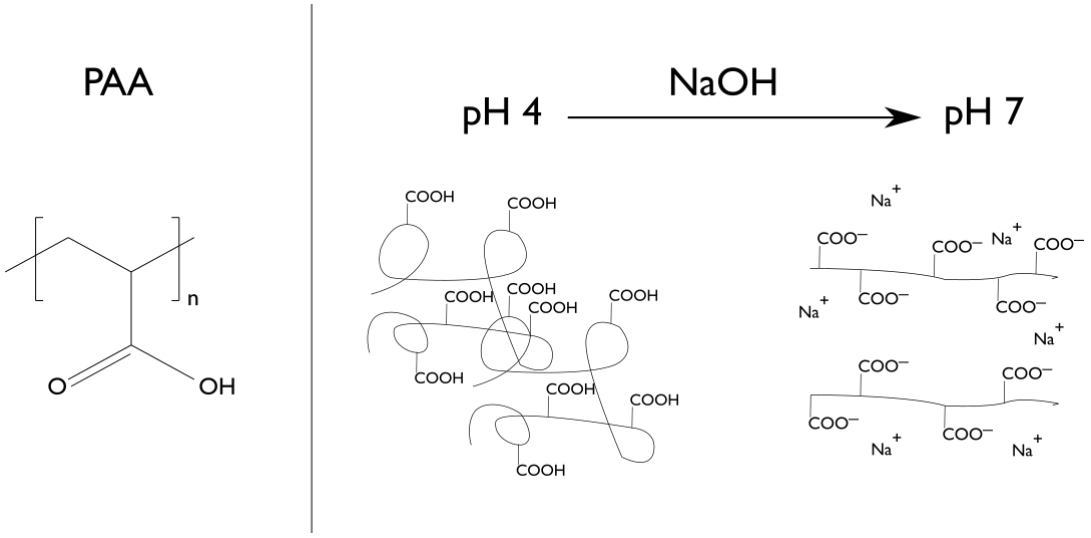

Figure 4.1: PAA chemical structure and schematic representation of Carbopol® polymer chains as function of pH. At a pH 4, polymer chains are randomly distributed in space. As polymer is neutralized to pH 7 with a basic solution of $NaOH$, from which the Na^+ ions come from, carboxyl groups ($COOH$) are ionized to carboxylate ($-COOH^-$), provoking ionic repulsion and microgel swelling.

Thus, if polyacrylic acid (PAA) is chemically and electrochemically stable in highly alkaline environment [Tran et al., 2020], hence it can be considered to formulate zinc suspension for zinc-air batteries. However, it appears that its physical properties, namely its microstructure, and thus the associated yield stress is modified with pH [Lee et al., 2011a]. It is reminded that yield stress is an important parameter to ensure the stability of the suspension regarding sedimentation in particular.

Furthermore, zinc is thermodynamically unstable in water and it releases zinc species in the form of ions in aqueous medium as function of pH [Zhang, 1996]. The species in aqueous equilibrium are shown in the zinc Pourbaix diagram in figure 4.2.

The Pourbaix diagram indicates the predominant zinc species that coexist with metallic zinc at a given pH in water. In the acidic to neutral region (slightly lower than pH 8), metallic zinc dissolves into divalent cations Zn^{2+}. As pH is increased slightly higher than 11, the zinc species in solution are zinc oxide (ZnO) and zinc hydroxide ($Zn(OH)_2$), species that have low solubility in water [Zhang, 1996]. Finally, at pH higher than 11, predominant species in solution are zincate species $Zn(OH)_3^-$ and $Zn(OH)_4^{2-}$. The region between the red-dotted lines represent the water stability region.

According to this diagram, during formulation of zinc suspensions in PAA gels, that are mainly composed of water, dissolution of zinc species will occur into the aqueous gel. More specifically, if PAA gel has a neutral pH 7, the zinc species in solution will be Zn^{2+} divalent cation, based on Pourbaix diagram in figure 4.2.

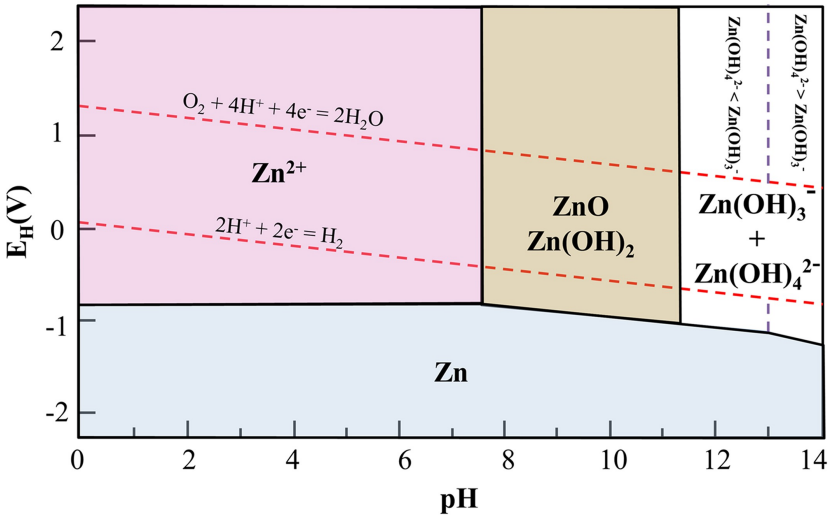

Figure 4.2: Pourbaix diagram of zinc at 25 °C taken from [Mainar et al., 2016].

However, as OH^- are found in solution due to PAA gel neutralization using NaOH as a base, the following reaction can happen [Reichle et al., 1975]:

$$Zn^{2+}_{(aq)} + 2OH^-_{(aq)} = Zn(OH)_{2(c)} \tag{4.2}$$

In which aqueous divalent zinc reacts with hydroxide ions to form zinc hydroxide.

It is thus expected that after preparing PAA gels at pH 7, when zinc particles will be added, Zn^{2+} will be released to aqueous solution and react with OH^-, forming zinc hydroxide $Zn(OH)_2$. The production of $Zn(OH)_2$ can shift the pH of the system to a value in which this species is spontaneously formed. According to results found by Thomas et al. [Thomas et al., 2013], the region in which $Zn(OH)_2$ is formed is around a pH 10, corresponding to the zone presented in the Pourbaix diagram at a pH in the approximate range of 7.5 to 11.5. In summary, it is important to underline that the initial suspension with a pH 7 given by the gel will probably evolve to a suspension with a pH around 10 as an effect of zinc species released in aqueous gel.

It is also important to point out that PAA gels are known to interact with divalent and trivalent cations. In fact, several studies found that viscosity of different polyacrylic acid was reduced when adding divalent cations like Zn^{2+} [Bernkop-Schnürch et al., 1998; Keegan et al., 2007; Singla et al., 2000] and Ca^{2+} [Charman et al., 1991; Mussel et al., 2019; Pringels et al., 2008]. In those studies, it was observed that divalent cations bound with the ionized carboxyl groups ($-COO^-$) from the polymer chain in a proportion 1:2, respectively. When binding takes place, the swelling degree of the polymer decreases [Mussel et al., 2019], softening the jammed structure of the polymer and leading to a yield stress decrease.

Thus, interaction of PAA with divalent cations, as well as increasing pH beyond its pKa value, result in the same effect, namely a decrease of the yield stress.

It is then emphasized that not only physicochemical sample properties, as pH, can lead to a yield stress decrease. Indeed, the presence of ionic species in solution and possible particle-gel interaction can also diminish the gel yield stress. These interactions could modify the physicochemical suspension properties, and consequently, its macroscopic properties.

The objective of this work is to build a stable interconnected network of zinc microparticles in a polymer gel, for redox flow batteries. To test the properties of the proposed PAA network, zinc suspensions in PAA gels are prepared at controlled pH conditions with the purpose of identifying interactions that can be detected by the macroscopic rheological behaviour of PAA gels.

In order to do so, PAA gel is first studied alone to determine the effect that polymer concentration and pH can have on its rheological behaviour. In fact, lets underline that yield stress is a key parameter of a percolated network and for the prevention of sedimentation in suspensions.

Next, the effect of the addition of zinc particles to the gel is studied with the objective to characterise zinc-PAA interactions. For this purpose, zinc suspensions of different PAA and zinc particle concentrations are prepared and then centrifugated. Our hypothesis is that PAA and zinc will bound after formulation and hence, centrifugation will make zinc particles settle together with the potentially bound PAA polymer. If some of the PAA is indeed bound to zinc particles, a polymer-depleted supernatant will be recovered after centrifugation, and its polymer concentration will therefore be lower than the initial polymer concentration of the suspension. Hence, zinc-PAA interactions will lead to a polymer concentration decrease in supernatant. To evaluate this hypothesis, the concentration of polymer in the supernatant will be determined by different means.

The first approach consists in a rheometric method that we will refer to as "inverse rheometry". This method will allow to calculate PAA concentration from supernatant rheological properties accordingly to its physicochemical properties, especially its pH. This method will be presented in section 3.4.

A second qualitative approach consists in labelling the polymer using rhodamine dye [Dinkgreve et al., 2018] and then quantifying its presence in supernatants. This method will be presented in section 4.2.5.

The presence of zinc-PAA interactions are an indication that an interconnected percolated network can be built using PAA polymer, in which PAA will not only transport ionic species

crucial for the cell reaction, but also effectively suspend zinc particles avoiding sedimentation. Thence, the presence of such interaction have to be carefully detected and studied.

4.2 Materials and methods

4.2.1 Polyacrylic acid (PAA) gel preparation

Polyacrylic acid (PAA) gels of different concentration were prepared as follows. An initial solution with a final volume of 700 ml at 0.30 wt. % of PAA gelling agent (Carbopol® 940, Acros Organics), is prepared by adding the polymer to deionized water in a 2 L beaker under continuous agitation, using a magnetic stirrer at 800 rpm. PAA polymer was added slowly under continuous stirring to avoid the formation of visible aggregates that take longer times to be dissolved. PAA initial solution is stirred for 24 h at 100 rpm to ensure full polymer dissolution and hydration [Varges et al., 2019].

From this initial solution, gels with different concentrations were prepared by dilution, adding deionized water and stirring with a magnetic stirrer at 800 rpm for 2 hours. Studied concentrations were 0.10, 0.15, 0.17, 0.20 and 0.30 wt. %. These concentrations were selected to be close to the rheological properties, chiefly yield stress, of slurries used in a RFB [Chapter 5]. All dilutions and original gel had a pH 3.6, measured with an Orion Star A215 pH meter (Thermo Fisher Scientific), using a pH/ATC rechargeable electrode (Orion™ ROSS Ultra™ Triode™).

As PAA gels rheological behaviour change as function of pH [Lee et al., 2011a], samples pH was adjusted to 4, 6, 7, 8, 9, 10, 11, 12 and 14 to study its effect on yield stress. Adjustment of pH was done by adding drop by drop of a freshly prepared NaOH 18 wt. % solution in deionized water (NaOH Pellets, Sigma Aldrich) [Varges et al., 2019]. As viscosity increases together with pH, gels are mixed when adding NaOH by using a vacuum paddle-mixer (Vacuret-S, Reitel GmbH), ensuring proper mixing and avoiding the formation of bubbles by imposing a vacuum (-0.8 bar). After reaching the desired pH, samples were mixed one supplementary hour to ensure NaOH diffusion through the gel. Finally, samples were stored at ambient temperature for 24 h and a final pH-check was done to ensure testing conditions prior to any analysis.

4.2.2 Zinc suspensions preparation and supernatant recovery

Zinc particles (Zinc powder battery grade, GN 7-4/200Bi/200In, Grillo GmbH), were used as received. Their size distribution was characterised using laser diffraction granulometry

(Mastersizer 2000, Malvern Panalytical). The results showed a Gaussian disperse distribution with a characteristic $D_{50} = 76.4\mu m$ [Chapter 5]. Let us recall that D_{50} represents the average particle diameter by mass.

To prepare zinc suspensions that will be later centrifuged, only PAA gels at pH 7 were used in which carboxyl groups are ionized. To do so, PAA gels were placed separately in 25 mL centrifuge tubes. Next, for each PAA gel concentration considered, zinc particles are added in the tubes and mixed using a spatula first, followed by a vortex shaker (Vortex-Genie® 2, Scientific Industries), until observing with naked eye that zinc particles are homogeneously distributed in the gel. Zinc particle concentrations considered for each PAA gel are 0, 10, 20, 30, 40 and 60 wt. % of the total sample weight. Suspension total weight was set so at least 7 g of PAA could be recovered after centrifugation. In this way the total weight of suspension prepared for a zinc concentration ranging from 10 to 40 wt. % was 13 g, and for 60 wt. % was 20 g.

As zinc suspensions are not neutral-buoyant systems (i.e. particle density equal to suspending fluid density), they can undergo sedimentation [Ovarlez et al., 2015]. In order to avoid 2-phase system formation in which polymer will not be in contact with the zinc particles, zinc suspensions are left under continuous agitation at 10 rpm using a rotating mixer (RM5, Assistant®, Hecht glaswarenfabrik GmbH & Co KG), as observed in figure 4.3.

Figure 4.3: Zinc suspensions under continuous mixing using a tube roller mixer.

After 24h, samples were centrifuged at 500 rpm for 10 min and supernatant was extracted for characterisation with a pipette as represented schematically in figure 4.4.

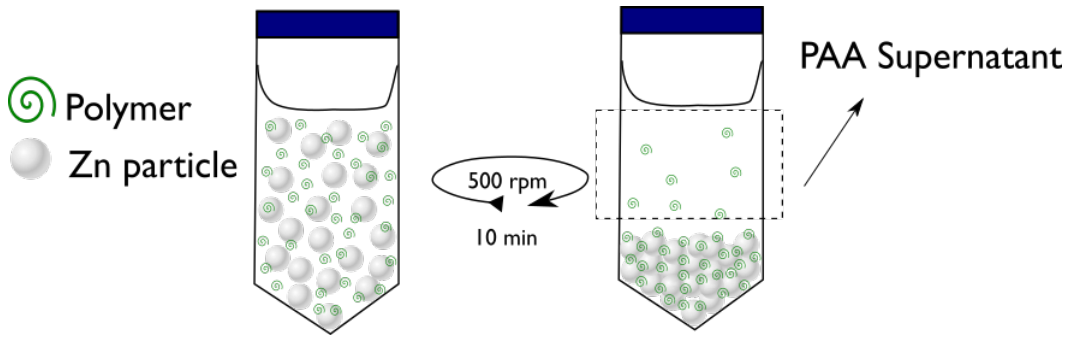

Figure 4.4: Zinc suspension centrifugation to obtain supernatant with remaining PAA polymer.

No zinc particles corresponding to their characteristic size D_{50} were observed after centrifugation, as discussed in supporting information figure 5.1(a).

Supernatants recovered after centrifugation will be addressed as S_{p_Zn}, where p and Zn are respectively the PAA polymer and the zinc concentration in the parent suspension in wt. %. We underline that in this appellation, S_{p_0}, corresponds simply to the PAA gel that was used to prepare the corresponding zinc suspension and its associated supernatant.

4.2.3 pH measurements

For each supernatant S_{p_Zn}, pH was determined using an Orion Star A215 pH meter (Thermo Fisher Scientific), using a pH/ATC rechargeable electrode (Orion™ ROSS Ultra™ Triode™). These properties were monitored in regard with their potential impact on PAA gel rheological behaviour, namely yield stress τ_y [Lee et al., 2011a].

4.2.4 Rheological measurements

The effect of pH on PAA gels was studied through shear stress as function of shear rate flow curves. In addition, the effect of zinc concentration on PAA gel recovered from supernatant S_{p_Zn} is also studied with the same approach.

Samples rheological characterisation was performed at 20 °C using a stress-controlled rheometer DHR-3 (TA-instruments) equipped with a cone-plate geometry. The cone had a radius of 25 mm and an angle of 2 degrees. Both cone and plate had rough surfaces to avoid sample slippage [Magnin et al., 1990]. The experiment was protected from potential solvent evaporation by using a solvent trap. Steady state measurements were performed by applying constant shear

rate steps. Measurements were performed two times by increasing and decreasing shear rate steps to check reproducibility. Lastly, steady state flow curves were fitted to Herschel-Bulkley model (Equation 4.1) to determine rheological flow parameters, chiefly yield stress τ_y.

When viscosity of the sample was found to be too small to be characterised by a cone-plate geometry, a microviscometer (Lovis 2000 microviscometer, Anton Paar), based on the rolling ball principle was used [Hubbard et al., 1943].

4.2.5 Labelling and UV-Vis spectroscopy

Labelling of PAA polymer is used to determine concentration of PAA still present in supernatant. The dye used to label is rhodamine 6G (Sigma Aldrich), which has a maximum absorption at a wavelength of $\lambda = 525\ nm$. Additionally, rhodamine possess positive charges when dissolved in water. Carboxyl groups ($-COO^-$) found in neutralized polymer, as observed in figure 4.1, can bind with cationic groups found in rhodamine dye, conferring the ability to label polymers [Beija et al., 2009; Haack et al., 2017]. In this way, it is presumed that rhodamine dye can bind to the polymer chain as reported by [Dinkgreve et al., 2018], thus allowing to quantify its presence by adequate UV-Vis spectroscopy measurements.

In order to label the gel, a concentrated PAA gel was prepared and then diluted with a solution containing the rhodamine dye. First, a 0.5 wt. % PAA gel is prepared and neutralized at a pH of 7 following the same procedure indicated in section 4.2.2. In parallel, a solution of rhodamine 6G 10^{-5} M is prepared by diluting the dye in deionized water. Next, PAA gel was diluted to a final concentration of 0.10 wt. % using the rhodamine solution. In this step, rhodamine found in the aqueous solution binds to PAA polymer. Finally, labelled-PAA gel is stirred continuously in the paddle-mixer for 1 hour to ensure dye diffusion into the PAA gel. At the end of this step, a pH measurement is done to ensure a neutral pH of 7. Only PAA 0.10 wt. % and the associated supernatants $S_{0.10\_Zn}$, were considered to analyse the results of polymer labelling.

Once labelled-PAA gel is set, different zinc suspensions are prepared as indicated in section 2.2, considering zinc concentrations of 0, 1, 2, 3, 4, 5, 7, 10 and 20 wt. % of zinc. These concentrations were selected as concentrations of zinc higher than 20 wt. % produced turbid supernatants that are not possible to be analysed by spectroscopy method. Samples are maintained under agitation at 10 rpm in rotating mixer (figure 4.3) for 24 h before obtaining supernatant by centrifugation (500 rpm for 10 minutes). Then, rhodamine 6G concentration of supernatants $S_{0.10\_Zn}$ were determined through the measurement of the sample light transmission, using a UV-Vis spectrometer (Red Tide USB650 Fiber Optic Spectrometer, Ocean Insight). The working principle of UV-Vis spectroscopy is illustrated in figure 4.5.

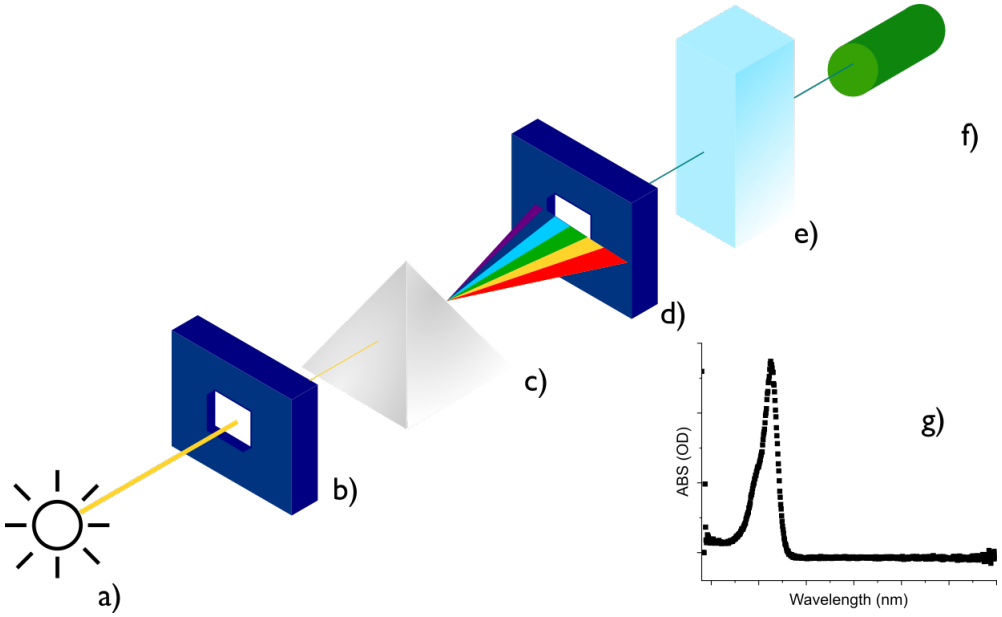

Figure 4.5: Scheme of UV-Vis working principle used for the supernatants obtained from suspensions of zinc particles in labelled PAA polymer. The light from a light source **a)** enters through a slit **b)**, where the amount of light and its wavelength is regulated. Next the light beam is diffracted by a grating (or prism) **c)**, and directed onto a focusing mirror **d)**. Finally, light interacts with the sample **e)**, which is placed in a cuvette specially made for UV-Vis spectrometers. The light transmitted through the sample is collected by a detector **f)**. The detector converts the optical signal into digital signal. An example of the absorption spectra can be seen in inset **g)**, where an absorption characteristic peak is registered for a given substance.

UV-Vis spectrometers detect transmitted light. Nevertheless, this information can be converted into light absorbance to eventually detect the absorbance peak characteristic of rhodamine by using the following equation:

$$A = log_{10}(I_0/I) \tag{4.3}$$

Equation 4.3 is known as the Beer-Lambert law, where A is the absorbance, I_0 is the intensity of the incident light and I is the transmitted intensity.

Using equation 4.3, a calibration curve is constructed allowing to correlate light absorption to different rhodamine concentrations. To do so, rhodamine solutions of concentrations in the range of 0.5 - 25 μM were prepared by dissolving dye powder in deionized water. Concentrations higher than 25 μM were not tested as absorbance linearity is nor respected. Next, their light absorbance was measured at a wavelength of $\lambda = 525\ nm$, which corresponds to rhodamine absorption peak. To eliminate the effect of the solvent, which in this case is deionised water for both PAA gels and rhodamine, a reference sample containing deionised water was measured to subtract its absorbance. Once the reference sample is considered, results of adsorption

are representative for rhodamine dye in solution. Calibration curve displaying rhodamine adsorption as function of its concentration is shown in figure 4.6.

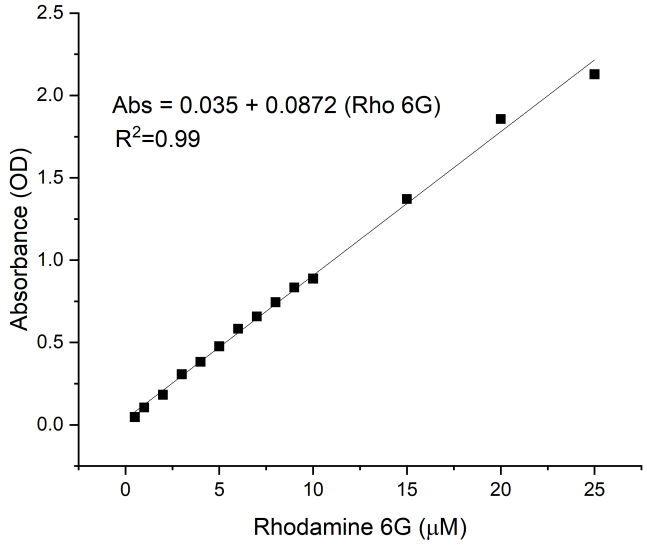

Figure 4.6: Absorbance as function of rhodamine 6g concentration obtained from UV-Vis spectra ($R^2 = 0.99$).

The characteristic absorbance of rhodamine at $\lambda = 525\ nm$ is represented as function of rhodamine concentration in μM. It is observed that calibration curve shows a linear dependence ($R^2 = 0.99$), within the range of concentrations studied.

Absorbance curves of supernatant $S_{0.10\_Zn}$, obtained from the centrifugation of the different zinc/labelled-PAA suspensions are obtained using UV-Vis spectroscopy. With the aid of the correlation curve (figure 4.6), concentration of rhodamine, and thus concentration of labelled polymer, in supernatant is obtained from absorbance values. As rhodamine is bound to PAA, its concentration in the supernatant is directly related to the polymer concentration in the supernatant. Consequently, it will be possible to determine if PAA concentration recovered from the centrifugation is lower compared to the initial PAA gel. This method is qualitative because the concentration determined is just proportional to the actual concentration in supernatant. If the statement is true, it means that there is a fraction of the polymer that sedimented with zinc particles during centrifugation, as a consequence of zinc-PAA interactions. Therefore, this method allows to characterise the zinc-PAA interactions from the concentration comparison.

4.3 Results

4.3.1 PAA flow flow curves: influence of pH

First, flow behaviour of PAA gel 0.10 wt. % at different pH is displayed in figure 7. 4.7.

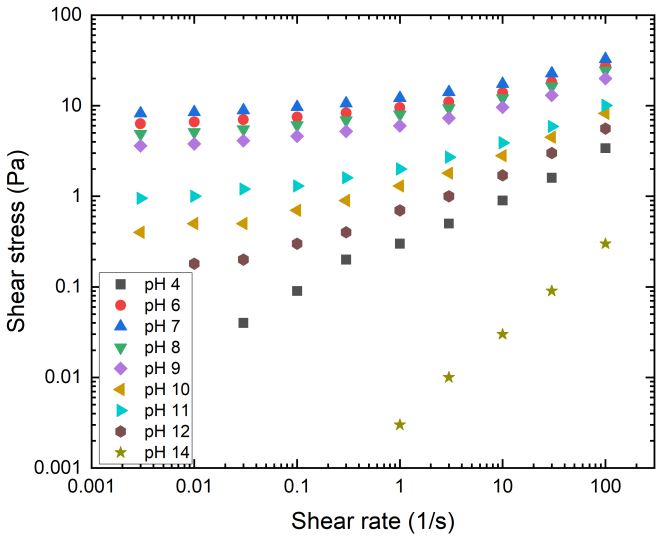

Figure 4.7: Shear stress as function of shear rate for PAA gel 0.10 wt. % at different pH.

The shear stress response to a shear rate is shown to depend strongly on pH. Two main behaviours can be observed from the data set in the pH range studied. For the lowest and highest pH, being 4 and 14 respectively, a viscoelastic behaviour is observed. Conversely, for gels at pH from 6 to 12 a viscoplastic behaviour is observed, evidenced by the yield stress followed by shear thinning behaviour. In addition, it is observed that shear stress values increase with increasing pH up to a pH of 7, where shear stresses found a maximum value. As pH is further increased, shear stresses values decrease. As previously explained, higher pH can lead to the weakening of the network by modifying the swelling degree of PAA microgels, softening the jammed structure [Lee et al., 2011a].

The same experiments were performed on PAA gels concentrations 0.15, 0.17, 0.20 and 0.30 wt. %. It was found that shear stress values incremented as PAA concentration increased. In like manner, the same result was obtained in which shear stress values found a maximum at a pH 6-7, before decreasing at higher pH.

For gels showing a viscoplastic behaviour, yield stress values were determined. To do so, shear stress as function of shear rate flow curves were fitted to Herschel-Bulkley model (equation

4.1), and the resulting yield stress is represented as function of pH for different concentrations in figure 4.8. It is important to notice that for gels with a viscoelastic behaviour, a value of zero was assigned to the yield stress.

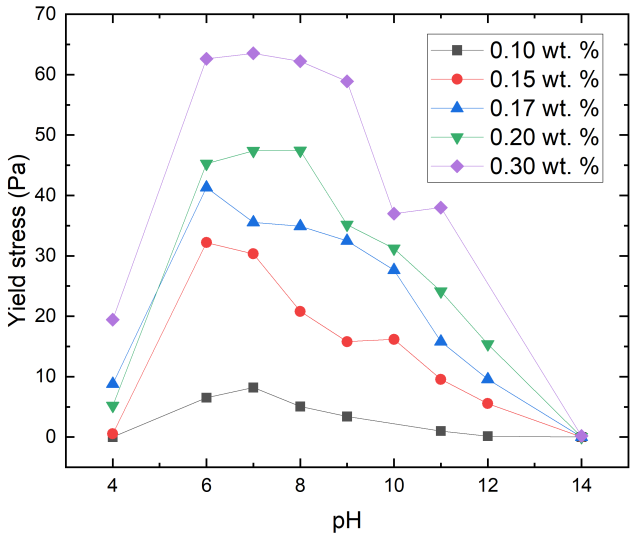

Figure 4.8: Yield stress τ_y obtained from Herschel-Bulkley model (equation 4.1), as function of PAA pH.

It is thus clearly observed that for all PAA concentrations tested in this study, ranging from 0.10 to 0.30 wt. %, yield stress first increases as pH increases reaching a maximum at pH 6-7, before decreasing as pH is further increased. These results are in agreement with what is reported in literature, in which the ionization state and osmotic pressure in PAA chains at different pH will determine its rheological behaviour [Gutowski et al., 2012; Lee et al., 2011a; Piau, 2007].

In an analogous representation, yield stress values are represented as function of polymer concentration for different pH in figure 4.9.

It is observed that concentration has a strong effect on yield stress and two behaviours are observed. At concentrations lower than 0.15 wt. % of PAA, yield stress is strongly dependent of concentration, where significant increase is observed. Then, at concentrations higher than 0.15 wt. %, the dependence diminishes. This tendency is observed independently of the pH at which gels are analysed.

These results are in agreement with those presented in a review paper by Piau [Piau, 2007], identifying two different scaling laws for yield stress τ_y as function of PAA concentration in Carbopol® 940 gels at pH 7. The relations are the following:

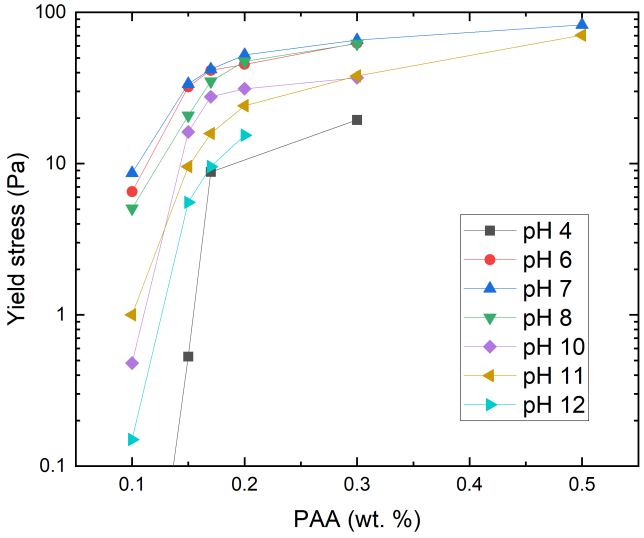

Figure 4.9: PAA steady state rheometry. Yield stress τ_y as function of PAA concentration at pHs ranging from 4 to 12.

$$\begin{aligned} \tau_y &= \left(\frac{[PAA]}{0.0335} - 1\right)^3 \qquad [PAA] \leq 0.15\ wt.\% \\ \tau_y &= 45\left(\frac{[PAA]}{0.124}\right)^{1/3} \qquad [PAA] > 0.15\ wt.\% \end{aligned} \tag{4.4}$$

Where $[PAA]$ is the PAA concentration in wt. %. The exponents in equation 4.4 indicate that concentrations effect become weaker as PAA concentration is increased at values higher than 0.15 wt. %, concentrations at which power index is reduced by a factor of 9.

Our results for neutral PAA gels (pH 7) are compared to those proposed by Piau [Piau, 2007], and displayed in figure 4.10. This clearly shows quantitative agreement between our results and the equations 4.4.

From the literature and from our rheometrical characterisation of PAA gels, it is observed that viscosity and yield stress are highly pH dependent. Therefore, in the following of this study, it will be crucial to measure the pH in the gels and supernatants beforehand, in order to determine their rheometrical behaviour in relation to the real physicochemical conditions.

At this stage, it is important to remember that, as we have seen from the analysis of the Pourbaix diagram (figure 4.2), while the gels are neutralised at pH 7, the addition of zinc for the preparation of the suspension results in a pH increase that can reach a value of around 10. When supernatant obtained after centrifugation is studied, pH modifications should be

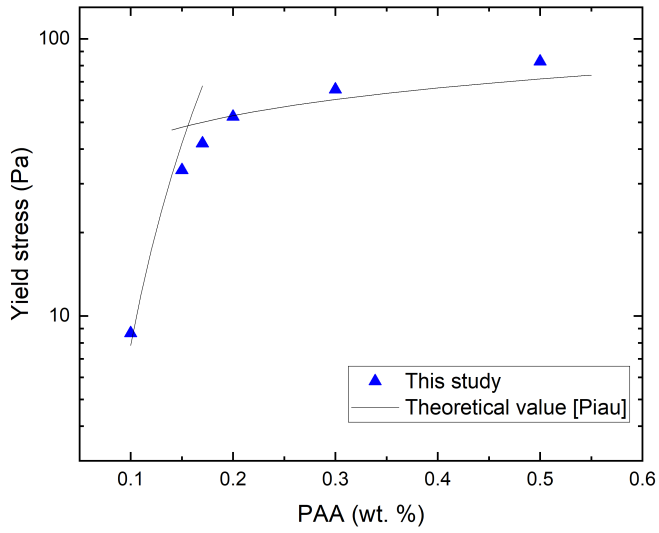

Figure 4.10: Yield stress τ_y as function of PAA concentration at pH 7 from our study and from [Piau, 2007].

considered in its characterisation to be done correctly.

4.3.2 Supernatant pH

After supernatants S_{p_Zn} were obtained through centrifugation, pH measurements were performed. Results are displayed on figure 4.11.

It is recalled that initial PAA gels ($S_{0.10\_Zn}$) have a pH of 7 at the time of preparing the suspensions. In figure 4.11 it is observed that after obtaining the supernatant by centrifugation, the effect of the lowest zinc particles concentration used to prepare parent suspension, being 10 wt. %, is observed as a pH increase to values close to 11. Then, for suspensions prepared with higher zinc particle concentrations, pH values remain close to 11.

This effect is observed for all polymer concentrations tested in this study. As presented in the introduction, the increase of pH has an origin in the new equilibrium obtained after zinc species Zn^{2+} are released to aqueous media, according to Pourbaix zinc diagram in figure 4.2. The sample conditions favour the formation of zinc hydroxide $Zn(OH)_2$ [Reichle et al., 1975], which its concentration is maximized in the range of pH 8 and 11, as found by our measurements.

Accordingly, it is underlined that pH of supernatants is different from the initial gel, and the rheological behaviour of these ought to be interpreted at their corresponding pH, which

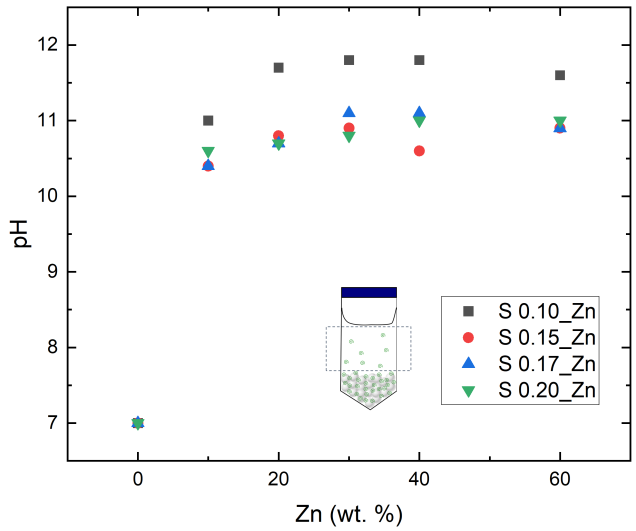

Figure 4.11: Supernatant pH obtained from centrifugation as function of zinc concentration in parent zinc suspensions.

has a value of 11 due to equilibrium found with the zinc species in dissolution.

4.3.3 Supernatant flow curves

Steady state flow curves for different supernatants S_{p_Zn}, obtained from centrifugation of samples prepared with different PAA concentrations, are presented in this section. Figure 4.12 shows steady state results for a concentration of 0.15 wt. %, mixed with zinc particles at concentrations ranging from 0 to 60 wt. %. We recall that these results are for supernatants having a pH of 11.

On figure 4.12(a), initial PAA gel 0.15 wt. % ($S_{0.15\_0}$ in black squares), shows as expected a viscoplastic behaviour, with a yield stress at low shear rates, followed by shear thinning behaviour.

Then, as zinc concentration is increased in parent suspensions, it can be observed that the corresponding supernatant obtained from centrifugation shows lower shear stress values, indicating a less viscous material. Shear thinning behaviour is observed whatever the formulation considered to prepare supernatant.

Flow curves were fitted to Herschel-Bulkley model (equation 4.1) and yield stress is determined and displayed in figure 4.12(b). In fact, it can be seen that yield stress behaviour is maintained for the supernatant obtained from centrifugation of zinc suspension with zinc

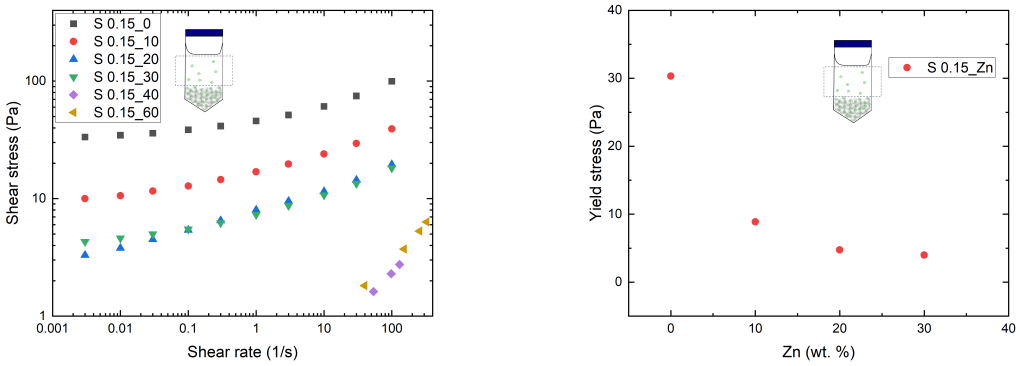

(a) (b)

Figure 4.12: Supernatants steady state rheometry at pH 11. a) Shear stress as function of shear rate obtained for different supernatants $S_{0.15\_Zn}$ b) Yield stress as function of zinc wt. % for $S_{0.15\_Zn}$. Yield stress was obtained from fitting experimental data to Herschel-Bulkley model (equation 4.1).

concentration up to 30 wt. % ($S_{0.15\_30}$). At this concentration however, yield stress value decreased by a factor of 7.5, as compared to that of $S_{0.15\_0}$. Finally, yield stress is no longer observed for $S_{0.15\_40}$ and $S_{0.15\_60}$.

These results show that if parent suspensions are more concentrated in zinc, the recovered supernatant will be less gelled, therefore indicating less polymer compared to the initial gel used to prepare zinc suspensions. Let us recall that the parent suspension has an invariable polymer concentration, set at 0.15 wt. % in this case. Given that the initial amount of polymer is constant, if less polymer is found in the supernatant after centrifugation, it is suggested that there is a certain amount of polymer interacting with zinc particles, which settles together with zinc during centrifugation. The amount of polymer that interacts and sediments with zinc particles increases when the zinc concentration used to prepare suspensions increases.

This first indication of zinc-PAA interactions will be evaluated by other approaches later in this paper.

The same rheometrical measurements were performed on supernatant obtained from the centrifugation of zinc suspensions, with polymer concentrations of 0.10, 0.17 and 0.20 wt. %. Results are shown in figure 4.13. It is remarked that preparation of zinc suspensions with PAA concentrations of 0.30 wt. % and higher concentrations resulted in non-reproducible heterogeneous samples, so they were left out of the study.

Supernatants obtained from suspensions prepared from PAA gel 0.10 wt. % are observed in figure 4.13(a). It is observed that original gel $S_{0.10\_0}$ has a viscoplastic behaviour denoted by the yield stress. In fact, as zinc particle concentration in parent suspension is increased, shear

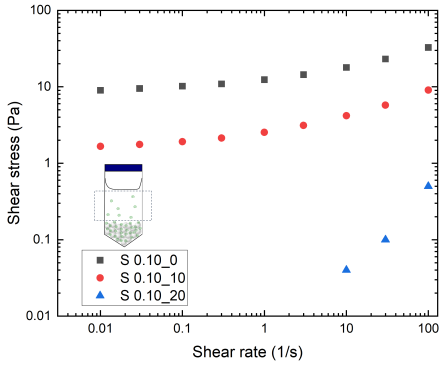

(a) PAA 0.10 wt. %

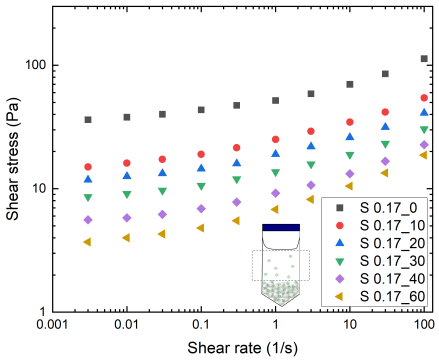

(b) PAA 0.17 wt. %

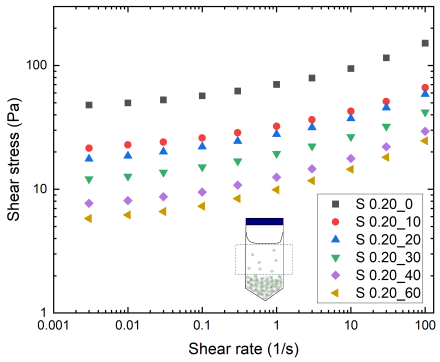

(c) PAA 0.20 wt. %

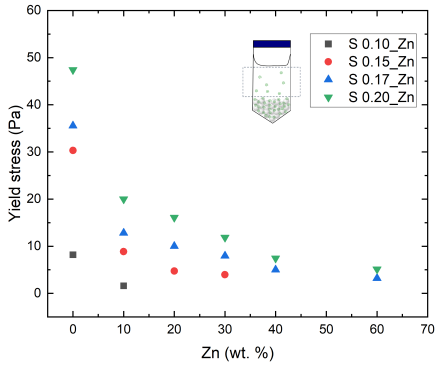

(d)

Figure 4.13: Supernatants steady state rheometry at pH 11. a) $S_{0.10\_Zn}$, b) $S_{0.17\_Zn}$ and c) $S_{0.20\_Zn}$ shear stress as function of shear rate obtained from centrifugation of zinc parent suspensions. d) Supernatants S_{p_Zn} yield stress as function of zinc wt. % for different PAA concentrations. Yield stress was obtained from fitting experimental data in figure 4.12(a) and 4.13(a), 4.13(b), 4.13(c) to Herschel-Bulkley model (equation 4.1).

stress values decreases. Moreover, as equivalently observed for $S_{0.15\_Zn}$ in figure 4.12(a), it is observed that at a zinc concentration of 20 wt. %, viscoplastic behaviour has already vanished.

For supernatants prepared from PAA gel 0.17 wt. % and 0.20 wt. %, in figure 4.13(b) and 4.13(c), respectively, it is observed that shear stress decreases as zinc concentration used to prepare zinc suspensions increase. It is remarked that for these initial PAA concentrations, viscoplastic behaviour is observed whatever the zinc concentration considered in the studied range from 10 to 60 wt. %.

Flow curves in figure 4.12(a) and 4.13 were fitted to Herschel-Bulkley model (equation 4.1) and yield stress is obtained for all supernatants showing viscoplastic behaviour. This result is displayed in figure 4.13(d), in which supernatant S_{p_Zn} yield stress is represented as a function

of zinc concentration of parent suspension.

Principally, a general trend is observed in which supernatant yield stress decreases as zinc concentration is increased for all the PAA concentrations considered. As previously observed in flow curves, the higher the zinc particles concentration, the more important is the yield stress decrease in supernatants, therefore indicating the direct effect of zinc concentration in PAA properties as a result of interactions.

To summarize the above findings represented in figure 4.12 and 4.13, regarding the rheometrical behaviour of supernatants, it is observed that for all initial PAA concentrations, as zinc concentration of the parent suspension is increased, supernatant viscosity and yield stress values decrease. Notably, as zinc concentration is increased, resulting supernatants after centrifugation are less gelled, thus indicating that there is less polymer. This may be associated to the fact that as more zinc is added to initial gel of given polymer concentration, more polymer can interact and then sediment together with zinc, clearly leading to a depletion of polymer in supernatant.

It is thus clear, that the flow behaviour of the supernatant depends on the zinc concentration of the parent suspension. This leads to the possibility of an interaction between the polymer chains and the zinc particles: the polymer bound to the zinc is centrifuged and remaining polymer is found in the supernatant.

In order to validate this hypothesis, the polymer concentration in the supernatant has to be quantified.

This will be done first by a method that we refer as inverse rheometry. The aim here is to determine "free polymer" concentration in supernatant by rheometric means. In this method, yield stress at supernatant pH is considered. Then, by using figure 4.9 in which the yield stress is correlated to a PAA concentration at a given pH, PAA concentration in supernatant, otherwise "free polymer", can be deduced.

Other polymer quantification methods like measuring the residual polymer by obtaining total dry extract in the supernatant are not straightforward as there are other zinc compounds in solution affecting the final result (supporting information 4.6.1). However, a qualitative method is proposed by labelling the polymer using rhodamine and then following its presence in supernatants using spectroscopy. This method will be presented as a second way to quantify the polymer concentration in the supernatant. Moreover, it allows to observe the decrease of polymer in solution as a consequence of zinc-polymer interactions.

4.3.4 Zinc polymer interactions: Inverse rheometry

4.3.4.1 Yield stress behaviour at pH 11

PAA gel yield stress obtained from Herschel-Bulkley fitting (equation 1), as function of PAA concentration for a pH 11 is taken from the log-lin plot in figure 4.9, and displayed in a linear representation in figure 4.14.

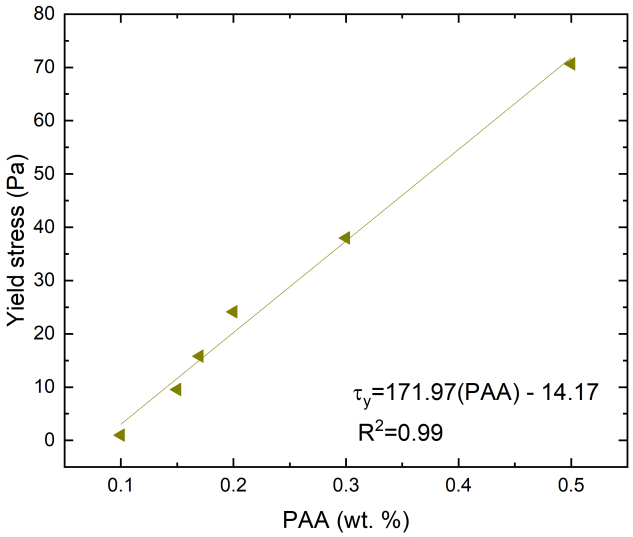

Figure 4.14: Yield stress of PAA gel as function of PAA concentration at pH 11.

It is observed that a linearity is found within the polymer concentrations analysed for a pH 11. It is reminded that these samples are pure gels that have not been in contact with zinc particles, so their rheological behaviour has not been modified. A yield stress interpolation can thus be done between PAA concentrations of 0.10 and 0.50 wt. %, using the following equation:

$$\tau_y = 171.97[PAA] - 14.17 \qquad R^2 = 0.99 \tag{4.5}$$

Where $[PAA]$ concentration is in wt. %.

The inverse rheometry method that will be used below is based on figure 4.14 and equation 4.5. By knowing the yield stress value of a PAA gel, this method allows to introduce τ_y value in equation 4.5 to deduce the polymer concentration of the gel, the supernatant in this case of study.

4.3.4.2 Free polymer concentration in supernatant by inverse rheometry

According to the inverse rheometry method, the yield stress values obtained from supernatant (figure 4.14) are used in equation 4.5 to calculate the polymer concentration in supernatant. It is pointed out that, according to our hypothesis considering zinc-PAA interactions, this concentration is representative of the concentration of "free polymer" that remains in the supernatant after centrifugation of the suspension.

We define then $[PAA]_{supernatant}$ be the concentration of the "free-polymer" remaining in the supernatant, $[PAA]_0$ being the polymer concentration in the parent suspension, before centrifugation. Thus, the ratio $[PAA]_{supernatant}/[PAA]_0$ will be an indication of the proportion of "free-polymer" remaining in the supernatant as compared to the initial amount $[PAA]_0$. This ratio will be equal to 1 if all the initial amount of polymer is found free in the supernatant, thus indicating that no interaction with zinc has occurred.

The ratio $[PAA]_{supernatant}/[PAA]_0$ is represented as function of zinc concentration in parent suspension in figure 15, for each zinc/polymer suspension considered in this study.

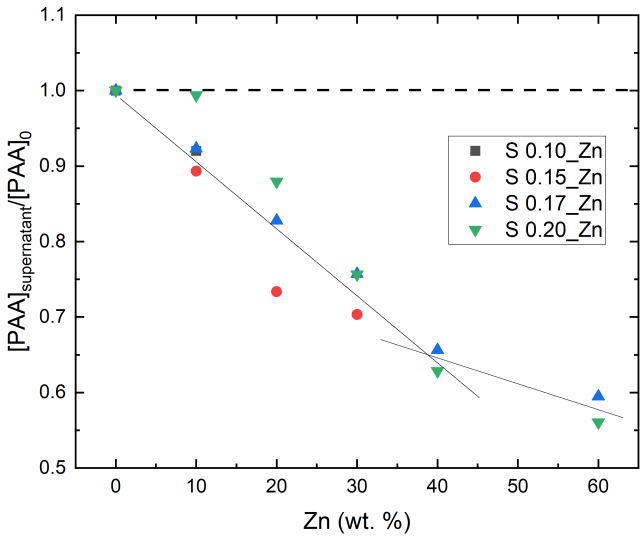

Figure 4.15: Fraction of remaining PAA in supernatant determined by inverse rheometry approach as function of zinc concentration in parent zinc suspension. $[PAA]_{supernatant}$ is determined from equation 4.5, using the values of yield stress in figure 4.13(d). $[PAA]_0$ is the initial known concentration of the PAA polymer (S_{p_0}). Dashed line represents the condition in which no zinc-PAA interactions occur. Calculations are done by considering supernatant pH 11. Solid lines are visual guides to ease the reading of the figure.

This figure clearly shows that the proportion of free polymer in the supernatant decreases as the concentration of zinc used in the parent suspensions increases. This result indicates that

for a gel prepared at a given polymer concentration, as more zinc particles are used to prepare suspension, more polymer will be involved in the interactions with zinc, which will automatically result in a lower concentration of free polymer in the supernatant after centrifugation.

The reduction of available polymer in the supernatant is rapid at first and seems to slow down for zinc concentrations above 40 wt. %. Note that the lines shown in figure 4.15 are not extrapolations but a visual aid to the reading of the figure. This result can be attributed to the increase in the viscosity of the material as the zinc particles are added, resulting in a reduction in the kinetics of the Zinc-PAA interactions. Adsorption kinetics are known to decrease as sample viscosity increase [Eugénie et al., 2014; Wright et al., 1998].

A further reading of this result is given by an analysis of figure 4.15 according to the initial concentration of PAA polymer. It is thus clear that the higher the polymer concentration, the lower will be the overall effect of a given zinc particle concentration on the gel. Specifically, a given number of particles will create the same number of interactions regardless of the PAA concentration. Therefore, for a given concentration of zinc, if the initial concentration of PAA is high enough, the supernatant obtained after centrifugation will be sufficiently rich in polymer and will be able to maintain a viscoplastic behaviour. However, if the initial concentration of PAA is low, it is possible that a large part, if not all, of the available polymer is involved in the interactions with Zinc. This would result in a supernatant with a low polymer concentration and a behaviour that would no longer be viscoplastic but viscoelastic. This is indeed the case for $S_{0.10\_Zn}$ and $S_{0.15\_Zn}$ for which the polymer concentrations of the supernatant cannot be determined by inverse rheometry (see figure 4.13(d)) beyond zinc concentrations of 10 and 30 wt. %, respectively. It is essential to notice that there is 90 % of PAA in concentration for $S_{0.10\_10}$. However, it is observed that when increasing to 20 wt. %, a viscoplastic behaviour is not found in $S_{0.10\_20}$. This result is due to the fact that from the beginning, $S_{0.10\_Zn}$ has a low concentration of PAA, so 90 % of this concentration is already close to the threshold in which a viscoplastic behaviour is still found. The same can be said for $S_{0.15\_30}$, for which 70 % of polymer is still available, but further increase leads to a viscoelastic behaviour.

This approach, based on the study of the viscoplastic properties of the supernatant obtained after centrifugation of a zinc/PAA suspension, allows us to highlight the presence of polymer in the supernatant in a lower quantity than the initial quantity of polymer. The missing polymer probably sediment with zinc particles during centrifugation. We thus have free polymer in the supernatant contrary to the bound polymer, having probably interacted with the zinc, in agreement with our hypothesis.

However, this is an indirect method of revealing potential zinc-PAA interactions. Other methods to quantify the concentration of PAA in the supernatant such as obtaining polymer dry extract were tested but the results were not satisfactory, as explained in section 4.6.1 in

supplementary information. In order to support the above results, another qualitative method is used to determine polymer concentration in supernatant. This method involves labelling the polymer with a dye which will be traced by UV-Visible spectroscopy.

4.3.4.3 Polymer labelling and qualitative detection by UV-Vis spectroscopy

Labelling of PAA using rhodamine and preparation of zinc/labelled-PAA suspensions is performed as described in section 4.2.5. It is recalled that zinc concentration in the range of 1 - 20 wt. % were used for this method. The corresponding supernatants are obtained after centrifugation and are characterised by UV-Vis spectroscopy. Using the calibration curve (figure 4.6), rhodamine concentration was obtained from sample absorbance, as indicated in section 4.2.5.

The concentration of rhodamine obtained in supernatants $S_{0.10\_Zn}$ as function of the zinc concentration in parent solution is shown in figure 4.16.

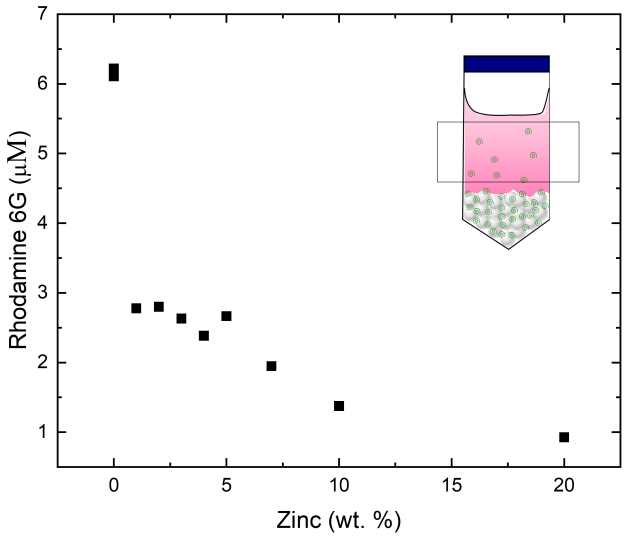

Figure 4.16: Rhodamine concentration determined from calibration curve (figure 4.6), in supernatant $S_{0.10\_Zn}$ as function of zinc particle concentration used to prepare parent zinc suspensions.

It is observed that indeed, and in agreement with the results obtained through inverse rheometry, rhodamine concentration decreases as zinc used to prepare zinc suspension increases. At a zinc concentration of 1 %, rhodamine concentration decreases abruptly and then continues to decrease at a weaker pace as zinc concentration increases up to 20 wt. %. It is reminded that higher zinc concentrations were not pursued because samples became turbid, altering final result.

This result clearly demonstrates, by direct measurement of the dye, the presence of polymer in the supernatant. As said before, this is the free polymer, as opposed to the bound polymer having interacted with the zinc and probably sedimented with it during centrifugation. It also shows that the concentration of rhodamine remaining in supernatant, which is proportional to free PAA concentration, decreases as increasing zinc particles are used in parent suspensions, thus producing more zinc-PAA interactions. This result agrees with the previous inverse rheometry results.

4.4 Discussion

In the previous sections, results indicated that supernatant recovered from centrifugation is depleted in polymer, as a result of zinc-PAA interactions. Moreover, the possible effect of pH is also taken into account, and the decrease in concentration cannot be just allocated to the softening of microgels, leading to lower yield stresses as pH is further increased.

In order to describe the nature of the interactions that could happen with a PAA gel and zinc particles, several tests were performed on pure gels and supernatants obtained from the centrifugation of zinc suspension. It is reminded that if a lower PAA concentration is found in supernatant compared to initial PAA concentration in pure gel, it is attributed to polymer bound to zinc particles that sedimented during centrifugation step, depleting the supernatant in PAA. To validate our statement, rheometric measurements and UV-Vis spectroscopy experiments were performed. Other tests including the recovery of the dried extract did not work as dissolved zinc species are also found in the supernatant and when dried, it is not possible to discern between PAA and other zinc species (supporting information 4.6.1).

From the results obtained in the previous sections 4.3.4.2 and 4.3.4.3 it was indeed observed that there was a modification of rheological behaviour in supernatants as zinc concentration in suspension was increased. Specifically, supernatant yield stress decreased as zinc concentration increased. By means of inverse rheometry, supernatant yield stress was then converted to remaining polymer concentration in supernatant using equation 4.5. Furthermore, if we consider that the viscoplastic behaviour is due to the presence of PAA polymer, hence the results obtained by inverse rheometry, in which less free PAA polymer in supernatant was found as zinc concentration increased, indicates a potential interaction with zinc particles.

In like manner, the polymer labelling approach, in which rhodamine binds with PAA, allowed us to validate inverse rheometry results by determining a decrease in rhodamine as function of zinc particles used in parent suspensions. When labelled-polymer binds to zinc particles, the rhodamine that was already in the polymer settles in the centrifugation step,

leading to a depletion of dye-polymer in supernatants. As observed in figure 4.16, a decrease in rhodamine concentrations, obtained by spectroscopy means, occurs as zinc concentration is increased. Hence, confirming the results obtained from our inverse rheometry method.

In addition, the results from labelling the polymer prove that a part of initial PAA polymer is removed from supernatant in the centrifugation step in the following way. If it is was just the effect of pH modifying PAA gel properties, the same amount of polymer would be available in supernatant when compared to original gel $S_{0.10\_0}$, but in a softer form because of the higher pH. As absorbance values were found to be lower for supernatants than for original gels, the rhodamine in solution had to be gone elsewhere together with PAA polymer. Hence, the evidence brought by labelling, even if just qualitative, it is very useful to demonstrate that zinc-PAA interactions took place reducing the free PAA polymer concentration in supernatant.

There is the question of the origin of the possible interactions, and a deconvolution of the possible effects that can lead to a decrease in yield stress behaviour observed in figures 4.12 and 4.13. When measuring the pH of the supernatants, it was observed that their pH increased to values around 11. As observed in section 4.3.1, it is known that yield stress values decrease at a pH 11 when compared to the original pH 7.

Hence, the question raised here is if the decrease in yield stress observed in supernatants is either an effect of the solution pH or an effect of the interaction happening between zinc and PAA polymer chains and leading to less PAA available in the supernatant.

Nonetheless, pH is already taken in account when doing inverse rheometry: equation 4.14 is obtained from values of yield stress determined for several PAA concentrations in pH 11. In order to rule out that yield stress decrease is only an effect of pH, yield stresses values for supernatants S_{p_Zn} are compared to the pure gel S_{p_0} yield stress at a pH 11. This comparison is depicted in figure 4.17.

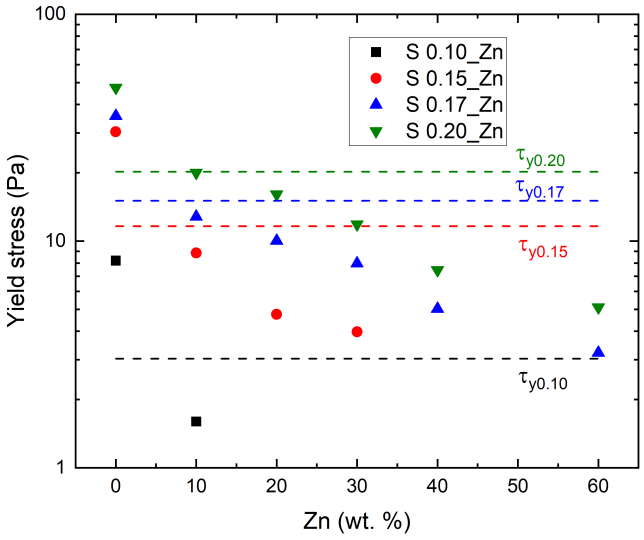

Figure 4.17: Log-lin representation of figure 4.13(d). Yield stress as function of zinc concentration used to prepare parent zinc suspensions. Dotted lines represent PAA yields stress at a pH 11 for gels only (S_{p_0}). Points represent the yield stress measured for each supernatant S_{p_Zn}.

It is then observed that yield stress of supernatants $S_{0.10\_Zn}$, $S_{0.15\_Zn}$, $S_{0.17\_Zn}$ and $S_{0.20\_Zn}$ decrease to values lower than the yield stress value at pH 11 corresponding to gels $S_{0.10\_0}$, $S_{0.15\_0}$, $S_{0.17\_0}$ and $S_{0.20\_0}$, respectively. Thence, even if a pH of 11 can produce a decrease in PAA yield stress, pH is not the only effect triggering this decrease as values of yield stress are lower than predicted. In other words, if the pH is not the origin of the yield stress decrease found in supernatants, the other option to consider is the interactions happening between PAA and zinc, modifying the rheological behaviour of the samples.

By having analysing different possibilities, it is then possible to validate our inverse rheometry approach presented in figure section 4.3.4.2, in which is concluded that a depletion of polymer takes place as zinc particle concentration is increased (figure 4.15). Compared to other methods, like spectroscopy in which turbidity of the samples can limit the analysis, rheometry is introduced as an accessible and powerful tool to describe interactions happening in microscopic scale.

Furthermore, the interactions in which PAA is bound to zinc particles, demonstrate that a network can be stablished when adequate PAA concentration is used to interconnect and suspend zinc particles. This property is important for electrochemical application, like RFB batteries, in which ions can travel through the built network facilitating the ionic mobility.

4.5 Conclusion and perspectives

Zinc suspensions were prepared in order to study interactions taking place between zinc microparticles and a PAA gel, being Carbopol® 940. First, yield stress of pure gels was investigated as function of concentration and pH. the values of yield stress for different concentrations of PAA at a pH of 11 are found to be rather useful to link rheological supernatant properties to PAA gels. Specifically, the pH of supernatants obtained after centrifugation of zinc suspension was found to increase from 7, the pH at which PAA gels were originally prepared, to a final pH of 11.

Next, by acknowledging the pH at which the supernatants were analysed, rheometric characterisation of supernatants allowed us to verify our primary hypothesis being that PAA concentration in supernatants S_{p_Zn} is lower compared to the original polymer concentration S_{p_0}, as the bound PAA was sedimented together with zinc particles in a centrifugation step. By means of inverse rheometry, a concentration of "free-polymer" was calculated (figure 4.15) identifying a net decrease of PAA concentration in the supernatant. This latter statement is validated through the results obtained by labelling PAA with rhodamine and following its concentration in supernatants by spectroscopy means. It was found that rhodamine dye decreases in supernatant as PAA was bound to zinc during sedimentation.

This study demonstrated that PAA is a suitable gelling agent to suspend particles to be used in a zinc slurry – air RFB. As demonstrated by out methods presented in here, interactions indicate that a zinc-PAA interconnected network can be prepared when using a sufficient amount of initial PAA concentration, suppressing possible sedimentation that can be detrimental to the performance of a RFB.

More research efforts are needed to understand the kinetics of the interactions happening between PAA polymer and zinc particles, in particular the viscosity effect and time. Moreover, it is important to investigate the magnitude of the interactions at different initial pH other than 7. In this way, predictions can be done depending on the electrolyte system of a zinc – air RFB, as they can operate in acidic, neutral and basic electrolytes [Mainar et al., 2018d].

4.6 Supporting information

4.6.1 Drying experiment

A first attempt to determine interactions/adsorption of PAA chains onto zinc particles was done by performing the drying of PAA supernatant S_{p_Zn}, and to compare the weight of the

remaining solid content to the original PAA mass used to prepare the pure gel. The drying consisted in evaporate the water in an oven at 70 °C for 24 h. When the water was evaporated (dried extract weight did not further change), the weight was considered to be representative of solid material. If the adsorption process happens, the PAA mass obtained from the supernatant S_{p_Zn} should be lower than the initial PAA mass used to prepare the pure gel S_{p_0}. PAA adsorbed was obtained with equation 4.6:

$$PAA_{adsorbed} = PAA_0 - PAA_{supernatant} \tag{4.6}$$

Where PAA_0 is the PAA mass to prepare a gel S_{p_0}, and $PAA_{supernatant}$ corresponds to the weight found in dried extract of a given supernatant S_{p_Zn}.

However, it was found that the solid content found in supernatant was higher than the initial mass. This resulted on negative adsorption values as observed in figure 4.18.

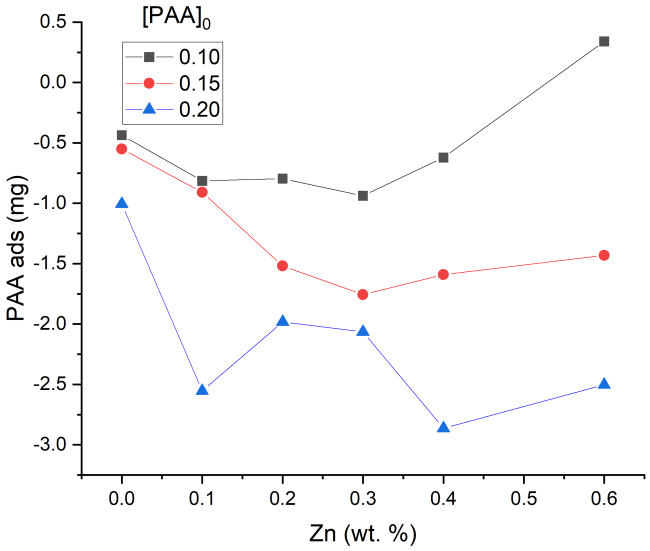

Figure 4.18: Drying experiments to determine adsorption.

In order to determine the origin of the final weight increase, the dried sample was analysed using a scanning electron microscope equipped with an energy dispersive X-ray spectroscopy (SEM-EDS). A beam of electrons is directed to a surface to excite the material, and as a response secondary electrons are generated, which can be used for imaging (SEM). As secondary electrons are generated, surface atoms become ionized and in order to return to its initial state, an electron from the outer shell is captured. At this point, photons are emitted, and by measuring the energy of the photon, it is possible to detect which element is being observed.

An elemental analysis was performed and the results are shown in figure 4.19.

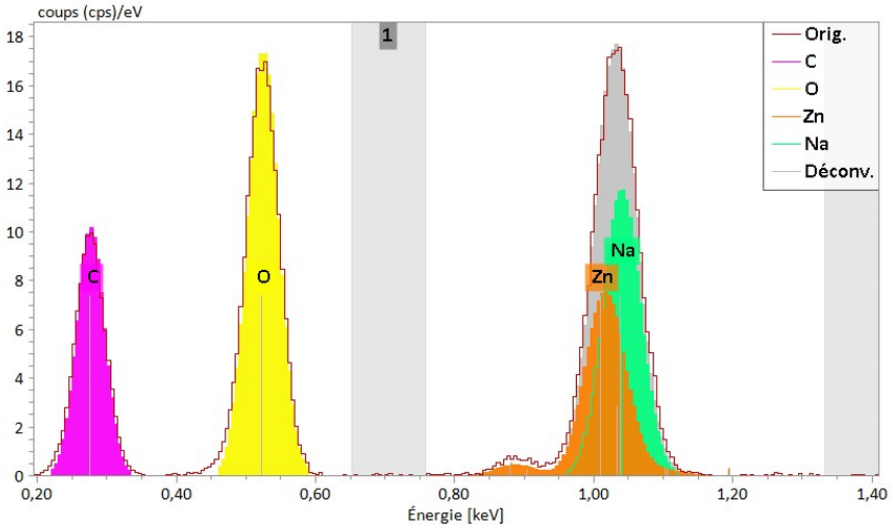

Figure 4.19: EDS deconvoluted spectra from dried $S_{0.15\_20}$

It was found that aside of organic elements like C and O, corresponding to the organic composition of PAA, Zn element was also quantified in the dried supernatant. A SEM picture depicted in figure 5.1(a) indicate that the zinc species in question is not a metallic zinc particle, as the particles used in this study have a $D_{50} = 76.4\ \mu m$.

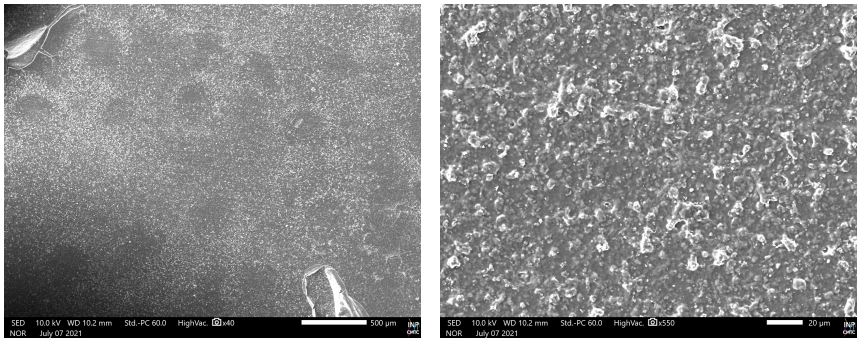

(a) (b)

Figure 4.20: SEM picture of dried supernatant $S_{0.15\_20}$. a) x 40 Scalebar = 500 μm. b) x 500, scalebar = 20 μm.

In this study, suspensions are prepared from a PAA gel at a pH of 7. From Pourbaix diagram (figure 4.2), it is indicated that Zn^{2+} is released in aqueous solution. Moreover, as explained in introduction, there is a new equilibrium found in which the pH increases to 11, favouring the formation of zinc species like ZnO and $Zn(OH)_2$. Moreover, these compounds tend to form crystalline deposits [Mainar et al., 2016]. Therefore, this is the proposed origin for the zinc species found in the dried supernatant obtained from drying.

CHAPTER

FIVE

FORMULATION AND CHARACTERISATION OF ZINC SLURRIES FOR ZINC SLURRY - AIR RFB: A RHEOMETRY APPROACH

In this chapter, rheometry is introduced as an optimization tool to increase discharge performance of a zinc slurry - air redox flow battery (RFB). Incorporation of electrode suspension slurry to metal-air batteries, in which dense metal solid microparticles are suspended in a conductive fluid with the aid of gelling agents is investigated. Electrochemical performance of zinc anode slurries is characterised in a single redox flow battery cell in discharge mode. Moreover, rheological behaviour of each of the slurries is investigated and key parameters underlying the cell performance are determined. A critical gelling agent concentration of 0.4 wt.% of PAA is found, where a maximum peak power density of 24 mW/cm^2 is obtained from polarization curves, improving previous reported performances using the same cell configuration. Combined rheological and electrochemical effects are analysed in which an optimum PAA concentration is found in which slurry stability is not compromised and conductivity is satisfactory. These results bring more understanding in the development of slurry-based RFBs.

Contents

5.1 Introduction

As current energy development aims towards technologies powered by renewable sources [Breyer et al., 2013], necessity of efficient energy storage systems has driven research to explore new materials and configurations. Redox flow batteries (RFBs hereinafter) have been gaining attention as their versatile and flexible operation is suitable to potentiate intermittent renewable energy sources like wind and solar energy. Their ability to decouple energy storage and power generation [Ye et al., 2019] improves electrical grid efficiency and power quality by allowing better resource management for peak shaving and valley filling.

Among different possible chemistries, zinc-air is one of the most interesting due to its high theoretical specific energy density of 1350 Wh/kg [Bockelmann et al., 2016] and zinc availability in Earth's crust. Zinc - air batteries have been commercialized since early 20th century [Mainar et al., 2018a], mostly as primary batteries. In a typical zinc-air battery, the electrochemical reactions proceeding in the cell are the following. For comparison, the half cell reactions are compared to the reference standard hydrogen electrode (SHE).

$$Cathode: \ O_2 + 2H_2O + 4e^- \underset{\text{charge}}{\overset{\text{discharge}}{\rightleftharpoons}} 4OH^- \quad (E^0 = 0.40 \ Vvs \ SHE) \tag{5.1}$$

$$\begin{aligned} Anode: \ Zn + 4OH^- - 2e^- &\underset{\text{charge}}{\overset{\text{discharge}}{\rightleftharpoons}} Zn(OH)_4^{2-} \\ (E^0 &= -1.25 \, V vs \, SHE) \\ Zn(OH)_4^{2-} &\rightarrow ZnO + H_2O + 2OH^- \end{aligned} \tag{5.2}$$

$$\begin{aligned} Cell \ reaction: 2Zn + O_2 &\underset{\text{charge}}{\overset{\text{discharge}}{\rightleftharpoons}} 2ZnO \\ (E^0 &= 1.65 \, V) \end{aligned} \tag{5.3}$$

Nevertheless, development as rechargeable batteries has been hindered due to different issues, largely, zinc anode limitations studied in depth by A. Mainar [Mainar et al., 2018a,b,c], and other authors [Banik et al., 2013, 2015; Liu et al., 2016; Schmid et al., 2017a,b; Yang et al., 2016; Yang et al., 2004]. In order to reduce zinc anode problems, metal-air batteries such as zinc - air, have been redesigned as flowing systems instead of static [Han et al., 2018].

In particular, zinc slurry - air flow battery is an interesting approach as zinc particles are dispersed in the same electrolyte media with the aid of gelling agents, enhancing electrode surface and energy density [Duduta et al., 2011; Huang et al., 2015]. Many of the advantages of having a flowable electrode comprise the reduction of dendrite formation [Jiang et al., 2018], and non-localized electrode shape change and passivation layers [Yang et al., 2004]. The flow of the slurry and charge transfer in single cell is optimized by using flow fields [Choi et al., 2020a], promoting uniform distribution over geometric area.

However, zinc microparticles are largely dense ($\rho_{Zn} = 7.11 \ g/cm^3$), and in order to increase active material utilization, they need to be homogeneously suspended in a percolated network [Wei et al., 2015]. Hence, rheology plays an important role in RFBs as network properties are important for slurry formulation. Moreover, electrochemical performance is directly linked to flow behaviour because mass transfer coefficients, ions diffusion and pump losses, among others, depend on electrolyte viscosity [Barton et al., 2018; Iyer et al., 2017; Tang et al., 2014].

Within this study, zinc slurry - air RFB is designed to work under highly alkaline conditions. Alkaline electrolytes are recurrently used in zinc-air batteries due to their high ionic conductivity and solubility of zinc species important in the redox reaction [R. Mainar et al., 2016]. Aqueous electrolytes are mixed with gelling agents and additives to prepare gel polymer electrolytes (GPEs). However, such a harsh alkaline environment(i.e. 10 M KOH used by N. Choi et al. for zinc slurry -air RFB [Choi et al., 2020b]), limits the availability of gelling agents that are able to suspend dense zinc particles, compromising slurry stability. Among

available gelling agents, Carbopol® 940 and attapulgite (Attagel® 50) were chosen to prepare zinc slurries.

Carbopol® 940, also known as polyacrylic acid (PAA) is used frequently as a model fluid in experiments together with numerical simulation because of its stability and well-known properties at near-neutral pH, where yield stress behaviour is enhanced (refer to [Piau, 2007] for extensive study in PAA elasto-visco-plastic behaviour). PAA has been already investigated as electrolyte additive for application in alkaline metal-air batteries like Al-air and Zn-air batteries. Z. Zhang et al. [Zhang et al., 2014] investigated PAA gel performance in a Al-air battery where its conductivity of 460 mS/cm was found to be close to that of aqueous electrolytes. Moreover, in the preparation of GPEs polyacrylic acid (PAA) used as gelling agent has been proved to show higher conductivity compared to other gelling agents like PVA and PAM at 6 M KOH [Tran et al., 2019].

Attapulgite is a type of magnesium aluminium silicate clay with a three-dimensional needle-like morphology [Shen et al., 2005] and chemical formula $3MgO - 1.5Al_2O_3 - 8SiO_2 - 9H_2O$. When dispersed at high shear rates, attapulgite is able to work as a gel-forming clay [Haden et al., 1967]. The shape and size of its needles, as well as its gelling mechanism, result in a good resistance to high concentrations of electrolytes [Abdo et al., 2013]. Under this latter conditions, yield stress is enhanced [Chang et al., 1993; Qian et al., 2018], making it a good candidate to prepare zinc slurries. Besides its rheology modifier properties, attapulgite also shows properties that enhance the electrochemical performance of zinc slurry-air batteries. Attapulgite has been previously investigated to formulate zinc slurries for automotive application and it was found that the addition of this clay reduces anode corrosion, even more when combined with ZnO [Sonneveld, 1991].

This study aims to assess the compositional effects of PAA gelling agent on slurry electrochemical and rheological properties in a custom-made zinc slurry - air RFB. The effect of PAA concentration on slurry electrochemical performance and stability is thoroughly investigated by electrochemical cell tests and rheological characterisation. Lastly, an optimal concentration of PAA is discussed in terms of the trade-of between performance and stability. This paper links material formulation in harsh alkaline environment with electrochemical experimentation and rheological characterisation, highlighting the importance of material formulation for RFBs. Furthermore, with the presented rheometric approach, it is possible to predict the formulation that will yield a maximum performance of such devices like RFBs by knowing particle and suspending fluids properties.

5.2 Materials and methods

5.2.1 Slurry preparation

In order to have reproducible results, a slurry preparation protocol is followed to produce each of the samples before either rheology or electrochemical characterisation. Slurry composition was taken from a previous study using the same experimental set-up [Choi et al., 2020a], except for gelling agents presented in here.

5.2.1.1 Gel polymer electrolytes (GPEs)

The preparation of GPEs is described in the previous Chapter 3. Formulation consist in aqueous electrolytes mixed with gelling agents. Table 5.1 shows the components and concentrations used to prepare the different GPEs used in this study.

Sample	KOH 10 M wt. %	PAA wt. %	Attapulgite wt. %	ZnO wt. %
GPE1	92.30	0.30	1.40	6.00
GPE2	92.15	0.45		
GPE3	92.00	0.60		
GPE4	91.85	0.75		
GPE5	91.70	0.90		

Table 5.1: Gel polymer electrolytes GPEs composition.

5.2.1.2 Zinc slurries

Zinc particles battery grade (GN 7-4/200Bi/200In, Grillo GmbH, Germany) were used as received and size characterisation is seen in figure 5.1.

Figure 5.1(a) shows a picture of zinc particles taken with a scanning electron microscopy (SEM, ZEISS GeminiSEM 500). It is seen that zinc particles show rounded shapes varying from particle to particle. Particle size was determined by means of laser diffraction (Mastersizer 2000, Malvern Panalytical), and it is shown in figure 5.1(b). Zinc particles yielded a monodisperse Gaussian distribution, with a mass-median-diameter $D_{50} = 76.4\mu m$ (with a $\sigma = 21.9\mu m$).

Once GPEs are prepared, zinc slurries are prepared in the following way. Zinc particles are added into freshly prepared GPEs. Particles are first dispersed using a spatula to avoid lumps and then slurries are homogenized with Ultra Turrax at 11 000 rpm for 1 minute. This preparation ensures homogeneous distribution of zinc particles in the suspending fluid. Higher

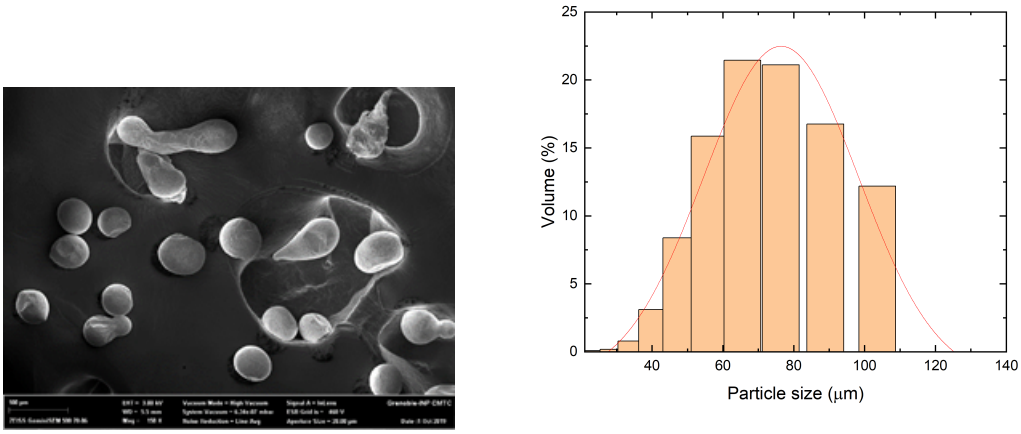

(a) (b)

Figure 5.1: Zinc particles battery grade size and shape characterisation. a) SEM picture of zinc particles. b) Zinc particles size distribution obtained by laser diffraction distribution (Mastersizer 2000).

rotational speeds and longer times were not pursued because high mechanical action can damage or disintegrate PAA polymer chains [Xiong et al., 2020], reducing sample yield stress. After preparation, samples were ready for either electrochemical or rheological characterisation. The final slurry concentrations can be found in table 5.2.

Sample	KOH 10 M wt. %	PAA wt. %	Attapulgite wt. %	ZnO wt. %	Zn wt. %
S1	61.10	0.20	0.9	4.0	33.8
S2	61.00	0.30			
S3	60.90	0.40			
S4	60.80	0.50			
S5	60.70	0.60			

Table 5.2: Zinc slurries composition.

Each slurry S_i in table 5.2 was prepared with corresponding KOH, PAA, attapulgite and ZnO concentrations as for GPE_i (table 5.1). For example, S1 was prepared by adding 33.8 wt. % of zinc particles to GPE1.

PAA concentrations higher than 0.6 wt. % were not investigated because of their final high apparent viscosity, which in practice made it impossible to flow samples through the RFB cell.

5.2.2 Electrochemical characterisation

Electrochemical tests were performed using a home-made single cell presented in a previous study [Choi et al., 2020a] to determine performances of zinc slurries in a zinc slurry - air RFB.

The configuration used for this study contained a graphite bipolar plate, flow frame flow field, separator, gaskets and current collectors, correctly fixed by the aid of two end plates, as it is depicted in the diagram in figure 5.2.

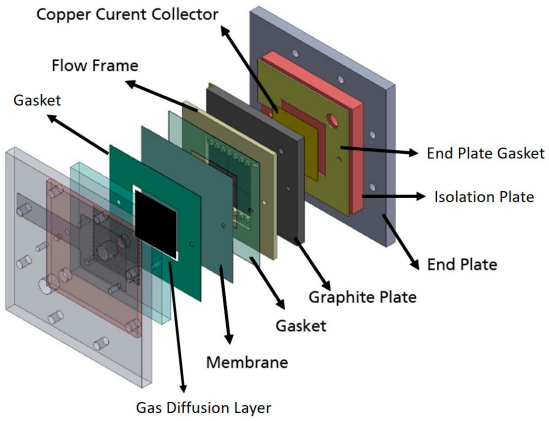

Figure 5.2: Diagram of single cell zinc slurry - air RFB reprinted from [Choi et al., 2020a].

Zinc slurry and synthetic air were pumped in the anode and cathode compartments with a flow rate of 160 mL/min and 100 mL/min, respectively. During cell testing, current-voltage characteristic curves were obtained by using a BaSyTec GSM Battery Test System (BaSyTec GmbH, Germany). When anode and cathode are flowing through the battery, constant current is applied and steady state voltage is obtained, as observed in figure 5.3:

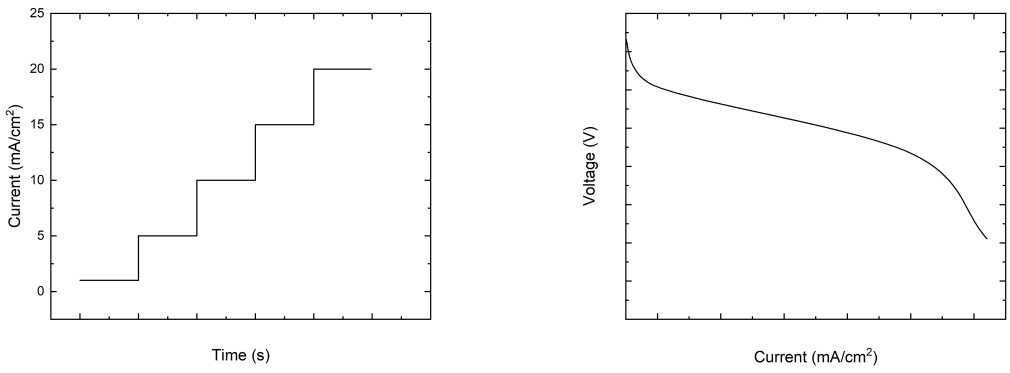

(a) (b)

Figure 5.3: Protocol to obtain polarization curves from cell testing. a) Protocol to obtain polarization curves. b) Expected voltage response to protocol in figure 5.3(a).

Finally, slurries conductivity was obtained by electrochemical impedance spectroscopy (EIS) using a response analyser (Hewlett Packard, United States) at 20 $°C$.

5.2.3 Zinc sedimentation in slurries

Zinc particle sedimentation in slurries is critical for RFB application and for rheological characterisation. If sedimentation takes place in the battery, zinc will settle in the bottom leading to clogging and/or lower battery performances due to less particles utilization. Correspondingly, if sedimentation takes place during rheological characterisation, initial sample properties will change during test, as sedimentation is in competition with deformation. Therefore, slurries sedimentation time is a critical factor as it can interfere in sample characterisation.

Sedimentation kinetics of recently prepared slurry samples were determined by tracking particle position over time, as shown in figure 5.4(a). Slurries were placed in a rectangular cell of width 4.5 mm and depth 10 mm. Pictures of slurries over time were recorded using a digital camera (Xiaomi Yi Cam, China) and were analyzed using ImageJ software. ImageJ can process images in grayscale and motion can be tracked after defining a pixel/distance ratio.

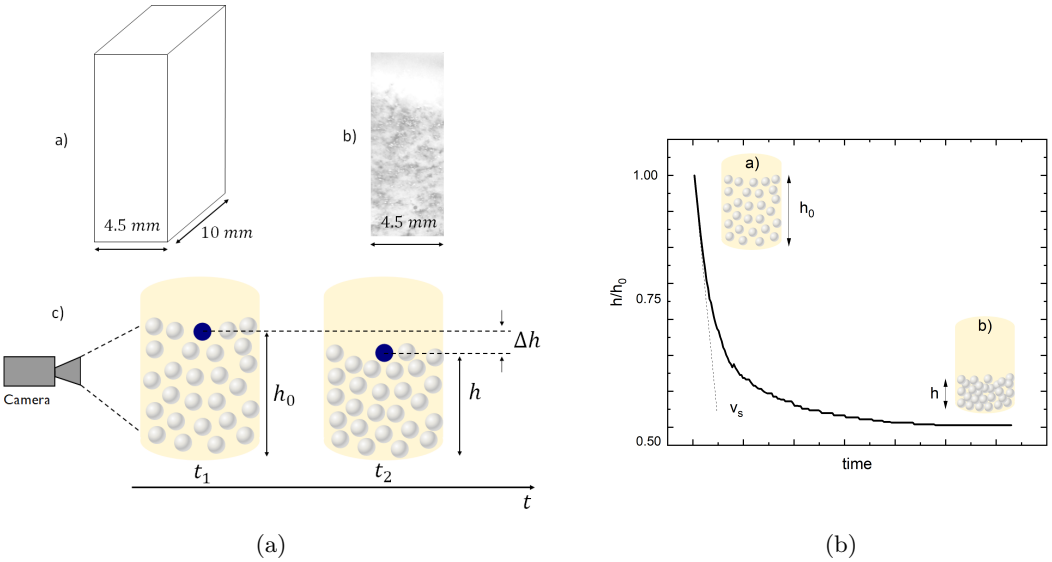

(a) (b)

Figure 5.4: Protocol to obtain sedimentation profiles. a) Sedimentation experiment set-up. a) Visualization cell used to record sedimentation. b) Picture of slurry in the visualization zone. c) Particle settling Δh happening between two different given times. Figure 4b) Expected sedimentation profile as function of original sample particles height h_0. Inset a) shows the sample at the beginning of the test. Inset b) shows sample after sedimentation. v_s is the sedimentation velocity obtained from the slope of the sedimentation profile in the linear region.

In figure 5.4(b) it is possible to observe the expected sedimentation profile for any given slurry undergoing sedimentation. Ratio h/h_0 is plotted against time. The more the sample undergoes sedimentation, the lower is the value of the ratio h/h_0. Sedimentation velocity v_s can be determined from the slope of the linear decrease at the beginning of the test, as observed in figure 5.4(b). Furthermore, it can be determined the time at which sample has undergone sedimentation at different percentages defined by the ratio loss. We define in this study a

critical sedimentation threshold of 5 %, equivalent to a ratio $h/h_0 = 0.95$. Beyond 5 % of sedimentation, sample cannot be characterised as its properties would have already changed from its initial state. Therefore, rheometric characterisation was set so the experiment time will be shorter than the time a given sample shows 5 % sedimentation.

5.2.4 Rheometry

Zinc slurries rheological behaviour was studied using a stress-controlled rheometer AR-G2 (TA instruments, United States) and a vane-in-cup geometry. Vane geometry (4-blades, blade width = 24 mm, h = 45.5 mm), was specially designed to study slurries in this study ensuring an homogeneous shearing avoiding slippage and ejection [Hermoso et al., 2012; Hreiz et al., 2017]. A scheme of the set-up can be observed in figure 5.5. In addition, it is observed that transparent cup (D = 48 mm) is equipped with a grid (thickness = 2 mm), in order to eliminate slippage effects [Owens et al., 2020], as shown in figure 5.5(b).

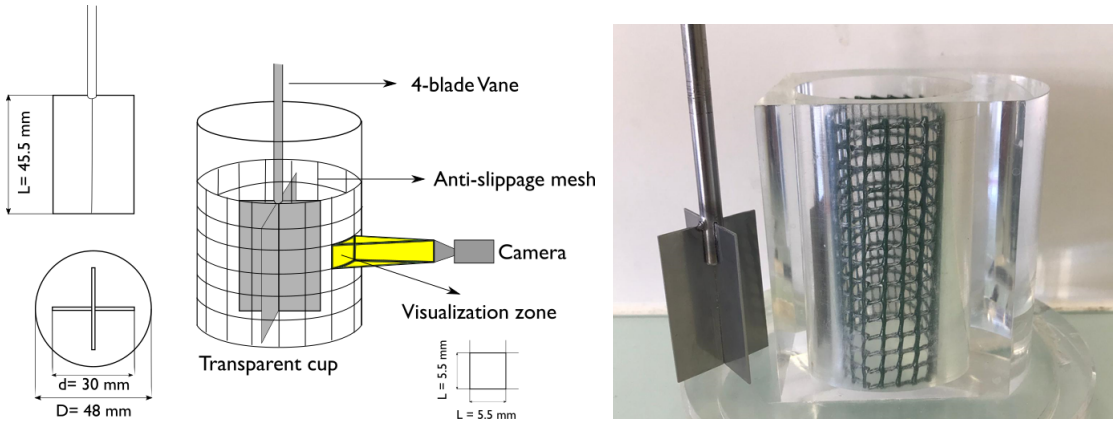

(a) (b)

Figure 5.5: Vane-in-cup equipped with grid to perform sample rheological characterisation. a) Scheme of Vane-in-cup and set up used for GPEs and slurries. b) Picture of actual set-up.

Moreover, vane tool generates a flow profile in a Couette that is similar to the one generated by concentric cylinders geometry [Baravian et al., 2002]. A calibration was performed to determine geometrical factors allowing sample rheological characterisation. These factors permit to translate rotational speed and torque obtained with vane-in-cup, into shear rate and shear stress, respectively. Using a Couette analogy approach [Aït-kadi et al., 2002], geometrical factors are calculated as follows:

$$K_{\dot{\gamma}} = \frac{\dot{\gamma}}{\dot{\theta}} = \frac{2}{n} \frac{\left(\frac{R_e}{r^*}\right)^{\frac{2}{n}}}{\left(\frac{R_e}{R_i}\right)^{\frac{2}{n}} - 1} \tag{5.4}$$

$$K_{\tau} = \frac{\tau}{\Gamma} = \frac{1}{2\pi r^{*2} h}$$

Where R_i is radius corresponding to the analogous inner cylinder, R_e is the cup radius, h is the height of the vane, n is the flow index of the calibration fluid and r^* is the radial position at which sample can be characterised independently of flow index n.

Finally, factors calculated with vane and cup dimensions are $K_{\dot{\gamma}} = 2.30\ rad^{-1}$ and $K_{\tau} = 13450.7\ Pa\ N^{-1}\ m^{-1}$, corresponding to an analogous inner cylinder of diameter d = 26 mm. Complete calculation of geometrical factors can be found in [Chapter 3].

5.2.4.1 Oscillatory rheometry

Small deformation rheometry was used to characterise slurries viscoelastic properties representative of samples close to rest. These tests allow us to assess slurry properties when battery is not under operation (no flow). Oscillatory rheometry consists in applying a sinusoidal deformation $\gamma(t) = \gamma_0 sin(\omega t)$, with γ_0 as the oscillation amplitude and ω as the angular frequency. In each test, storage and loss moduli (G' and G'' respectively), are recorded as function of deformation or frequency. Slurries linear deformation domain (LVR), in which viscoelastic properties are independent of deformation, was determined by performing a strain amplitude sweep from 0.1 to 1000 % at 1 Hz.

Viscoelastic behaviour representative of sample linear behaviour were obtained by applying a frequency sweep from 0.1 to 4 Hz at a deformation located in samples LVR. These deformations were 0.1 % for S1 and 1 % for all the other slurries (S2-S5).

5.2.4.2 Large deformation rheometry

Slurry flow curves were obtained by large deformation tests. Large deformation tests are important to understand how slurries will behave while pumping in a RFB. Steady shear rheometry was performed by decreasing shear rate steps in which the stress response is measured. As

explained in Chapter 3, just decreasing shearing steps are taken into account in order to avoid heterogeneous shearing zones [Ovarlez et al., 2013]. Shear rate was decreased from 100 to 0.01 s^{-1}.

5.3 Results

5.3.1 Electrochemical discharge performance

Electrochemical performance is evaluated by determining polarization curves for each formulated slurry in a zinc slurry – air RFB single cell. Results are shown in figure 5.6, where the variation of voltage and power density as a function of current density is represented for each slurry.

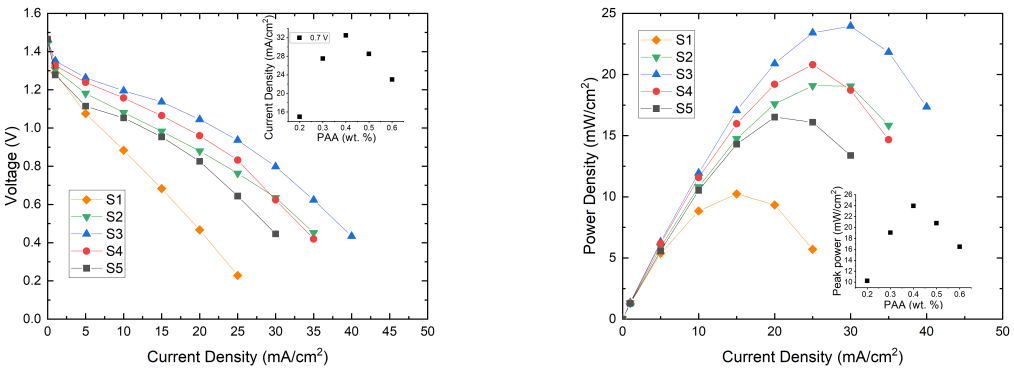

(a) (b)

Figure 5.6: Zinc slurries polarization curves. a) Voltage as function of current density. b) Power density as function of current density.

Figure 5.6 reveals the effect of PAA concentration used in slurry formulation on cell electrochemical performance. Current-voltage characteristic curve (figure 5.6(a)), records the cell voltage at an imposed current. It is observed that cell voltage drops at different rates for different PAA concentrations as current density is increased. Moreover, S3 reaches the higher current density values before reaching voltage cut-off.

To compare all slurries under the same conditions, current density values at a constant voltage of 0.7 V are represented as function of PAA concentration in the inset of figure 5.6(a). This voltage is representative for zinc-air batteries as it has been shown that cycling stability and energy efficiency is optimal at 0.7 V [Li et al., 2013]. It is observed that current density increases from 15 to 32.5 mA/cm^2 as PAA concentration increases from 0.2 to 0.4 wt. %. Contrarily, when PAA concentration is increased further than 0.4 wt. % up to 0.6 wt. %,

current density decreases to a value of 23 mA/cm^2. S3 out-stands among the different slurries by showing the highest current density at 0.7 V.

In an equivalent representation, figure 5.6(b) analyses power density as a function of current density for each of the slurries. As current density increases, power density increases up to a maximum point before decreasing and forming a parabola. The maximum point is known as peak power density, and it is depicted as function of PAA concentration in the inset of figure 5.6(b). It is observed that peak power density increases from 10 to 24 mW/cm^2 as PAA concentration increases from 0.2 to 0.4 wt. %. When concentration of PAA in increased in slurry formulation, peak power density decreases to a value of 16.5 mW/cm^2 for a PAA concentration of 0.6 wt. %. These results suggest that concentration of 0.4 wt. % corresponding to S3 is close to a limit between two behaviours, one that favours battery performance and another that decreases its performance.

To broaden our understanding of slurries electrochemical properties, slurries ionic conductivity was measured by EIS. Figure 5.7 represents ionic conductivity as function of PAA concentration.

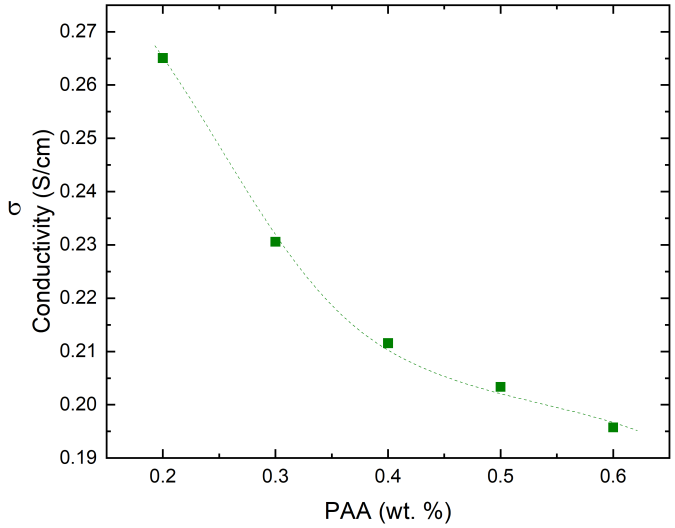

Figure 5.7: Slurries conductivity as function of PAA concentration 20 $°C$.

As PAA concentration increases, conductivity decreases following a quadratic behaviour $\sigma = 0.46 \cdot (PAA)^2 - 0.53 \cdot PAA + 0.35$ $(R^2 = 0.99)$, where σ is the slurry ionic conductivity and PAA is the concentration of PAA in wt. %. It is observed that when PAA concentration is increased from 0.2 to 0.4 wt. % in slurries, the conductivity dependence is stronger than when increasing the concentration from 0.4 to 0.6 wt. %. When increasing PAA concentration, a viscosity increase is imminent, as it will be presented in a following section (section 5.3.3.2).

Even if slurries can benefit from an increase in viscosity to slow down sedimentation kinetics, electrochemical activity can be reduced. W. Yuan et. al [Yuan et al., 2018], indicated that generally, higher viscosities lead to lower conductivities in aqueous electrolytes.

Results presented in this section illustrate that there is a critical PAA concentration in the range of concentrations studied. Moreover, higher concentrations of gelling agent reduce slurry ionic conductivity. To investigate why slurry peak power density and voltage (figure 5.6), are enhanced at 0.4 wt. % PAA, corresponding to S3 formulation, rheological characterisation needs to be performed. Nevertheless, sedimentation tests are performed to study PAA effect on sedimentation kinetics, but also allowing to know for how long slurries are stable in order to be characterised.

5.3.2 Zinc sedimentation

Sedimentation tests were performed tracking zinc particle position in zinc slurries and results are shown in figure 5.8.

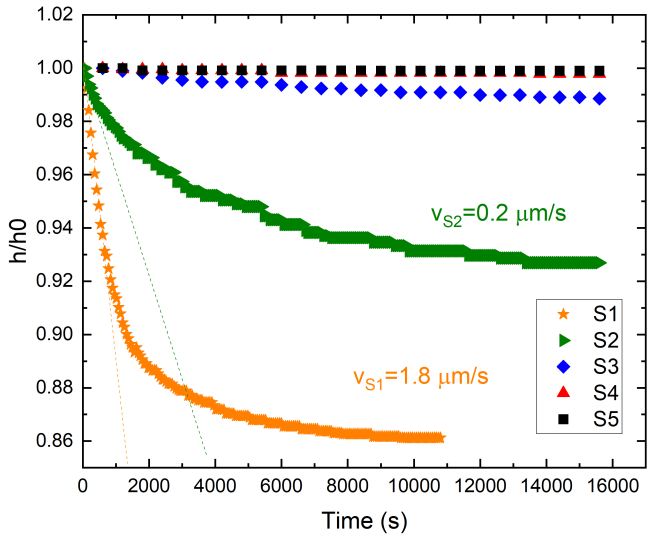

Figure 5.8: Slurries sedimentation kinetics at 20 $^{\circ}C$.

The ratio between the recorded height and the initial height as a function of time is represented in figure 5.8 for each slurry. Results revealed that different sedimentation kinetics are found depending on PAA concentration used to prepare slurries.

S1 shows the fastest h/h_0 ratio decrease at times $t < 2000\ s$. Sedimentation velocity v_s is calculated from the linear height h decrease and it is found to be $v_{s1} = 1.8\mu m/s$. Then h stabilizes slowly until reaching a plateau at $\approx$ 10 000 s (2.78 hours). For S2, h/h_0 ratio

	S1	S2	S3	S4	S5
Sedimentation	Time [s]				
5 %	420	3240	-	-	-
7 %	660	8760	-	-	-
10 %	1200	-	-	-	-
14 %	9600	-	-	-	-

Table 5.3: Characteristic sedimentation times for S1 and S2 at 20 $°C$. S3, S4 and S5 do not show a sedimentation loss equal or higher than 5 % in 200 000 s ($\approx$ 55 h).

decreases slowly compared to S1. The sedimentation velocity is found to be $v_{s2} = 0.2\mu m/s$, which is 9 times slower compared to S1. Finally, S2 sedimentation finishes after 15 000 s (4.17 hours).

Contrastingly, samples S3, S4 and S5 remained homogeneous for longer periods and no significant sedimentation (h/h_0 lower than 2%) was observed in 55 h. In table 5.3, it is reported the time in which each of the slurries undergo sedimentation up to a given percentage of h/h_0 loss.

It is observed that slurry S1 shows a settling of 5 % at a time of 420 s, whereas S2 reaches this threshold at 3240 s, almost 8 times longer. Finally, S3, S4 and S5 remain stable (less than 2 % of sedimentation) in the timespan analysed. Finally, sample height stabilizes at a h/h_0 loss of 14 % for S1 and 7 % for S2, respectively.

Rheological characterisation presented in following section was performed so the time of each experiment was shorter than the time to reach 5 % of sedimentation.

5.3.3 Rheological characterisation

5.3.3.1 Oscillatory rheometry

Slurries viscoelastic properties obtained by oscillatory rheology are depicted in figure 5.9. These small deformation experiments are representative of sample properties at rest. It is important to understand slurries behaviour and network properties when RFB is not under operation.

Results of amplitude strain sweep are observed in figure 5.9(a). It is observed that as oscillation strain develops, storage G' and loss G'' moduli first form a plateau indicating the linear domain LVR. As PAA concentration increases, it is possible to observe that this domain is present for all slurries at different extents. For S1, LVR ends at a strain of 0.4 %. For S2 and S3, LVR is larger and reaches up to 1.6 % strain. Finally S4 and S5 shows a LVR up to 4 % strain. In the LVR is observed that $G' >> G''$ for all slurries.

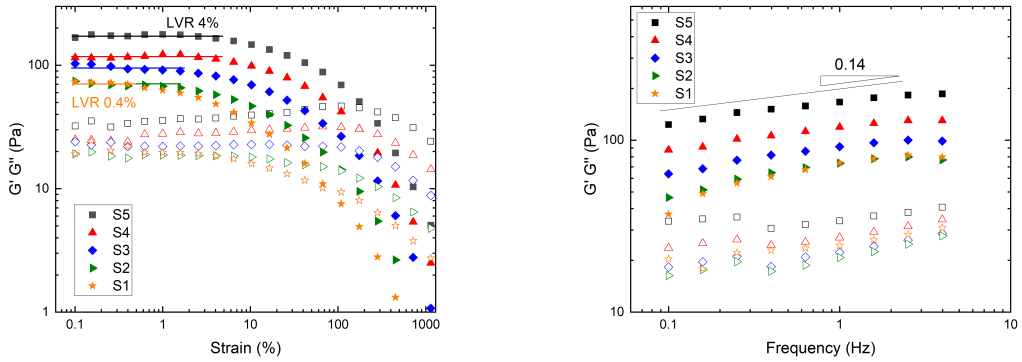

(a) (b)

Figure 5.9: Slurry oscillatory rheometry. a) Log-log plot of G' and G'' as function of strain amplitude at 1 Hz, 20 $°C$. Solid symbols represent storage modulus G' and open symbols represent loss modulus G''. b) Log-log plot of G' and G'' as function of frequency at a deformation located in slurries LVR, at 20 $°C$. Solid symbols represent storage modulus G' and open symbols represent loss modulus G''.

When amplitude strain continues to increase, a crossover point is met where $G' = G''$ and indicates the transition point from elastic solid to viscous liquid behaviour. As deformation continues to increase beyond crossover point, G'' becomes greater than G', indicating that sample initial network is being deformed indefinitely. In this non-linear region, moduli are strongly dependent of deformation and sample is under conditions similar to flow.

Same behaviour is observed for all slurries but as PAA concentration decreases, moduli values decrease as well, being S1 the slurry with lowest G' and G" values.

Furthermore, as observed in figure 5.9(b), for all slurries G' is greater than G'' in the range of frequency tested from 0.1 to 4 Hz. Moreover, modulus G' is parallel to G'' and they show a slight dependence to frequency as moduli values increase with frequency with an average slope of 0.14. Moreover, there is not a moduli crossover in the range of frequencies analysed.

The effect of PAA is also observed in figure 5.9(b). As PAA concentration increases from S1 to S5, moduli values increase accordingly, with S5 showing the highest moduli values and S1 the lowest moduli values, respectively.

Therefore, this viscoelastic behaviour observed for zinc slurries suggest that slurries show properties characteristic of gel-like materials. This is very important as zinc particles form part of a gelled network in a zinc slurry - air RFB.

5.3.3.2 Zinc slurries flow curves

To understand slurries behaviour representative of flow, flow curves are obtained by shearing tests. Steady state shear stress as function of shear rate for each slurry is presented in figure 5.10.

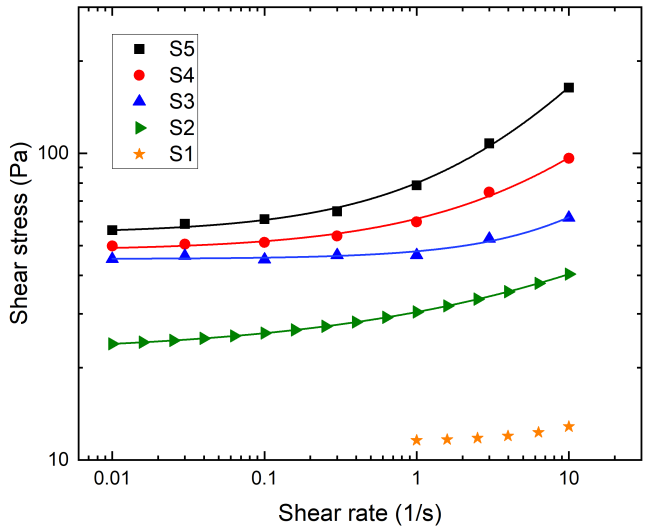

Figure 5.10: Shear stress as function of shear rate for zinc slurries at 20 $°C$. Solid lines represent Herschel-Bulkley fitting. Table 5.11(b) shows the fitting parameters for each slurry.

In figure 5.10, shear stress as function of shear rate is observed for all slurries. It is worth to mention again that flow curves were obtained by down-ramping shear rate. Moreover, rod climbing (also known like Weissenberg effect [Weissenberg, 1947]), was observed at shear rates $> 10\ s^{-1}$ (video, `https://rb.gy/mqstib`), where no steady state was found, as observed in our previous study with gel polymer electrolytes [Chapter 3]. Results presented in this study are obtained for a range of shear rates comprised between 0.01 and 10 s^{-1}.

S1 was analyzed at shear rates from 1 to 10 s^{-1} and it is observed that shear stress increases slightly with shear rate. Lower shear rates lead to sedimentation and two phases system where no steady state was found, even if the large deformation experiment was shorter than the sedimentation time (420 s for S1 to reach 5 % of sedimentation, table 5.3). An explanation to this faster sedimentation may lay on the protocol used to obtain the flow curves. As shear rate is decreased, slurry viscosity decreases from the beginning of the test. In the fluidized slurry state, yield stress is absent and gelled network cannot make opposition to zinc particles to settle towards the bottom of the cup. This sedimentation process has also been observed by other researchers dealing with suspensions [Ovarlez et al., 2010; Ovarlez et al., 2011; Owens et al., 2020].

Next, S2 shows higher shear stress values as PAA concentration is increased, and sedimentation was not observed during the test. As shear rate increases from 0.01 to 10 s^{-1}, shear stress continuously increases. However, a different behaviour is observed for S3, which was prepared with 0.4 wt. % of PAA. S3 shows that as shear rate is increased, shear stress remains first constant at shear rates $< 1\ s^{-1}$ and then shear stress increases as shear rate increases. S4 and S5 show similar behaviour compared to S3: a shear stress plateau up to a shear stress of 0.1 s^{-1}, and then shear stress increases as shear rate is increased.

Overall, slurries analysed in here show a behaviour corresponding to yield stress fluids, except for S1. This rheological behaviour is sought because yield stress will help to maintain zinc particles in suspension and provide a percolated network providing enhanced conductivity. In addition, shear-thinning behaviour is also observed, decreasing viscosity as shear rate is increased. Viscosity decrease is very important to ease pumping of slurry throughout a RFB.

To quantify rheological parameters, shear stress vs shear rates curves were fitted to a Herschel-Bulkley model:

$$\tau = \tau_y + K\dot{\gamma}^n \tag{5.5}$$

Where τ is the shear stress, τ_y is the yield stress, K is the consistency index, $\dot{\gamma}$ is the shear rate and n is the flow index. Fitting results are shown in table 5.11(b). In the case of S1, as there are values just few values in one shear rate decade, no fitting was done. Instead, the shear stress at the lowest shear rate is represented together with the yield stress of other slurries.

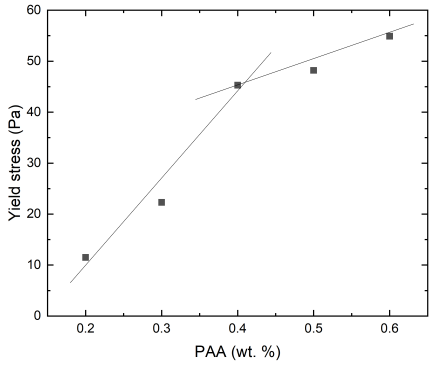

(a)

Sample	PAA $[wt.\%]$	τ_y $[Pa]$	K $[Pa \cdot s^n]$	n $[-]$	R^2
S1*	0.20	11.6	-	-	-
S2	0.30	22.3	8.10	0.35	0.99
S3	0.40	45.3	2.67	0.80	0.98
S4	0.50	48.2	13.00	0.57	0.99
S5	0.60	54.9	25.21	0.64	0.99

(b)

Figure 5.11: Slurries yield stress. * As there are few points for S1, a yield stress is not considered but just the shear stress measured at the lowest shear rate in figure 5.10 is considered. a) Yield stress as function of PAA concentration for slurries. b) Herschel-Bulkley fitting parameters for zinc slurries obtained from equation 5.5.

In figure 5.11(a) it is observed that yield stress increases by a factor of 4 from 11.6 to 45.3 Pa as PAA concentration is increased from 0.2 to 0.4 wt.%. When PAA concentration is further increased up to 0.6 wt.%, the increase in yield stress is weaker compared to the other slurries. Yield stress for S4 and S5 are 48.2 and 54.9 Pa, respectively.

Herschel-Bulkley parameters can be found in table 5.11(b). It is observed that shear thinning behaviour is found by the model as flow index $n < 1$. Furthermore, consistency index K was found to increase with increasing PAA concentration.

Finally, it is observed that concentration of 0.4 wt. % is close to a critical concentration from which a yield stress behaviour is very well defined in comparison with the slurries prepared with concentrations lower to 0.4 wt. %. Discussion comparing both electrochemical and rheological results is found in next section.

5.4 Discussion

As seen across electrochemical and rheological characterisation, PAA concentration plays an important role in the formulation of zinc slurries for RFB.

From electrochemical characterisation, polarization curves (figures 5.6), it is observed that slurry performance is enhanced when PAA concentration increases from S1 to S3, reaching a concentration of 0.4 wt.% of PAA. At this concentration, slurry performance is maximized reaching a current density of 32.5 mA/cm^2 at 0.7 V and a peak power density of 24 mW/cm^2. Contrastingly, when PAA concentration is further increased up to 0.6 wt. % (corresponding to S5), single cell performance decreases, as observed in the insets of figure 5.6.

These results show not only that there is a critical PAA concentration where electrochemical performance during discharge is maximized, but also that S3 formulation improves the performance of a zinc slurry - air RFB compared to a previous study. N. Choi et al. [Choi et al., 2020b], reported a current density value of 15 mA/cm^2 at 0.7 V and 10 mW/cm^2 using the same set-up as the one used in this study (flow frame geometry for anode side), but a different zinc slurry formulation without attapulgite. From this comparison, electrochemical performance was improved by a factor of ≈ 2.4 in terms of peak power density, by using S3 as zinc anode slurry.

In order to understand how formulation can affect the performance of a zinc slurry - air RFB, rheological characterisation at small and large deformation was performed. Oscillatory rheology results represented viscoelastic properties of slurries at rest. It was found from frequency sweep (figure 5.9(b)), that all slurries behaved as elastic-solids. Indeed, G' was found to be greater

than G'' and independent of frequency, in the range of frequencies tested. Therefore, this viscoealstic behaviour suggests that there is a percolated network consisting mainly in the gel suspending fluid where zinc particles are dispersed, as Wei et al. observed for slurry RFBs [Wei et al., 2015]. Gel behaviour is important at rest because there is a mechanical resistance coming from the network that will prevent particles from settling. Nevertheless, it is crucial to assess if network strength is adequate to prevent zinc particles from settling when no flow is imposed.

Certainly, yield stress suggests that there is a percolated network in the slurries that prevents zinc particles from settling. Nonetheless, the gelled network used in slurry has to possess a minimum yield stress to maintain zinc particles in suspension. This minimum yield stress will depend on zinc particles characteristics and it is calculated as follows.

5.4.1 Minimum required yield stress τ_y

Slurries are prepared by using dense zinc particles prone to settling in aqueous medium. Knowing zinc particles size distribution (figure 5.1(b)), it is possible to determine the gel strength necessary to maintain a single particle in suspension. This is done by the equilibrium of forces acting on a zinc particle, as observed in figure 5.12.

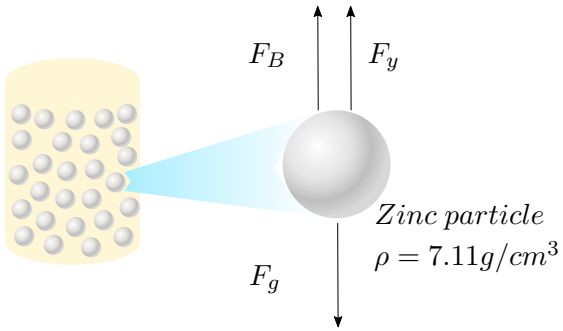

Figure 5.12: Forces acting on a single zinc particle suspended in a GPE. B, y and g stand for buoyancy, gel strength and gravity force, respectively.

As observed in figure 5.12, a single zinc particle ($D_{50} = 76.4\ \mu m$, $\rho = 7.13\ g/cm^3$), is under the action of gravity force F_g, buoyancy force F_B and gel strength F_y. F_g drags the particles towards the bottom of a container following gravity action. F_B is the fluid force opposing to particle weight. Finally, F_y is the force corresponding to the gelled network and it will representative of its suspending ability.

Furthermore, F_B and F_g can be expressed in terms of ρ density, g gravity constant and V volume:

$$\begin{aligned} F_B &= \rho_{fluid} \cdot g \cdot V_{particle} \\ F_g &= m \cdot g = \rho_{particle} \cdot g \cdot V_{particle} \end{aligned} \tag{5.6}$$

If we assume that a single particle like the one in figure 5.12 is in equilibrium, it is possible to write the following equation:

$$F_y + F_B - F_g = 0 \tag{5.7}$$

By substituting equations (5.6) into (5.7), we obtain:

$$F_y = V_{particle} \cdot g \cdot (\rho_{particle} - \rho_{gel}) \tag{5.8}$$

It is assumed that zinc particles are spherical, so the volume is equal to $V_{particle} = \frac{4}{3}\pi r^3_{particle}$. Knowing that stress can be expressed as $\tau = F/A$, where A is the contact particle area ($A = \pi r^2_{particle}$), it is possible to calculate the stress needed to maintain single particle in suspension. This stress will be analogous to yield stress:

$$\tau_y = \frac{4}{3}\pi r_{particle} \cdot g \cdot (\rho_{particle} - \rho_{gel}) \tag{5.9}$$

By substituting in equation (5.9) the values of radius ($r = 38.2\ \mu m$, figure 5.1), density corresponding to zinc particles ($\rho_{Zn} = 7.11\ g/cm^3$) and the density of the suspending fluid ($\rho_{GPE} = 1.40\ g/cm^3$, obtained from Microviscometer Lovis 2000 DMA density meter), a yield stress value $\tau_{yZn} = 2.85\ Pa$ is obtained. In order to maintain a single zinc particle in suspension, GPE yield stress value should be larger than τ_{yZn}.

In the next subsection, we analyze shortly rheological behaviour of GPEs, notably their suspending ability through yield stress.

5.4.2 GPEs as suspending fluids

Rheology of GPEs was analysed in a previous work [Chapter 3] and yield stresses τ_y were determined for each of the suspending fluids. Shear stress as function of shear rate curves were fitted to Herschel-Bulkley model (equation 5.5) for each GPE. Yield stress values and fitting parameters are displayed in figure 5.13 for each GPE.

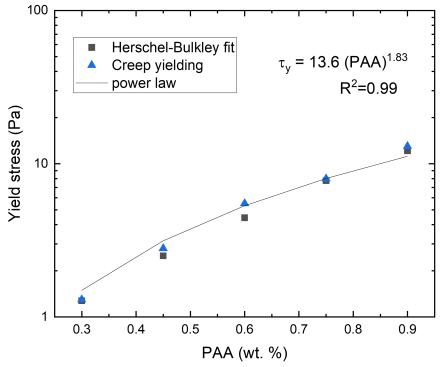

(a)

Sample	PAA [wt. %]	τ_y [Pa]	K [Pa $\cdot s^n$]	n [-]	R^2
GPE1	0.2	1.28	1.1	0.60	0.99
GPE2	0.3	2.51	5.1	0.63	
GPE3	0.4	4.44	9.6	0.62	
GPE4	0.5	7.75	20.3	0.61	
GPE5	0.6	12.15	38.6	0.59	

(b)

Figure 5.13: GPEs yield stress from [Chapter 3]. a) Yield stress as function of PAA concentration for GPEs. b)Herschel-Bulkley parameters obtained from fitting with equation (5.5).

In table 5.13(b), each of the GPEs correspond to the slurries with the same number (i.e. GPE5 is the suspending fluid of S5). As expected, it is observed that when PAA increases, yield stress value increases as well. Complete rheological characterisation and discussion can be found in our previous work [Chapter 3].

As previously described, there is a condition to comply to maintain zinc particles in suspension, being that gelled network yield stress ought to be greater than minimum yield stress to suspend zinc particles ($\tau_y > \tau_{yZn} = 2.85\ Pa$). It is observed in table 5.13(b), that only three of the GPEs comply with this condition, being GPE3, GPE4 and GPE5. In other words, slurries prepared with at least 0.4 wt. % of PAA, corresponding to S3, will remain homogenously suspended for longer durations (no significant sedimentation observed in 55 h).

Consequently, it is with no surprise that electrochemical and rheological behaviours are different when analyzing samples prone to sedimentation. Moreover, results obtained during sedimentation experiments (figure 5.8), confirm that S1 and S2 exhibited sedimentation profiles, whereas S3, S4 and S5, prepared with GPEs with $\tau_y \geqslant 2.85\ Pa$ are stable for the whole extent of the experiment.

Therefore, when minimum yield stress to suspend zinc particles is met by increasing PAA concentration up to 0.4 wt. % corresponding to S3, electrochemical performance is enhanced (figure 5.6). Nevertheless, when PAA concentration is further increased, electrochemical performance is not improved. This is also reflected in figure 5.7, where conductivity decreases as PAA concentration increases. As discussed by K. Smith et al. [Smith et al., 2014], an optimal yield stress value must exists, as mechanical energy dissipation and ion mobility depends on the viscosity of the system. Similarly, Z. Zhang et al. [Zhang et al., 2014] not only demonstrated that an optimal conductivity of PAA-based alkaline gels was attained at a specific PAA

concentration, but also further increase in gelling concentration led to lower conductivities.

Moreover, slurry rheological properties are also influenced by sedimentation kinetics. For instance, in figure 5.10, it is possible to discern between two behaviours. At PAA concentrations higher than 0.4 wt. % in slurries, it is possible to observe a stress plateau corresponding when $\dot{\gamma} \rightarrow 0$, corresponding to a yield stress. Contrastingly, S1 and S2 show significantly lower stresses and even more, S1 is hardly characterised due to sedimentation effects.

Finally, zinc slurries key rheological and electrochemical properties evaluated in this study are summarized in figure 5.14.

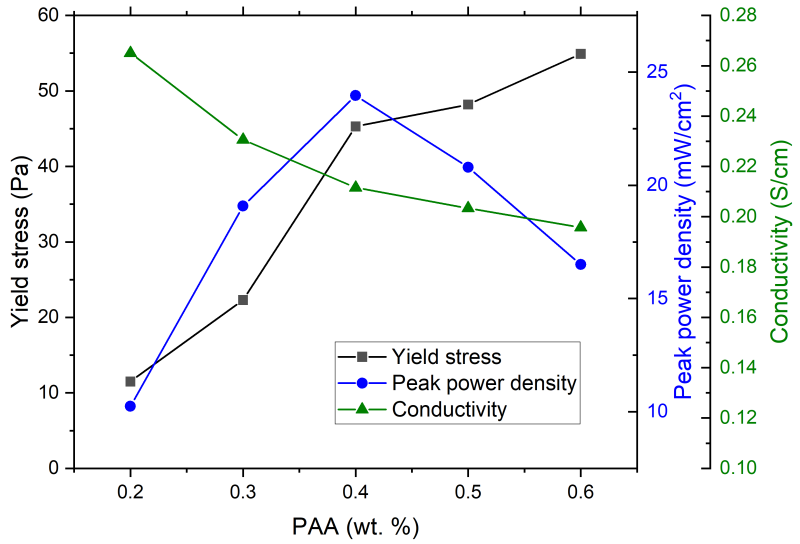

Figure 5.14: Yield stress, peak power density and ionic conductivity as function of PAA concentration.

In figure 5.14, it is possible to observe the combined effects of yield stress and conductivity on the performance of the single RFB cell. As PAA concentration increases in slurries, peak power density increases steadily together with yield stress up to a concentration of 0.4 wt. %. At this PAA concentration, maximum peak power density is reached and suspending fluid (GPE3), possess a yield stress large enough to avoid zinc particles sedimentation. Hence, it is then close to this PAA critical concentration where there should be an optimum concentration in which power peak density can be maximized, meaning that there is not PAA in excess and network properties are able to suspend zinc particles homogeneously.

Consequently, once this optimum concentration is exceeded, peak power density decreases even if more PAA in the formulation leads to more stable slurries in terms of sedimentation. This can be explained by the fact that PAA does not enhance conductivity and the additional viscosity increase has a negative effect on ion mobility as explained in section 5.3.1. Hence,

at PAA > 0.4 wt. %, peak power density decreases together with conductivity, whereas yield stress increases weakly. In like manner, J. Barton et al. [Barton et al., 2018] and J. Milshtein et al. [Milshtein et al., 2017], found that flow batteries using high viscosity electrolytes were correlated to low mass transfer rates, decreasing RFB performance.

5.5 Conclusions and Perspectives

As seen in electrochemical results, as PAA concentration increases, a critical concentration is found where peak power density is maximized during the discharge of a zinc slurry - air RFB. This critical concentration was found to be 0.4 wt. % of PAA in slurries, corresponding to S3. Moreover, it was found by rheometrical means that this critical concentration is needed to have a yield stress $\tau_{yZn} > 2.85\ Pa$ in order to maintain zinc particles in suspensions. This result was also reflected on sedimentation tests in figure 5.8, where S1 and S2 sediments as gelled network is not strong enough to maintain zinc particles homogeneously suspended.

Hence, rheology is found to be a useful tool to characterise slurries and understand key rheological parameters affecting discharge performance of a zinc slurry - air RFB. Yield stress shows to be not only important as stability enhancer but also as a parameter favouring the performance of a network formed by a gel and zinc particles. Furthermore, we present here that just by knowing the size and density of the particles to be suspended, it is possible to know the yield stress needed to be closer to maximum electrochemical performance.

This study is a first insight on the electrochemical performance of a zinc microparticles slurry-based RFB observed from a rheological point of view. More research efforts are needed in order to evaluate pressure losses when pumping slurries through the cell. Finally, on-line visualization experiments are needed to understand how slurry behave while pumping and if dead-zones can be avoided. In such way, metal-air RFB can continue to be developed in order to ensure a transition to more sustainable energy sources.

GENERAL CONCLUSION

The formulation of a zinc anode suspension for a zinc slurry – air redox flow battery (RFB) is presented in this work. Specifically, the formulation is studied with a rheometric approach in which key parameters were found to be important for the performance of the battery.

The first part of the study consisted in the preparation of the suspending fluid to be later used with zinc microparticles having a D_{50} of 76.4 μm. The objective was to formulate a gelled polymer electrolyte (GPE), consisting in an aqueous alkaline electrolyte (10 M KOH), and gelling agents. A yield stress behaviour was sought for the GPEs to avoid sedimentation of dense zinc particles ($\rho = 7.13\ g/cm^3$) when the battery is at rest, followed by a shear thinning behaviour producing a viscosity decrease as shear rate increases, easing the pumping in the RFB. Moreover, gelling agents had to be compatible with the harsh alkaline environment, required for the operation of the battery, to avoid chemical degradation leading to the loss of viscoplastic properties.

The gelling agents used in this study were polyacrylic acid (PAA, Carbopol® 940) in different concentrations and attapulgite clay (Attagel® 50). Rheometric characterisation was performed with a specific protocol to obtain the flow behaviour of GPEs, using a vane geometry specially designed for our samples. Using the Couette analogy [Aït-kadi et al., 2002], the raw results obtained with a vane-in-cup geometry were converted to shear stress and shear rate. By performing oscillatory rheometry, it was found that polyacrylic acid (PAA) together with attapulgite were able to form a gelled network even in such alkaline environment (pH $\gtrsim$ 14) characterised by storage moduli G' higher than the loss moduli G" independently of the angular frequency. Moreover, when performing large deformation tests, a yield stress followed by shear thinning behaviour was found independently of the PAA concentration used.

The second part of the study consisted in determining if PAA polymer was a suitable gelling agent to formulate zinc slurries. The objective consisted in determining if zinc interacted with PAA, forming an interconnected network in which PAA not only serves as mechanical support for zinc particles, but also as a good candidate to be an ionic carrier. The main hypothesis was

that if zinc-PAA interactions take place, the polymer would bound with zinc particles. After inducing sedimentation through a centrifugation step, if polymer was bound to the particles, this polymer would be removed from solution, and a depleted PAA supernatant would be recovered at the end of the step.

To validate our hypothesis, zinc suspensions were prepared using different concentrations of initial PAA and zinc. Next, the rheological behaviour of supernatants was compared to the rheological behaviour of the initial PAA gel used to prepare parent zinc suspensions. This was done using the so-called inverse rheometry method, in which by knowing the yield stress of a supernatant and its pH, it was possible to determine the PAA concentration in solution. It was found that yield stress of supernatants recovered after centrifugation was lower than the one of the initial gels used to prepare the parent suspensions. This result is linked to a lower PAA concentration in the supernatant, indicating that a part of the PAA settled together with zinc during the centrifugation step. Hence, in an indirect approach, rheometry endorses that during the suspension formulation, a part of the polymer effectively interacts with zinc, whereas the residual polymer remains free in supernatant. By labelling PAA polymer with rhodamine dye and follow its concentration in supernatant using a UV-Vis spectrometer, it was possible to confirm that polymer concentration in supernatant decreased. Indeed, this result validates our hypothesis of zinc-PAA interactions, resulting in free and bound polymer.

Hence, as interactions were identified using rheometry and spectroscopy, it was confirmed that PAA is a suitable gelling agent to be used in zinc slurries for application in RFB, providing an interconnected network where PAA is able to transport the discharge and charge ionic products of zinc.

In the third part of the study, the electrochemical performance of zinc slurries prepared with the GPEs studied in Chapter 3 is analysed. Slurries were tested in a zinc slurry – air RFB set-up, developed by Fraunhofer ICT, Germany, one of the FlowCamp partner institutes. Polarization curves, indicating the performance of the battery with the anode slurries, were obtained for each of the formulations tested. In the slurry formulation, the concentration of PAA gelling agent was studied from 0.2 to 0.6 wt. %. It was found that a maximum performance of 24 mW/cm^2 was obtained at an optimal PAA concentration of 0.4 wt. % PAA, improving previous results using the same experimental conditions [Choi et al., 2020a].

The origin of this optimal concentration was studied by different means. It was found that the yield stress of the suspending fluid, being the GPE at a PAA concentration of 0.40 wt. %, corresponded to the minimum yield stress τ_y, required to suspend zinc particles. The main result of this part is the link between yield stress and electrochemical performance: below yield stress the resulting formulation is not appropriate because suspensions are subjected to sedimentation and above yield stress, the increase in viscosity affects the ionic conductivity and energy used during pumping.

This study presents a new formulation for zinc slurry – air RFBs, consisting in a gelled alkaline electrolyte and zinc microparticles. The use of PAA gelling agent is extended to the alkaline environment, specific of zinc-air RFBs. Therefore, this study enriches the database of PAA applications, specifically as suspending fluid in alkaline conditions. With the rheometric approach presented in this manuscript, it is possible to have a better understanding on slurry-based batteries, by optimizing the formulation to be used from rheological key parameters, chiefly yield stress.

PERSPECTIVES

Pour continuer sur cette étude, et aller plus avant dans l'optimisation des batteries à flux redox au zinc, différentes voies peuvent être explorées. Cependant, du point de vue du procédé, l'un des défis majeurs concerne la compréhension et la maîtrise des propriétés d'écoulement de la suspension de zinc, dans les conditions de fonctionnement de la batterie.

Au sein du consortium FlowCamp, et en particulier au sein de l'équipe dédiée à l'étude de la batterie zinc-air, des simulations numériques sont développées en ce sens, l'objectif étant de prédire et d'augmenter la puissance délivrée en sortie de batterie. Ces simulations mettent en œuvre une cellule d'écoulement modèle, développée au moyen du logiciel COMSOL, et commune à l'ensemble des partenaires FlowCamp.

Il serait important d'apporter à ces simulations innovantes, couplant approches électrochimique et paramètres d'écoulement, des données expérimentales. Celles-ci, en plus de constituer une contribution déterminante à la caractérisation, et donc à la compréhension de la physique, des écoulements dans la batterie en fonctionnement, produiront une base qui fera référence, et permettra notamment de valider les résultats numériques et/ou d'orienter les options choisies pour des simulations signifiantes.

Nous avons posé les prémices d'une telle étude et développé un banc expérimental instrumenté, permettant de modéliser l'écoulement dans la cellule commune telle que définie au sein du consortium FlowCamp. Ce dispositif est représenté en figure 5.1 et illustré en figure 5.2.

Dans cette boucle d'écoulement en continu, le fluide est mis en mouvement au moyen d'un pousse-seringue (VIT-FIT, LAMBDA), la vitesse du piston permettant de contrôler le débit d'écoulement. Le débit est déterminé par pesage au moyen d'une balance (KERN 440) pilotée par un logiciel permettant de mesurer l'évolution de la masse de fluide en fonction du temps. Deux capteurs de pression (A-10, Wika), placés en entrée et en sortie de la cellule, permettent d'évaluer la perte de charge associée à l'écoulement. La mesure est là encore pilotée par un logiciel spécifique et accessible en direct sur ordinateur.

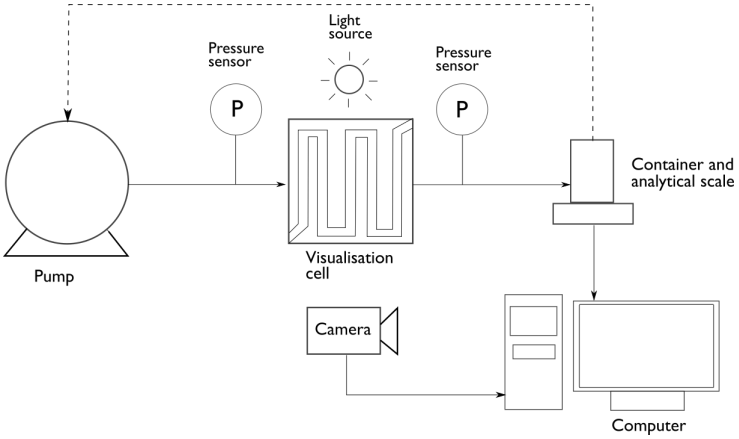

Figure 5.1: Schéma du banc expérimental.

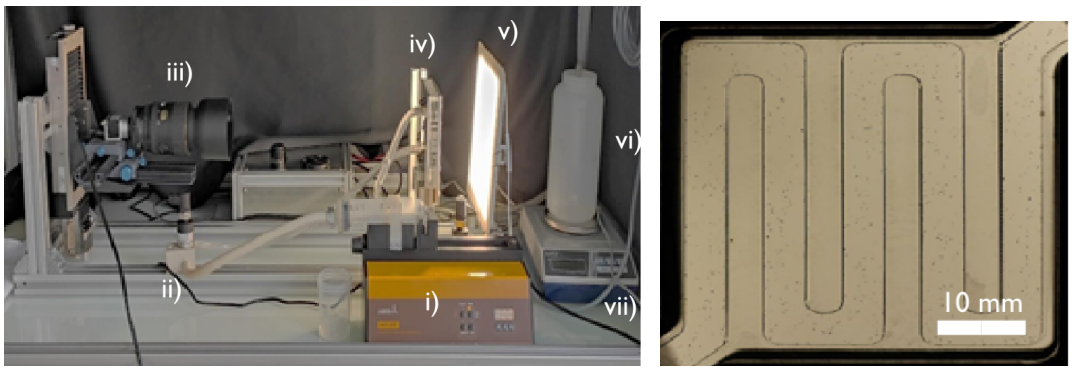

(a) (b)

Figure 5.2: a) Vue d'ensemble de dispositif expérimental. i) Pousse seringue, ii) Capteurs de pression, iii) Caméra et objectif, iv) Cellule d'écoulement, v) Éclairage, vi) Réservoir, vii) Balance, b) Cellule d'écoulement (PMMA) : chaque canal constituant le serpentin est caractérisé par une largeur de 50 mm, une hauteur de 2 mm et une épaisseur 5 mm.

Un système d'éclairage , constitué de une lampe LED (Colours, 17.5 W, Kingfisher International Products Limited) et une caméra (acA1920-25uc, BASLER) permettent de visualiser l'écoulement. Les images sont stockées sur ordinateur. Deux objectifs ont été utilisés. Un objectif standard, Nikkon 50 mm F 1,2 A, permettant une visualisation globale de l'écoulement. Un objectif macro, TOKINA Macro 100 mm F2,8 B, permettant d'analyser, avec une précision accrue, des zones spécifiques de l'écoulement.

Pour cette étude préliminaire, nous avons mis en œuvre un gel de PAA concentré à 0.2 wt % à pH 7. Ce gel est représentatif, en termes de comportement rhéologique, de la suspension S3, caractérisée par une performance électrochimique optimale (cf. Chapitre 5). En vue des expériences de visualisation, ce fluide a été ensemencé au moyen de billes de verre de 100/200 μm de diamètre à une concentration volumique $\phi = 0.04$. Ces particules permettent d'obtenir un contraste important et facilite l'exploitation des images qui sont réalisées.

Les images obtenues sont traitées par le logiciel DynamicStudio (Dantec Dynamics). Il donne accès aux champs de vitesse en tout point de l'écoulement, en analysant deux images séparées par un intervalle de temps connu Δt, selon le principe de la PIV [Raffel et al., 1998]. Sans rentrer dans le détail, cette technique permet de calculer le déplacement des particules pendant le temps Δt et d'en déduire la vitesse en tout point du cliché, par des méthodes de corrélations statistiques réalisées sur plusieurs pairs d'images.

Nos premiers résultats sont encourageants en même temps qu'ils mettent en évidence les pistes d'amélioration potentielle du dispositif.

Mesures de pression

Ainsi, en figure 5.3 sont reportées l'évolution de la pression en fonction du temps pour 3 débits différents. Un régime permanent est obtenu pour les débits les plus faibles : au bout de 10s pour le débit de 0.2 cm^3/s et de 20 s pour le débite de 0.4 cm^3/s. Il est clair cependant qu'il n'en est rien pour le débit de 0.8 cm^3/s : la seringue est vide de manière prématurée. C'est un point d'amélioration à envisager.

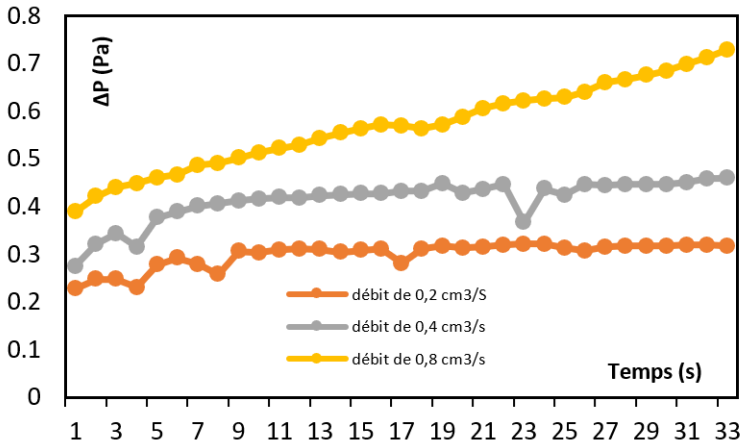

Figure 5.3: Perte de charge ΔP aux bornes de la cellule pour différents débits d'écoulement.

Champs de vitesse

Pour chacun des deux débits les plus faibles, nous avons analysé les champs de vitesse.

Ecoulement dans les canaux en zone centrale :

Les résultats sont représentés en figure 5.4 pour le débit de 0.2 cm^3/s.

Les résultats sont ceux attendus, avec une vitesse maximale au centre des canaux et une vitesse faible au voisinage des parois. Le même type de comportement est observé à 0.2 cm^3/s. On peut ensuite extraire de ces premières analyses le profil de vitesse dans les canaux d'écoulement, en fonction de la hauteur dans l'écoulement. Un résultat obtenu pour un débit

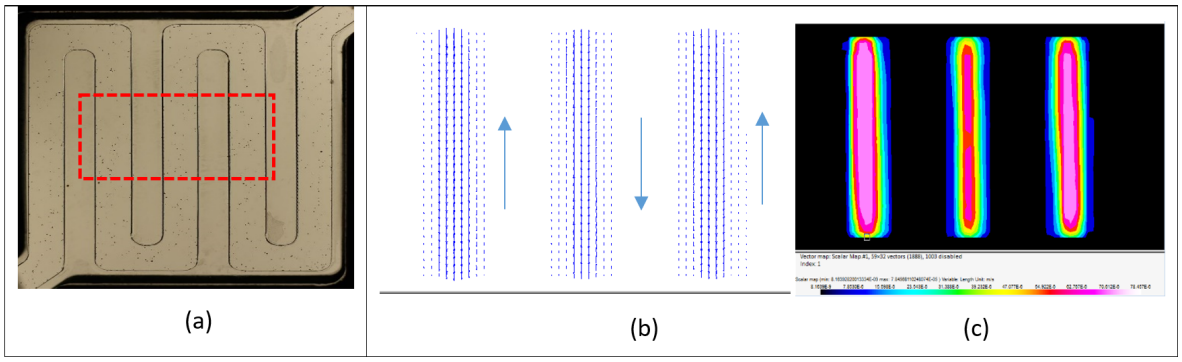

Figure 5.4: Écoulement à 0.2 cm^3/s. (a) cellule d'écoulement et zone d'analyse en PIV ; (b) vecteurs vitesses dans les canaux d'écoulement avec indication du sens de l'écoulement ; (c) champs de vitesse.

de 0.4 cm^3/s, à mi-hauteur des canaux, est représenté en figure 5.5.

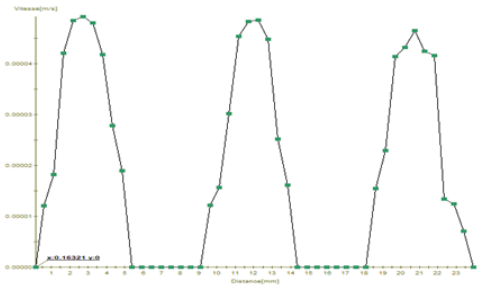

Figure 5.5: Profil de vitesse à mi-hauteur dans les canaux pour un débit de 0.4 cm^3/s.

Aux erreurs de mesures près, ces mesures préliminaires montrent que dans chaque canal, l'écoulement est de type Poiseuille, avec une vitesse nulle aux parois et maximale au centre. L'analyse précise des vitesses dans chaque canal, et des vitesses maximales en particulier, permettrait d'évaluer l'homogénéité et la stabilité de l'écoulement en circuit continu.

Ecoulement dans les angles :

Les résultats sont représentés en figure 5.6 pour le débit de 0.4 cm^3/s. Les zones analysées sont schématisées en figure 5.6a. Les résultats de PIV sont représentés en figure 5.6b pour les écoulements dans les angles supérieurs de la cellule ; en figure 5.6c pour les écoulements dans les angles inférieurs de la cellule.

Là encore, les résultats sont ceux attendus, traduisant des gradients importants, avec des vitesses maximales dans la partie centrale et des vitesses quasi-nulles plus on s'approche des parois. On constate cependant des pertes de symétrie du champ de vitesse dans les différents canaux, hauts et bas. Aucune conclusion à ce stade ne peut cependant en être tirée. De tels effets pourraient être en effet attribuables à des défauts de réglage à ce stade de développement de l'installation.

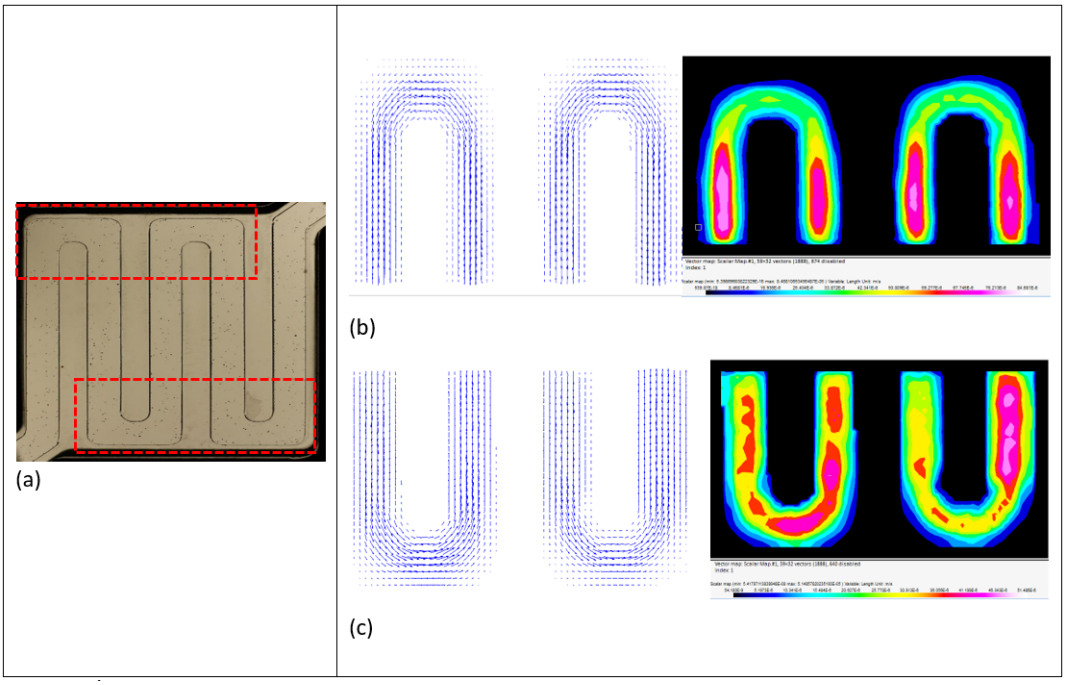

Figure 5.6: Écoulement à un débit de 0.4 cm^3/s : a) identifications des zones d'analyse en PIV ; b) vecteurs et champs de vitesse dans les angles supérieurs ; c) vecteurs et champs de vitesse dans les angles inférieurs.

Ces tous premiers résultats ont le mérite de mettre en évidence la faisabilité et la validité du banc expérimental développé. Il est clair que nous sommes aujourd'hui en mesure d'envisager une modélisation expérimentale des écoulements, dans une cellule représentative du fonctionnement des batteries à flux redox, qui pourra être mis en œuvre pour différents fluides, modèles ou réels. Il pourra par ailleurs être équipé de cellules avec des géométries de canaux diverses. Son intérêt pour les développements futurs apparaît ainsi certain et multiple. Il s'agit maintenant d'affiner les réglages de ce dispositif avant de multiplier les mesures et d'obtenir une cartographie des écoulements, tant d'un point de vue qualitatif que quantitatif, dans les conditions d'usage de la batterie. Une véritable base de données pourra alors être constituée, permettant de confronter résultats expérimentaux et simulations et, le cas échéant, de valider les hypothèses et les options choisies pour les développements numériques.

BIBLIOGRAPHY

Abdo, J and M. D. Haneef (2013). "Clay nanoparticles modified drilling fluids for drilling of deep hydrocarbon wells". In: *Applied Clay Science* 86, pp. 76–82.

Acrivos, A., R. Mauri, and X. Fan (1993). "Shear-induced resuspension in a couette device". In: *International Journal of Multiphase Flow* 19.5, pp. 797–802.

Aït-kadi, A., P. Marchal, L. Choplin, and M. Bousmina (2002). "Quantitative Analysis of Mixer-Type Rheometers". In: *The Canadian Journal of Chemical Engineering* 80.December, pp. 1166–1174.

Aral, B. K. and D. M. Kalyon (1994). "Effects of temperature and surface roughness on time-dependent development of wall slip in steady torsional flow of concentrated suspensions". In: *Journal of Rheology* 38.4, pp. 957–972.

Argyrou, M. C., P. Christodoulides, and S. A. Kalogirou (2018). *Energy storage for electricity generation and related processes: Technologies appraisal and grid scale applications.*

Armand, M. and J. M. Tarascon (2008). "Building better batteries". In: *Nature* 451, pp. 652–657.

Auffret, Y, D. C. Roux, N. El Kissi, F Caton, I Pignot-Paintrand, D. E. Dunstan, and C Rochas (2009a). "Aging and yielding in a sheared AOT/iso-octane/water lyotropic lamellar phase". In: *European Physical Journal E* 29.1, pp. 51–60.

Auffret, Y, D. C. Roux, N. El Kissi, D. E. Dunstan, and I. Pignot-Paintrand (2009b). "Stress and strain controlled rheometry on a concentrated lyotropic lamellar phase of AOT/Water/Iso-octane". In: *Rheologica Acta* 48.4, pp. 423–432.

Balmforth, N. J., I. A. Frigaard, and G. Ovarlez (2014). "Yielding to stress: Recent developments in viscoplastic fluid mechanics". In: *Annual Review of Fluid Mechanics* 46, pp. 121–146.

Banik, S. J. and R. Akolkar (2013). "Suppressing Dendrite Growth during Zinc Electrodeposition by PEG-200 Additive". In: *Journal of The Electrochemical Society* 160.11, pp. D519–D523.

Banik, S. J. and R. Akolkar (2015). "Suppressing Dendritic Growth during Alkaline Zinc Electrodeposition using Polyethylenimine Additive". In: *Electrochimica Acta* 179, pp. 475–481.

Baravian, C., A. Lalante, and A. Parker (2002). "Vane rheometry with a large, finite gap". In: *Applied Rheology* 12.2, pp. 81–87.

Baravian, C. and D. Quemada (1998). "Using instrumental inertia in controlled stress rheometry". In: *Rheologica Acta* 37.3, pp. 223–233.

Barnes, H. A. (1999). "The yield stress-a review or '$\pi\alpha\nu\tau\alpha$ $\rho\epsilon\iota$'-everything flows?" In: *Journal of Non-Newtonian Fluid Mechanics* 81.1-2, pp. 133–178.

Barnes, H. A. and Q. D. Nguyen (2001). *Rotating vane rheometry-a review.*

Barton, J. L., J. D. Milshtein, J. J. Hinricher, and F. R. Brushett (2018). "Quantifying the impact of viscosity on mass-transfer coefficients in redox flow batteries". In: *Journal of Power Sources* 399, pp. 133–143.

Batchelor, G. K. and J. T. Green (1972a). "The determination of the bulk stress in a suspension of spherical particles to order c2". In: *Journal of Fluid Mechanics* 56.3, pp. 401–427.

— (1972b). "The hydrodynamic interaction of two small freely-moving spheres in a linear flow field". In: *Journal of Fluid Mechanics* 56.2, pp. 375–400.

Bazilian, M., M. Bradshaw, J. Gabriel, A. Goldthau, and K. Westphal (2020). "Four scenarios of the energy transition: Drivers, consequences, and implications for geopolitics". In: *Wiley Interdisciplinary Reviews: Climate Change* 11.2.

Beaudin, M., H. Zareipour, A. Schellenberg, and W. Rosehart (2015). *Energy Storage for Mitigating the Variability of Renewable Electricity Sources.* Elsevier Inc., pp. 1–33.

Beija, M., C. A. Afonso, and J. M. Martinho (2009). "Synthesis and applications of rhodamine derivatives as fluorescent probes". In: *Chemical Society Reviews* 38.8, pp. 2410–2433.

Benmouffok-Benbelkacem, G., F. Caton, C. Baravian, and S. Skali-Lami (2010). "Non-linear viscoelasticity and temporal behavior of typical yield stress fluids: Carbopol, Xanthan and Ketchup". In: *Rheologica Acta* 49.3, pp. 305–314.

Bernkop-Schnürch, A. and M. E. Krajicek (1998). "Mucoadhesive polymers as platforms for peroral peptide delivery and absorption: Synthesis and evaluation of different chitosan-EDTA conjugates". In: *Journal of Controlled Release* 50.1-3, pp. 215–223.

Bertola, V, F Bertrand, H Tabuteau, D Bonn, and P Coussot (2003). "Wall slip and yielding in pasty materials". In: *Journal of Rheology* 47.5, pp. 1211–1226.

Blakers, A., M. Stocks, B. Lu, and C. Cheng (2021). "A review of pumped hydro energy storage". In: *Progress in Energy* 3.2, p. 022003.

Bockelmann, M., U. Kunz, and T. Turek (2016). "Electrically rechargeable zinc-oxygen flow battery with high power density". In: *Electrochemistry Communications* 69, pp. 24–27.

Boger, D. V. (2013). "Rheology of slurries and environmental impacts in the mining industry". In: *Annual Review of Chemical and Biomolecular Engineering* 4, pp. 239–257.

Bonnoit, C, T Darnige, E Clement, and A Lindner (2010). "Inclined plane rheometry of a dense granular suspension". In: *Journal of Rheology* 54.1, pp. 65–79.

Bossis, G, E Lemaire, O Volkova, and H Clercx (1997). "Yield stress in magnetorheological and electrorheological fluids: A comparison between microscopic and macroscopic structural models". In: *Journal of Rheology* 41.3, pp. 687–704.

Boyé, H. and M. Vivo (2016). "The environmental and social acceptability of dams". In: *Field Actions Science Reports. The journal of field actions* Special Issue 14.

Boyer, F., É. Guazzelli, and O. Pouliquen (2011). "Unifying suspension and granular rheology". In: *Physical Review Letters* 107.18, pp. 1–5.

Breyer, C. and A. Gerlach (2013). "Global overview on grid-parity". In: *Progress in Photovoltaics: Research and Applications* 21.1, pp. 121–136.

Briscoe, B. J., P. F. Luckham, and S. R. Ren (1994). "The properties of drilling muds at high pressures and high temperatures". In: *Philosophical Transactions - Royal Society of London, A* 348.1687, pp. 179–207.

Brito-De La Fuente, E., L. Choplin, and P. A. Tanguy (1997). "Mixing with helical ribbon impellers: Effect of highly shear thinning behaviour and impeller geometry". In: *Chemical Engineering Research and Design* 75.1, pp. 45–52.

Brushett, F. R., M. J. Aziz, and K. E. Rodby (2020). *On Lifetime and Cost of Redox-Active Organics for Aqueous Flow Batteries.*

Cabot, P. L., M Cortes, F Centellas, and E Perez (1993). "Potentiostatic passivation of zinc in alkaline solutions". In: *Journal of Applied Electrochemistry* 23.4, pp. 371–378.

Caramia, V. and B. Bozzini (2014). "Materials science aspects of zinc-air batteries: A review". In: *Materials for Renewable and Sustainable Energy* 3.2.

Carreau, P. J., R. P Chhabra, and J. Cheng (1993). "Effect of Rheological Properties on Power Consumption with Helical Ribbon Agitatos". In: *AIChE Journal* 39.9, pp. 1421–1430.

Caton, F. and C. Baravian (2008). "Plastic behavior of some yield stress fluids: From creep to long-time yield". In: *Rheologica Acta* 47.5-6, pp. 601–607.

Chang, S. H., M. H. Ryan, and R. K. Gupta (1993). "The effect of pH, ionic strength, and temperature on the rheology and stability of aqueous clay suspensions". In: *Rheologica Acta* 32.3, pp. 263–269.

Charman, W. N., D. P. Christy, E. P. Geunin, and D. C. Monkhouse (1991). "Interaction between calcium, a model divalent cation, and a range of poly (acrylic acid) resins as a function of solution ph". In: *Drug Development and Industrial Pharmacy* 17.2, pp. 271–280.

Chateau, X., G. Ovarlez, and K. L. Trung (2008). "Homogenization approach to the behavior of suspensions of noncolloidal particles in yield stress fluids". In: *Journal of Rheology* 52.2, pp. 489–506. arXiv: 1006.2293.

Cheng, D. C. (1986). "Yield stress: A time-dependent property and how to measure it". In: *Rheologica Acta* 25.5, pp. 542–554.

Choi, C., S. Kim, R. Kim, Y. Choi, S. Kim, H. young Jung, J. H. Yang, and H. T. Kim (2017). *A review of vanadium electrolytes for vanadium redox flow batteries.*

Choi, N. H., D. Del Olmo, P. Fischer, K. Pinkwart, and J. Tübke (2020a). "Development of flow fields for zinc slurry air flow batteries". In: *Batteries* 6.1, p. 15.

Choi, N. H., D. del Olmo, D. Milian, P. Fischer, K. Pinkwart, and J. Tübke (2020b). "Use of carbon additives towards rechargeable Zinc Slurry Air Flow Batteries". In: *Energies* 13.17, p. 4482.

Ciez, R. E. and J. F. Whitacre (2016). "The cost of lithium is unlikely to upend the price of Li-ion storage systems". In: *Journal of Power Sources* 320, pp. 310–313.

Clark, P. E. (1995). "Drilling mud rheology and the API recommended measurements". In: *Society of Petroleum Engineers - SPE Production Operations Symposium 1995, POS 1995.* Vol. 1995-April. OnePetro, pp. 933–941.

Cohu, O. and A. Magnin (1995). "Rheometry of paints with regard to roll coating process". In: *Journal of Rheology* 39.4, pp. 767–785.

Coussot, P (2018). *Slow flows of yield stress fluids: yielding liquids or flowing solids?*

Coussot, P, J. S. Raynaud, F Bertrand, P Moucheront, J. P. Guilbaud, H. T. Huynh, S Jarny, and D Lesueur (2002). "Coexistence of liquid and solid phases in flowing soft-glassy materials". In: *Physical Review Letters* 88.21, pp. 2183011–2183014.

Coussot, P. (2005). *Rheometry of Pastes, Suspensions, and Granular Materials: Applications in Industry and Environment.* Hoboken, NJ, USA: John Wiley & Sons, Inc., pp. 1–291.

Coussot, P., S. Proust, and C. Ancey (1996). "Rheological interpretation of deposits of yield stress fluids". In: *Journal of Non-Newtonian Fluid Mechanics* 66.1, pp. 55–70.

Curran, S. J., R. Hayes, A. Afacan, M. C. Williams, and P. A. Tanguy (2002). "Properties of Carbopol Solutions as Models for Yield-Stress Fluids". In: *Journal of Food Science* 67.1, pp. 176–180.

Cwalina, C. D. and N. J. Wagner (2016). "Rheology of non-Brownian particles suspended in concentrated colloidal dispersions at low particle Reynolds number". In: *Journal of Rheology* 60.1, pp. 47–59.

Dagois-Bohy, S., S. Hormozi, É. Guazzelli, and O. Pouliquen (2015). "Rheology of dense suspensions of non-colloidal spheres in yield-stress fluids". In: *Journal of Fluid Mechanics* 776, R2.

Dail, R. V. and J. F. Steffe (1990). "Dilatancy in Starch Solutions Under Low Acid Aseptic Processing Conditions". In: *Journal of Food Science* 55.6, pp. 1764–1765.

Davari, E and D. G. Ivey (2018). "Bifunctional electrocatalysts for Zn-air batteries". In: *Sustainable Energy and Fuels* 2.1, pp. 39–67.

De Larrard, F, C. F. Ferraris, and T Sedran (1998). "Fresh concrete: A Herschel-Bulkley material". In: *Materials and Structures* 31, pp. 494–498.

Deane, J. P., B. P. Ó Gallachóir, and E. J. McKeogh (2010). *Techno-economic review of existing and new pumped hydro energy storage plant.*

Denn, M. M. and J. F. Morris (2014). *Rheology of non-brownian suspensions.*

Deshpande, A. P., J. M. Krishnan, and P. B. Kumar (2010). *Rheology of complex fluids*, pp. 1–257.

Dinkgreve, M, M Fazilati, M. M. Denn, and D. Bonn (2018). "Carbopol: From a simple to a thixotropic yield stress fluid". In: *Journal of Rheology* 62.3, pp. 773–780.

Dinkgreve, M., J. Paredes, M. M. Denn, and D. Bonn (2016). "On different ways of measuring "the" yield stress". In: *Journal of Non-Newtonian Fluid Mechanics* 238, pp. 233–241.

Divoux, T., M. A. Fardin, S. Manneville, and S. Lerouge (2016). "Shear Banding of Complex Fluids". In: *Annual Review of Fluid Mechanics* 48, pp. 81–103. arXiv: 1503.04130.

Dratler, D. I., W. R. Schowalter, and R. L. Hoffman (1997). "Dynamic simulation of shear thickening in concentrated colloidal suspensions". In: *Journal of Fluid Mechanics* 353, pp. 1–30.

Duduta, M., B. Ho, V. C. Wood, P. Limthongkul, V. E. Brunini, W. C. Carter, and Y. M. Chiang (2011). "Semi-solid lithium rechargeable flow battery". In: *Advanced Energy Materials* 1.4, pp. 511–516.

Dunn, B., H. Kamath, and J. M. Tarascon (2011). *Electrical energy storage for the grid: A battery of choices.*

Dzuy, N. Q. and D. V. Boger (1985). "Direct Yield Stress Measurement with the Vane Method". In: *Journal of Rheology* 29.3, pp. 335–347.

Dzuy, N. Q. and D. V. Boger (1983a). "Yield Stress Measurement for Concentrated Suspensions". In: *Journal of Rheology* 27.4, pp. 321–349.

— (1983b). "Yield Stress Measurement for Concentrated Suspensions". In: *Journal of Rheology* 27.4, pp. 321–349.

EDF Renewables in Germany — Performances & Services (n.d.).

Einstein, A. (1911). "Berichtigung zu meiner Arbeit: Eine neue Bestimmung der Moleküldimensionen". In: *Annalen der Physik* 339.3, pp. 591–592.

— (1906). "Eine neue Bestimmung der Moleküldimensionen". In: *Annalen der Physik* 324.2, pp. 289–306.

Eitelberg, G (1984). *Corrigendum to Weissenberg effect and its dependence upon the experimental geometry.*

Emady, H., M. Caggioni, and P. Spicer (2013). "Colloidal microstructure effects on particle sedimentation in yield stress fluids". In: *Journal of Rheology* 57.6, pp. 1761–1772.

Eugénie, S. d. P., D. Fabrice, C. Gérard, and M. Samir (2014). "Effect of bulk viscosity and surface tension kinetics on structure offoam generated at the pilot scale". In: *Food Hydrocolloids* 34, pp. 104–111.

European Commission (2019). *The European Green Deal*.

Eurostat (2020). *Energy data 2020 edition*. Tech. rep., p. 334.

Fabbrizzi, L. (2019). "Strange Case of Signor Volta and Mister Nicholson: How Electrochemistry Developed as a Consequence of an Editorial Misconduct". In: *Angewandte Chemie - International Edition* 58.18, pp. 5810–5822.

Fan, F. Y., W. H. Woodford, Z. Li, N. Baram, K. C. Smith, A. Helal, G. H. McKinley, W. C. Carter, and Y. M. Chiang (2014). "Polysulfide flow batteries enabled by percolating nanoscale conductor networks". In: *Nano Letters* 14.4, pp. 2210–2218.

Foss, D. R. and J. F. Brady (2000). "Structure, diffusion and rheology of Brownian suspensions by Stokesian Dynamics simulation". In: *Journal of Fluid Mechanics* 407, pp. 167–200.

Frigaard, I. (2019). *Simple yield stress fluids*.

Fu, J., Z. P. Cano, M. G. Park, A. Yu, M. Fowler, and Z. Chen (2017). "Electrically Rechargeable Zinc–Air Batteries: Progress, Challenges, and Perspectives". In: *Advanced Materials* 29.7.

Garole, D. J., R. Hossain, V. J. Garole, V. Sahajwalla, J. Nerkar, and D. P. Dubal (2020). "Recycle, Recover and Repurpose Strategy of Spent Li-ion Batteries and Catalysts: Current Status and Future Opportunities". In: *ChemSusChem* 13.12, pp. 3079–3100.

Gielen, D., F. Boshell, D. Saygin, M. D. Bazilian, N. Wagner, and R. Gorini (2019). "The role of renewable energy in the global energy transformation". In: *Energy Strategy Reviews* 24, pp. 38–50.

Gopalakrishnan, V and C. F. Zukoski (2004). "Effect of attractions on shear thickening in dense suspensions". In: *Journal of Rheology* 48.6, pp. 1321–1344.

Gruber, P. W., P. A. Medina, G. A. Keoleian, S. E. Kesler, M. P. Everson, and T. J. Wallington (2011). "Global lithium availability: A constraint for electric vehicles?" In: *Journal of Industrial Ecology* 15.5, pp. 760–775.

Guazzelli, É. and O. Pouliquen (2018). "Rheology of dense granular suspensions". In: *Journal of Fluid Mechanics* 852, P11–P173.

Gubler, L. (2019). *Membranes and separators for redox flow batteries*.

Guo, Y., Y. N. Chen, H. Cui, and Z. Zhou (2019). "Bifunctional electrocatalysts for rechargeable Zn-air batteries". In: *Chinese Journal of Catalysis* 40.9, pp. 1298–1310.

Gutowski, I. A., D. Lee, J. R. de Bruyn, and B. J. Frisken (2012). "Scaling and mesostructure of Carbopol dispersions". In: *Rheologica Acta* 51.5, pp. 441–450.

Guvendiren, M., H. D. Lu, and J. A. Burdick (2012). *Shear-thinning hydrogels for biomedical applications*.

Haack, R. A., S. Gayda, R. J. Himmelsbach, and S. Y. Tetin (2017). "Unexpected reactivity of the 2-carboxyl functionality in rhodamine dyes". In: *Tetrahedron Letters* 58.18, pp. 1733–1737.

Haden, W. L. and I. A. Schwint (1967). "ATTAPULGITE: ITS PROPERTIES AND APPLICATIONS". In: *Industrial & Engineering Chemistry* 59.9, pp. 58–69.

Han, X., X. Li, J. White, C. Zhong, Y. Deng, W. Hu, and T. Ma (2018). "Metal–Air Batteries: From Static to Flow System". In: *Advanced Energy Materials* 8.27, pp. 1–28.

Hermes, M., B. M. Guy, W. C. K. Poon, G. Poy, M. E. Cates, and M. Wyart (2016). "Unsteady flow and particle migration in dense, non-Brownian suspensions". In: *Journal of Rheology* 60.5, pp. 905–916. arXiv: `1511.08011`.

Hermoso, J., B. D. Jofore, F. J. Martínez-Boza, and C. Gallegos (2012). "High pressure mixing rheology of drilling fluids". In: *Industrial and Engineering Chemistry Research* 51.44, pp. 14399–14407.

Hester, R. D. and D. R. Squire (1997). *Rheology of waterborne coatings*.

Hoffman, R. L. (1998). "Explanations for the cause of shear thickening in concentrated colloidal suspensions". In: *Journal of Rheology* 42.1, pp. 111–123.

Hreiz, R., N. Adouani, D. Fünfschilling, P. Marchal, and M. N. Pons (2017). "Rheological characterization of raw and anaerobically digested cow slurry". In: *Chemical Engineering Research and Design* 119, pp. 47–57.

Hu, C. and F. De Larrard (1996). "The rheology of fresh high-performance concrete". In: *Cement and Concrete Research* 26.2, pp. 283–294.

Huang, Q. and Q. Wang (2015). "Next-generation, high-energy-density redox flow batteries". In: *ChemPlusChem* 80.2, pp. 312–322.

Hubbard, R. M. and G. G. Brown (1943). "The Rolling Ball Viscometer". In: *Industrial and Engineering Chemistry - Analytical Edition* 15.3, pp. 212–218.

Huggins, R. A. (2015). *Energy storage: Fundamentals, materials and applications, second edition*. Springer International Publishing, pp. 1–509.

Imanishi, N and O Yamamoto (2019). *Perspectives and challenges of rechargeable lithium–air batteries*.

Iyer, V. A., J. K. Schuh, E. C. Montoto, V Pavan Nemani, S. Qian, G. Nagarjuna, J. Rodríguez-López, R. H. Ewoldt, and K. C. Smith (2017). "Assessing the impact of electrolyte conductivity and viscosity on the reactor cost and pressure drop of redox-active polymer flow batteries". In: *Journal of Power Sources* 361, pp. 334–344.

Jiang, H. R., M. C. Wu, Y. X. Ren, W. Shyy, and T. S. Zhao (2018). "Towards a uniform distribution of zinc in the negative electrode for zinc bromine flow batteries". In: *Applied Energy* 213.August 2017, pp. 366–374.

Jörissen, L. (2006). "Bifunctional oxygen/air electrodes". In: *Journal of Power Sources* 155.1, pp. 23–32.

Kapila, S., A. O. Oni, E. D. Gemechu, and A. Kumar (2019). "Development of net energy ratios and life cycle greenhouse gas emissions of large-scale mechanical energy storage systems". In: *Energy* 170, pp. 592–603.

Kear, G., A. A. Shah, and F. C. Walsh (2012). "Development of the all-vanadium redox flow battery for energy storage: A review of technological, Financial and policy aspects". In: *International Journal of Energy Research* 36.11, pp. 1105–1120.

Keegan, G., J. Smart, M. Ingram, L. Barnes, G. Rees, and G. Burnett (2007). "An in vitro assessment of bioadhesive zinc/carbomer complexes for antimicrobial therapy within the oral cavity". In: *International Journal of Pharmaceutics* 340.1-2, pp. 92–96.

Keentok, M (1982). "The measurement of the yield stress of liquids". In: *Rheologica Acta* 21.3, pp. 325–332.

Kim, H., G. Jeong, Y. U. Kim, J. H. Kim, C. M. Park, and H. J. Sohn (2013). *Metallic anodes for next generation secondary batteries*.

Kittner, N., F. Lill, and D. M. Kammen (2017). "Energy storage deployment and innovation for the clean energy transition". In: *Nature Energy* 2.9.

Kong, L., C. Li, J. Jiang, and M. G. Pecht (2018). "Li-ion battery fire hazards and safety strategies". In: *Energies* 11.9, pp. 1–11.

Krieger, I. M. and T. J. Dougherty (1959). "A Mechanism for Non-Newtonian Flow in Suspensions of Rigid Spheres". In: *Transactions of the Society of Rheology* 3.1, pp. 137–152.

Kurzweil, P (2010). "Gaston Planté and his invention of the lead-acid battery-The genesis of the first practical rechargeable battery". In: *Journal of Power Sources* 195.14, pp. 4424–4434.

Lang, C., J. Kohlbrecher, L. Porcar, A. Radulescu, K. Sellinghoff, J. K. G. Dhont, and M. P. Lettinga (2019). "Microstructural Understanding of the Length- And Stiffness-Dependent Shear Thinning in Semidilute Colloidal Rods". In: *Macromolecules* 52.24, pp. 9604–9612. arXiv: `1910.08349`.

Lao-atiman, W., S. Olaru, A. Arpornwichanop, and S. Kheawhom (2019). "Discharge performance and dynamic behavior of refuellable zinc-air battery". In: *Scientific Data* 6.1.

Lebranchu, A., S. Delaunay, P. Marchal, F. Blanchard, S. Pacaud, M. Fick, and E. Olmos (2017). "Impact of shear stress and impeller design on the production of biogas in anaerobic digesters". In: *Bioresource Technology* 245.June, pp. 1139–1147.

Lee, D., I. A. Gutowski, A. E. Bailey, L. Rubatat, J. R. De Bruyn, and B. J. Frisken (2011a). "Investigating the microstructure of a yield-stress fluid by light scattering". In: *Physical Review E - Statistical, Nonlinear, and Soft Matter Physics* 83.3, pp. 1–8.

Lee, J. S., S. T. Kim, R. Cao, N. S. Choi, M. Liu, K. T. Lee, and J. Cho (2011b). "Metal-air batteries with high energy density: Li-air versus Zn-air". In: *Advanced Energy Materials* 1.1, pp. 34–50.

Li, M., J. Lu, Z. Chen, and K. Amine (2018). *30 Years of Lithium-Ion Batteries*.

Li, Y., M. Gong, Y. Liang, J. Feng, J. E. Kim, H. Wang, G. Hong, B. Zhang, and H. Dai (2013). "Advanced zinc-air batteries based on high-performance hybrid electrocatalysts". In: *Nature Communications* 4.

Liddle, B. and P. Sadorsky (2020). "How much do asymmetric changes in income and energy prices affect energy demand?" In: *Journal of Economic Asymmetries* 21.

Liu, T. W. (1989). "Flexible polymer chain dynamics and rheological properties in steady flows". In: *The Journal of Chemical Physics* 90.10, pp. 5826–5842.

Liu, X., J. Guo, Y. Cheng, G. Xu, Y. Li, and P. Cui (2010). "Synthesis and electrorheological properties of polar molecule-dominated TiO2 particles with high yield stress". In: *Rheologica Acta* 49.8, pp. 837–843.

Liu, Z., G. Pulletikurthi, A. Lahiri, T. Cui, and F. Endres (2016). "Suppressing the dendritic growth of zinc in an ionic liquid containing cationic and anionic zinc complexes for battery applications". In: *Dalton Transactions* 45.19, pp. 8089–8098.

Lochhead, R. Y., J. A. Davidson, and G. M. Thomas (1989). "Poly(acrylic acid) thickeners. The importance of gel microrheology and evaluation of hydrophobically modified derivatives as emulsifiers". In: *Adv.Chem.Ser.* 223.Polym. Aqueous Media, pp. 113–147.

Loftus, P. J., A. M. Cohen, J. C. Long, and J. D. Jenkins (2015). "A critical review of global decarbonization scenarios: What do they tell us about feasibility?" In: *Wiley Interdisciplinary Reviews: Climate Change* 6.1, pp. 93–112.

Lohaus, J., D. Rall, M. Kruse, V. Steinberger, and M. Wessling (2019). "On charge percolation in slurry electrodes used in vanadium redox flow batteries". In: *Electrochemistry Communications* 101.March, pp. 104–108.

Lourenssen, K., J. Williams, F. Ahmadpour, R. Clemmer, and S. Tasnim (2019). *Vanadium redox flow batteries: A comprehensive review.*

Macosko, C. W. (1994). *Rheology: Principles, Measurements, and Applications.* Wiley-VCH.

Madraki, Y., S. Hormozi, G. Ovarlez, É. Guazzelli, and O. Pouliquen (2017). "Enhancing shear thickening". In: *Physical Review Fluids* 2.3, p. 33301.

Magnin, A and J. M. Piau (1990). "Cone-and-plate rheometry of yield stress fluids. Study of an aqueous gel". In: *Journal of Non-Newtonian Fluid Mechanics* 36.C, pp. 85–108.

— (1987). "Shear rheometry of fluids with a yield stress". In: *Journal of Non-Newtonian Fluid Mechanics* 23.C, pp. 91–106.

Mahaut, F., X. Chateau, P. Coussot, and G. Ovarlez (2008). "Yield stress and elastic modulus of suspensions of noncolloidal particles in yield stress fluids". In: *Journal of Rheology* 52.1, pp. 287–313. arXiv: 0810.3487.

Mahlendorf, F., A. Heinzel, C. Mueller, and D. Fuchs (2021). "Secondary zinc-air batteries – mechanically rechargeable". In: *Electrochemical Power Sources: Fundamentals, Systems, and Applications.* Elsevier, pp. 99–123.

Mainar, A. R., L. C. Colmenares, J. A. Blázquez, and I. Urdampilleta (2018a). "A brief overview of secondary zinc anode development: The key of improving zinc-based energy storage systems". In: *International Journal of Energy Research* 42.3, pp. 903–918.

Mainar, A. R., L. C. Colmenares, H. J. Grande, and J. A. Blázquez (2018b). "Enhancing the cycle life of a Zinc–air battery by means of electrolyte additives and zinc surface protection". In: *Batteries* 4.3.

Mainar, A. R., E. Iruin, L. C. Colmenares, J. A. Blázquez, and H. J. Grande (2018c). "Systematic cycle life assessment of a secondary zinc–air battery as a function of the alkaline electrolyte composition". In: *Energy Science and Engineering* 6.3, pp. 174–186.

Mainar, A. R., E. Iruin, L. C. Colmenares, A. Kvasha, I. de Meatza, M. Bengoechea, O. Leonet, I. Boyano, Z. Zhang, and J. A. Blazquez (2018d). "An overview of progress in electrolytes for secondary zinc-air batteries and other storage systems based on zinc". In: *Journal of Energy Storage* 15, pp. 304–328.

Mainar, A. R., L. Olatz, M. Bengoechea, I. Boyano, I. de Meatza, A. Kvasha, A. Guerfi, and J. A. Blazquez (2016). "Alkaline aqueous electrolytes for secondary zinc-air batteries: an overview". In: *International Journal of Energy Research* 40, pp. 1032–1049. arXiv: `arXiv:1011.1669v3`.

Mansard, V. and A. Colin (2012). "Local and non local rheology of concentrated particles". In: *Soft Matter* 8.15, pp. 4025–4043.

Manthiram, A. (2020). *A reflection on lithium-ion battery cathode chemistry.*

Mari, R., R. Seto, J. F. Morris, and M. M. Denn (2014). "Shear thickening, frictionless and frictional rheologies in non-Brownian suspensions". In: *Journal of Rheology* 58.6, pp. 1693–1724. arXiv: `1403.6793`.

Mele, C., A. Bilotta, P. Bocchetta, and B. Bozzini (2017). "Characterization of the particulate anode of a laboratory flow Zn–air fuel cell". In: *Journal of Applied Electrochemistry* 47.8, pp. 877–888.

Mele, C. and B. Bozzini (2015). "Spectroelectrochemical investigation of the anodic and cathodic behaviour of zinc in 5.3 M KOH". In: *Journal of Applied Electrochemistry* 45.1, pp. 43–50.

Milner, S. T. (1996). "Relating the shear-thinning curve to the molecular weight distribution in linear polymer melts". In: *Journal of Rheology* 40.2, pp. 303–315.

Milshtein, J. D., R. M. Darling, J. Drake, M. L. Perry, and F. R. Brushett (2017). "The Critical Role of Supporting Electrolyte Selection on Flow Battery Cost". In: *Journal of The Electrochemical Society* 164.14, A3883–A3895.

Missaire, F., C. G. Qiu, and M. A. Rao (1990). "Yield stress of structured and unstructured food suspensions". In: *Journal of Texture Studies* 21.4, pp. 479–490.

Mohamad, A. A. (2020). "Failure analysis of zinc electrode using hydroponic gel and liquid electrolytes in zinc-air batteries at elevated temperatures". In: *Ionics* 26.6, pp. 2981–2988.

Moller, P., A. Fall, V. Chikkadi, D. Derks, and D. Bonn (2009). "An attempt to categorize yield stress fluid behaviour". In: *Philosophical Transactions of the Royal Society A: Mathematical, Physical and Engineering Sciences* 367.1909, pp. 5139–5155.

Møller, P. C., J. Mewis, and D. Bonn (2006). "Yield stress and thixotropy: On the difficulty of measuring yield stresses in practice". In: *Soft Matter* 2.4, pp. 274–283.

Mongruel, A. and M. Cloitre (1999). "Shear viscosity of suspensions of aligned non-Brownian fibres". In: *Rheologica Acta* 38.5, pp. 451–457.

Mooney, M. (1931). "Explicit Formulas for Slip and Fluidity". In: *Journal of Rheology* 2.2, pp. 210–222.

Mussel, M., P. J. Basser, and F. Horkay (2019). "Effects of mono- and divalent cations on the structure and thermodynamic properties of polyelectrolyte gels". In: *Soft Matter* 15.20, pp. 4153–4161.

Nelson, A. Z. and R. H. Ewoldt (2017). "Design of yield-stress fluids: A rheology-to-structure inverse problem". In: *Soft Matter* 13.41, pp. 7578–7594.

N'gouamba, E., J Goyon, L Tocquer, T Oerther, and P Coussot (2020). "Yielding, thixotropy, and strain stiffening of aqueous carbon black suspensions". In: *Journal of Rheology* 64.4, pp. 955–968.

Nikolova, V, P Iliev, K Petrov, T Vitanov, E Zhecheva, R Stoyanova, I Valov, and D Stoychev (2008). "Electrocatalysts for bifunctional oxygen/air electrodes". In: *Journal of Power Sources* 185.2, pp. 727–733.

Nzihou, A., B. Bournonville, P. Marchal, and L. Choplin (2004). "Rheology and heat transfer during mineral residue phosphatation in a rheo-reactor". In: *Chemical Engineering Research and Design* 82.5, pp. 637–641.

Olabi, A. G., T. Wilberforce, M. Ramadan, M. A. Abdelkareem, and A. H. Alami (2020). *Compressed air energy storage systems: Components and operating parameters – A review.*

Oppong, F. K. and J. R. de Bruyn (2011). "Mircorheology and jamming in a yield-stress fluid". In: *Rheologica Acta* 50.4, pp. 317–326.

Ovarlez, G., Q. Barral, and P. Coussot (2010). "Three-dimensional jamming and flows of soft glassy materials". In: *Nature Materials* 9.2, pp. 115–119.

Ovarlez, G, S Cohen-Addad, K Krishan, J Goyon, and P Coussot (2013). "On the existence of a simple yield stress fluid behavior". In: *Journal of Non-Newtonian Fluid Mechanics* 193, pp. 68–79. arXiv: 1209.4325.

Ovarlez, G., S. Rodts, X. Chateau, and P. Coussot (2009). "Phenomenology and physical origin of shear localization and shear banding in complex fluids". In: *Rheologica Acta* 48.8, pp. 831–844.

Ovarlez, G., F. Bertrand, and S. Rodts (2006). "Local determination of the constitutive law of a dense suspension of noncolloidal particles through magnetic resonance imaging". In: *Journal of Rheology* 50.3, pp. 259–292.

Ovarlez, G., F. Mahaut, F. Bertrand, and X. Chateau (2011). "Flows and heterogeneities with a vane tool: Magnetic resonance imaging measurements". In: *Journal of Rheology* 55.2, pp. 197–223. arXiv: 1007.5446.

Ovarlez, G., F. Mahaut, S. Deboeuf, N. Lenoir, S. Hormozi, and X. Chateau (2015). "Flows of suspensions of particles in yield stress fluids". In: *Journal of Rheology* 59.6, pp. 1449–1486.

Owens, C. E., A. J. Hart, and G. H. McKinley (2020). "Improved rheometry of yield stress fluids using bespoke fractal 3D printed vanes". In: *Journal of Rheology* 64.3, pp. 643–662.

Parant, H., G. Muller, T. Le Mercier, J. M. Tarascon, P. Poulin, and A. Colin (2017). "Flowing suspensions of carbon black with high electronic conductivity for flow applications: Comparison between carbons black and exhibition of specific aggregation of carbon particles". In: *Carbon* 119, pp. 10–20.

Park, M., J. Ryu, W. Wang, and J. Cho (2016). "Material design and engineering of next-generation flow-battery technologies". In: *Nature Reviews Materials* 2.1, pp. 1–18.

Pei, P., Z. Ma, K. Wang, X. Wang, M. Song, and H. Xu (2014). "High performance zinc air fuel cell stack". In: *Journal of Power Sources* 249, pp. 13–20.

Petekidis, G, D Vlassopoulos, and P. N. Pusey (2004). "Yielding and flow of sheared colloidal glasses". In: *Journal of Physics Condensed Matter*. Vol. 16. 38, pp. 3955–3963.

Pfeifroth, U., A. Sanchez-Lorenzo, V. Manara, J. Trentmann, and R. Hollmann (2018). "Trends and Variability of Surface Solar Radiation in Europe Based On Surface- and Satellite-Based Data Records". In: *Journal of Geophysical Research: Atmospheres* 123.3, pp. 1735–1754.

Piau, J. M. (2007). "Carbopol gels: Elastoviscoplastic and slippery glasses made of individual swollen sponges. Meso- and macroscopic properties, constitutive equations and scaling laws". In: *Journal of Non-Newtonian Fluid Mechanics* 144.1, pp. 1–29.

Piau, J.-M., M Dorget, J.-F. Palierne, and A Pouchelon (1999). "Shear elasticity and yield stress of silica–silicone physical gels: Fractal approach". In: *Journal of Rheology* 43.2, pp. 305–314.

Pieczyska, E, S Gadaj, W. K. Nowacki, K Hoshio, Y Makino, and H Tobushi (2005). "Characteristics of energy storage and dissipation in TiNi shape memory alloy". In: *Science and Technology of Advanced Materials*. Vol. 6. 8, pp. 889–894.

Pignon, F., A. Magnin, and J.-M. Piau (1996). "Thixotropic colloidal suspensions and flow curves with minimum: Identification of flow regimes and rheometric consequences". In: *Journal of Rheology* 40.4, pp. 573–587.

Pignon, F., A. Magnin, J. M. Piau, B. Cabane, P. Lindner, and O. Diat (1997). "Yield stress thixotropic clay suspension: Investigations of structure by light, neutron, and x-ray scattering". In: *Physical Review E - Statistical Physics, Plasmas, Fluids, and Related Interdisciplinary Topics* 56.3, pp. 3281–3289.

Pinnangudi, B., M. Kuykendal, and S. Bhadra (2017). *Smart Grid Energy Storage*. Elsevier Ltd, pp. 93–135.

Poslinski, A. J., M. E. Ryan, R. K. Gupta, S. G. Seshadri, and F. J. Frechette (1988). "Rheological Behavior of Filled Polymeric Systems I. Yield Stress and Shear-Thinning Effects". In: *Journal of Rheology* 32.7, pp. 703–735.

Pringels, E, C Vervaet, R Verbeeck, P Foreman, and J. P. Remon (2008). "The addition of calcium ions to starch/Carbopol® mixtures enhances the nasal bioavailability of insulin". In: *European Journal of Pharmaceutics and Biopharmaceutics* 68.2, pp. 201–206.

Puapattanakul, A., S. Therdthianwong, A. Therdthianwong, and N. Wongyao (2013). "Improvement of zinc-air fuel cell performance by gelled koh". In: *Energy Procedia* 34, pp. 173–180.

Puig, J., C. Hanotin, M. Neyret, and P. Marchal (2016). "High temperature rheological study of borosilicate glasses containing platinum group metal particles by means of a mixer-type rheometer". In: *Journal of Nuclear Materials* 469, pp. 112–119.

Qian, Y. and G. De Schutter (2018). "Enhancing thixotropy of fresh cement pastes with nanoclay in presence of polycarboxylate ether superplasticizer (PCE)". In: *Cement and Concrete Research* 111.May, pp. 15–22.

R. Mainar, A., O. Leonet, M. Bengoechea, I. Boyano, I. De Meatza, A. Kvasha, A. Guerfi, and J. Alberto Blázquez (2016). *Alkaline aqueous electrolytes for secondary zinc-air batteries: An overview*.

Raffel, M, C. Willert, S. Wereley, and J. Kompenhans (1998). *Particle Image Velocimetry - A Practical Guide*. Springer-Verlag Berlin Heidelberg, p. 229.

Rahman, M. A., X. Wang, and C. Wen (2013). "High Energy Density Metal-Air Batteries: A Review". In: *Journal of The Electrochemical Society* 160.10, A1759–A1771.

Reichle, R. A., K. G. McCurdy, and L. G. Hepler (1975). "Zinc Hydroxide: Solubility Product and Hydroxy-complex Stability Constants from 12.5–75 °C". In: *Canadian Journal of Chemistry* 53.24, pp. 3841–3845.

Rochefort, W. E. and S. Middleman (1987). "Rheology of Xanthan Gum: Salt, Temperature, and Strain Effects in Oscillatory and Steady Shear Experiments". In: *Journal of Rheology* 31.4, pp. 337–369.

Rodriguez, B. E., E. W. Kaler, and M. S. Wolfe (1992). "Binary Mixtures of Monodisperse Latex Dispersions. 2. Viscosity". In: *Langmuir* 8.10, pp. 2382–2389.

Rouyer, F., S. Cohen-Addad, and R. Höhler (2005). "Is the yield stress of aqueous foam a well-defined quantity?" In: *Colloids and Surfaces A: Physicochemical and Engineering Aspects*. Vol. 263. 1-3, pp. 111–116.

Rugolo, J. and M. J. Aziz (2012). "Electricity storage for intermittent renewable sources". In: *Energy and Environmental Science* 5.5, pp. 7151–7160.

Sánchez-Díez, E., E. Ventosa, M. Guarnieri, A. Trovò, C. Flox, R. Marcilla, F. Soavi, P. Mazur, E. Aranzabe, and R. Ferret (2021). "Redox flow batteries: Status and perspective towards sustainable stationary energy storage". In: *Journal of Power Sources* 481, p. 228804.

Sasikala, N, K Ramya, and K. S. Dhathathreyan (2014). "Bifunctional electrocatalyst for oxygen/air electrodes". In: *Energy Conversion and Management* 77, pp. 545–549.

Schmid, M, U Schadeck, and M Willert-Porada (2017a). "Development of silica based coatings on zinc particles for improved oxidation behavior in battery applications". In: *Surface and Coatings Technology* 310, pp. 51–58.

Schmid, M and M Willert-Porada (2017b). "Electrochemical behavior of zinc particles with silica based coatings as anode material for zinc air batteries with improved discharge capacity". In: *Journal of Power Sources* 351, pp. 115–122.

Sdougos, H. P., S. R. Bussolari, and C. F. Dewey (1984). "Secondary flow and turbulence in a cone-and-plate device". In: *Journal of Fluid Mechanics* 138, pp. 379–404.

Shen, L., Y. Lin, Q. Du, W. Zhong, and Y. Yang (2005). "Preparation and rheology of polyamide-6/attapulgite nanocomposites and studies on their percolated structure". In: *Polymer* 46.15, pp. 5758–5766.

Shigematsu, T. (2019). *The development and demonstration status of practical flow battery systems.*

Singla, A. K., M. Chawla, and A. Singh (2000). *Potential applications of carbomer in oral mucoadhesive controlled drug delivery system: A review.*

Sisternes, F. J. de, J. D. Jenkins, and A. Botterud (2016). "The value of energy storage in decarbonizing the electricity sector". In: *Applied Energy* 175, pp. 368–379.

Skyllas-Kazacos, M. and F. Grossmith (1987). "Efficient Vanadium Redox Flow Cell". In: *Journal of The Electrochemical Society* 134.12, pp. 2950–2953.

Skyllas-Kazacos, M., M. Rychcik, R. G. Robins, A. G. Fane, and M. A. Green (1986). "New All-Vanadium Redox Flow Cell". In: *Journal of The Electrochemical Society* 133.5, pp. 1057–1058.

Smedley, S. and X. G. Zhang (2009). "Secondary Batteries - Metal-Air Systems — Zinc-Air: Hydraulic Recharge". In: *Encyclopedia of Electrochemical Power Sources*, pp. 393–403.

Smith, K. C., Y.-M. Chiang, and W. Craig Carter (2014). "Maximizing Energetic Efficiency in Flow Batteries Utilizing Non-Newtonian Fluids". In: *Journal of The Electrochemical Society* 161.4, A486–A496.

Sollich, P., F. Lequeux, P. Hébraud, and M. E. Cates (1997). "Rheology of soft glassy materials". In: *Physical Review Letters* 78.10, pp. 2020–2023. arXiv: `9611228 [cond-mat]`.

Solomon, B. R., X. Chen, L. Rapoport, A. Helal, G. H. McKinley, Y. M. Chiang, and K. K. Varanasi (2018). "Enhancing the Performance of Viscous Electrode-Based Flow Batteries Using Lubricant-Impregnated Surfaces". In: *ACS Applied Energy Materials* 1.8, pp. 3614–3621.

Soloveichik, G. L. (2011). *Battery technologies for large-scale stationary energy storage.*

Sonneveld, P. J. A. N. (1991). "The zinc suspension electrode". PhD thesis. Technische Universiteit Eindhoven.

Stamm, J., A. Varzi, A. Latz, and B. Horstmann (2017). "Modeling nucleation and growth of zinc oxide during discharge of primary zinc-air batteries". In: *Journal of Power Sources* 360, pp. 136–149. arXiv: 1612.03464.

Stickel, J. J. and R. L. Powell (2005). *Fluid mechanics and rheology of dense suspensions.*

Tang, A., J. Bao, and M. Skyllas-Kazacos (2014). "Studies on pressure losses and flow rate optimization in vanadium redox flow battery". In: *Journal of Power Sources* 248, pp. 154–162.

Thomas, S, N Birbilis, M. S. Venkatraman, and I. S. Cole (2013). *Self-repairing oxides to protect zinc: Review, discussion and prospects.*

Tilman, D. and C. Lehman (2001). "Human-caused environmental change: Impacts on plant diversity and evolution". In: *Proceedings of the National Academy of Sciences of the United States of America* 98.10, pp. 5433–5440.

Torquato, S, T. M. Truskett, and P. G. Debenedetti (2000). "Is random close packing of spheres well defined?" In: *Physical Review Letters* 84.10, pp. 2064–2067. arXiv: 0003416 [cond-mat].

Tran, T. N. T., H. J. Chung, and D. G. Ivey (2019). "A study of alkaline gel polymer electrolytes for rechargeable zinc–air batteries". In: *Electrochimica Acta* 327, p. 135021.

Tran, T. N. T., M. P. Clark, H. Chung, and D. G. Ivey (2020). "Effects of Crosslinker Concentration in Poly(Acrylic Acid)-KOH Gel Electrolyte on Performance of Zinc-Air Batteries". In: *Batteries & Supercaps* 3.5, pp. 409–416.

Varges, P. R., C. M. Costa, B. S. Fonseca, M. F. Naccache, and P. R. De Souza Mendes (2019). "Rheological characterization of carbopol ® dispersions in water and in water/glycerol solutions". In: *Fluids* 4.1.

Vikström, H., S. Davidsson, and M. Höök (2013). "Lithium availability and future production outlooks". In: *Applied Energy* 110, pp. 252–266.

Visco, S. J., V. Y. Nimon, A. Petrov, K. Pridatko, N. Goncharenko, E. Nimon, L. De Jonghe, Y. M. Volfkovich, and D. A. Bograchev (2014). "Aqueous and nonaqueous lithium-air batteries enabled by water-stable lithium metal electrodes". In: *Journal of Solid State Electrochemistry* 18.5, pp. 1443–1456.

Wagner, N. J. and J. F. Brady (2009). "Shear thickening in colloidal dispersions". In: *Physics Today* 62.10, pp. 27–32.

Wang, K., P. Pei, Z. Ma, H. Chen, H. Xu, D. Chen, and X. Wang (2015). "Dendrite growth in the recharging process of zinc-air batteries". In: *Journal of Materials Chemistry A* 3.45, pp. 22648–22655.

Weber, A. Z., M. M. Mench, J. P. Meyers, P. N. Ross, J. T. Gostick, and Q. Liu (2011). *Redox flow batteries: A review.*

Wei, T. S., F. Y. Fan, A. Helal, K. C. Smith, G. H. McKinley, Y. M. Chiang, and J. A. Lewis (2015). "Biphasic Electrode Suspensions for Li-Ion Semi-solid Flow Cells with High Energy

Density, Fast Charge Transport, and Low-Dissipation Flow". In: *Advanced Energy Materials* 5.15, p. 1500535.

Wei, X., W. Pan, W. Duan, A. Hollas, Z. Yang, B. Li, Z. Nie, J. Liu, D. Reed, W. Wang, and V. Sprenkle (2017). "Materials and Systems for Organic Redox Flow Batteries: Status and Challenges". In: *ACS Energy Letters* 2.9, pp. 2187–2204.

Weissenberg, K. (1947). "A continuum theory of rheological phenomena". In: *Nature* 159.4035, pp. 310–311.

Wilson, D. I. (2018). "What is rheology?" In: *Eye* 32.2, pp. 179–183.

Wright, P. R., F. J. Muzzio, and B. J. Glasser (1998). "Batch uptake of lysozyme: Effect of solution viscosity and mass transfer on adsorption". In: *Biotechnology Progress* 14.6, pp. 913–921.

Xia, Y and P. T. Callaghan (1991). "Study of Shear Thinning in High Polymer Solution Using Dynamic NMR Microscopy". In: *Macromolecules* 24.17, pp. 4777–4786.

Xiong, B., P. Purswani, T. Pawlik, L. Samineni, Z. T. Karpyn, A. L. Zydney, and M. Kumar (2020). "Mechanical degradation of polyacrylamide at ultra high deformation rates during hydraulic fracturing". In: *Environmental Science: Water Research and Technology* 6.1, pp. 166–172.

Yang, C., Z. Zhang, Z. Tian, K. Zhang, J. Li, and Y. Lai (2016). "Effects of Carboxymethyl Cellulose on the Electrochemical Characteristics and Dendrite Growth of Zinc in Alkaline Solution". In: *Journal of The Electrochemical Society* 163.9, A1836–A1840.

Yang, H., Y. Cao, X. Ai, and L. Xiao (2004). "Improved discharge capacity and suppressed surface passivation of zinc anode in dilute alkaline solution using surfactant additives". In: *Journal of Power Sources* 128.1, pp. 97–101.

Yao, N. Y., R. J. Larsen, and D. A. Weitz (2008). "Probing nonlinear rheology with inertio-elastic oscillations". In: *Journal of Rheology* 52.4, pp. 1013–1025.

Ye, J., L. Xia, C. Wu, M. Ding, C. Jia, and Q. Wang (2019). *Redox targeting-based flow batteries.*

Yoo, B., M. A. Rao, and J. F. Steffe (1995). "Yield stress of food dispersions with the vane method at controlled shear rate and shear stress". In: *Journal of Texture Studies* 26.1, pp. 1–10.

Yoshimura, A. and R. K. Prud'homme (1988). "Wall Slip Corrections for Couette and Parallel Disk Viscometers". In: *Journal of Rheology* 32.1, pp. 53–67.

Yuan, W. L., X. Yang, L. He, Y. Xue, S. Qin, and G. H. Tao (2018). "Viscosity, conductivity, and electrochemical property of dicyanamide ionic liquids". In: *Frontiers in Chemistry* 6.59.

Zarraga, I. E., D. A. Hill, and D. T. Leighton (2000). "The characterization of the total stress of concentrated suspensions of noncolloidal spheres in Newtonian fluids". In: *Journal of Rheology* 44.2, pp. 185–220.

Zhang, T., N. Imanishi, Y. Shimonishi, A. Hirano, J. Xie, Y. Takeda, O. Yamamoto, and N. Sammes (2010). "Stability of a Water-Stable Lithium Metal Anode for a Lithium–Air

Battery with Acetic Acid–Water Solutions". In: *Journal of The Electrochemical Society* 157.2, A214.

Zhang, X. G. (2009). "SECONDARY BATTERIES – ZINC SYSTEMS Zinc Electrodes : Overview". In: *Encyclopedia of Electrochemical Power Sources*, pp. 454–468.

Zhang, X. G. (1996). *Corrosion and Electrochemistry of Zinc*.

Zhang, Z., C. Zuo, Z. Liu, Y. Yu, Y. Zuo, and Y. Song (2014). "All-solid-state Al-air batteries with polymer alkaline gel electrolyte". In: *Journal of Power Sources* 251, pp. 470–475.

Université
Grenoble Alpes